Fracture Mechanisms of Layer-By-Layer Polyurethane/Poly(Acrylic Acid) Nanocomposite

by

Eugene R Kheng

A dissertation submitted in partial fulfillment
of the requirements for the degree of
Doctor of Philosophy
(Mechanical Engineering)
in The University of Michigan
2014

Doctoral Committee:

Professor Anthony M. Waas, Chairperson
Professor Ellen M. Arruda
Professor Nicholas A. Kotov
Professor Michael Thouless

For Victoria & Leonora

ACKNOWLEDGEMENTS

I would like to express my gratitude to my advisor, Professor Anthony Waas, for his guidance and support throughout my time at the University of Michigan. I would also like to thank Professors Ellen Arruda, Nicholas Kotov and Michael Thouless for serving on the doctoral committee and for all their assistance in research over the years.

I am thankful for the many colleagues who have given me assistance and enriched my time here, Paul Davidson, Trisha Sain, Pavana Prabhakar, Cao Keqin, Paul Podsiadlo, Amit Salvi, Christian Heinrich, Zhang Dianyun, Pascal Meyer, Wooseok Ji, Evan Pineda, Royan D'Mello, Brian Justusson, Ming Yang, Bongjun Yeom, Tanaz Rahimzadeh, Cyrus Kosztowny, Lucas Hansen, Scott Stapleton and Siva Shankar Rudraraju.

I would also like to thank the staff at the aerospace department, Terry Larrow for his assistance in machining experimental parts, Aaron Borgman for moving electrons to the right places, Thomas Griffin, Crhis Chartier and Dave Mclean.

I would like to thank my wife, Victoria, for being there for me always. I would also like to thank my daughter, Leora, for reminding me of the importance of family and for not getting into more trouble than she does. I would like to thank my parents, as well as my extended family, for their support through these years.

The author would also like to acknowledge the support of the Office of Naval Research.

TABLE OF CONTENTS

LIST OF FIGURES

Figure

LIST OF TABLES

Table

LIST OF APPENDICES

Appendix

LIST OF ABBREVIATIONS

LBL Layer-by-Layer

MTM Montmorillonite

PU Polyurethane

PAA Poly(Acrylic Acid)

PU/PAA Polyurethane/Poly(Acrylic Acid)

LDM Large Dipping Machine

HVLP High Volume Low Pressure

SEM Scanning Electron Microscope

LSDM Large Spray Deposition Machine

SENT Single Edge-Notch Tension

DCZM Discrete Cohesive Zone Model

LVDT Linear Variable Differential Transformer

LVSEM Low Vacuum Scanning Electron Microscope

EMAL Electron Microscopy and Analysis Laboratory

FE Finite Element

ABSTRACT

Fracture Mechanisms of Layer-By-Layer Polyurethane/Poly(Acrylic Acid) Nanocomposite

by

Eugene R Kheng

Chair: Anthony M Waas

A Layer-by-Layer (LBL) material is examined in detail in this thesis. Improvements are made to its method of manufacture. Efforts are made to understand its fracture mechanisms and take advantage of these fracture mechanisms in the absorption of impact energy.

A novel series of experiments has been performed on LBL manufactured thin films to demonstrate their unique fracture mechanisms. Polyurethane/Poly(Acrylic Acid) (PU/PAA) and $PU/PAA/(PU/Clay)_5$ nanocomposite films readily undergo Interlaminar mode II fracture, because of the relatively weak elctrostatic bonds between monolayers. Tensile tests performed while under observation by a scanning electron microscope demonstrate the tendency of these nanocomposite films to undergo interlaminar mode II fracture even when loads are applied in the plane of nanocomposite film.

Furthermore, a novel automated manufacturing facility has been designed and built to deposit large sheets of Layer-by-Layer nanocomposite film. These large sheets are incorporated into a borosillicate glass composite in order to compare the

ballistic characteristics of LBL PU based nanocomposite films to a single cast layer of polyurethane. It is demonstrated that shear fracture is the mode of failure in the blocks containing the nanocomposite film. The Shear Fracture surface in the nanocomposite after it has undergone a ballistic impact is characterized.

Additional experiments are performed to characterize the interlaminar fracture stresses and toughnesses, to assist in the implementation of a numerical crack band model that describes the nanocomposite film. The computational model predicts the failure of the ballistic nanocomposite samples.

CHAPTER I

Introduction

LBL deposition of nanocomposites has received much attention in recent times. Nanocomposites deposited in a LBL machine have a planar layered nanostructure which imparts useful interactions and mechanisms between any two sequential layers. Like traditional fiber matrix composites, this anisotropy can be take advantage of, by designing the nanocomposite to act in a manner advantageous to the application.

LBL Nanocomposites are manufactured by depositing a minimal amount of two oppositely charged materials on a glass substrate. The opposite charges ensure that each layer has a characteristic bond strength to the preceeding and subsequent layer. Rinsing the substrate well between each deposition ensures that only molecules/particles that have strong electrostatic attachment to the previous layer remain attached. This method of deposition results in a very slow build up of material in the thickness direction and requires multiple depositions in order to build up a micron order thickness of material. A schematic of a nanocomposite is shown in figure 1.1. It is to be noted that each monolayer of material ideally consists of a single molecule thickness of polymer or single thickness of particles, resulting in a very thin material even after hundreds of deposited layers. However, depending on the quality of rinsing, it is observed that more than one molecule can be deposited in each layer. An alternate set of positive and negatively charged layers is known as a bilayer.

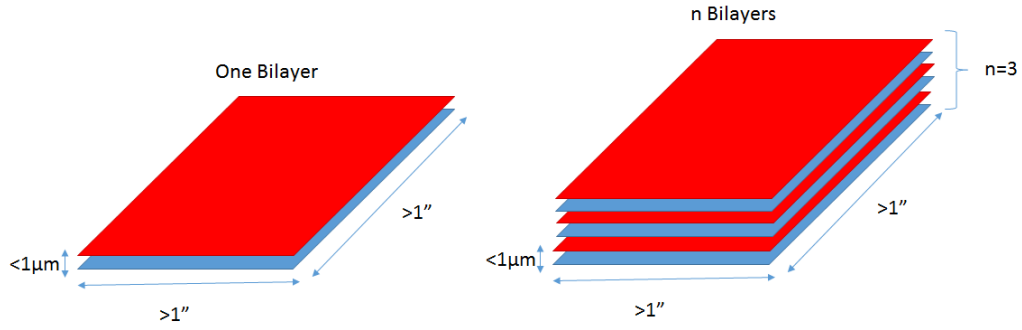

Figure 1.1: Bilayer Schematic

LBL Nanocomposites can be used to add various functionality to the base materials. Depending on the base material and additive material or materials, electrical conductivity, increased elastic modulus and fracture toughness can be tailored to the intended use of the nanocomposite.

Tests performed on free standing film as well as films incorporated into a larger composite block have demonstrated that LBL films have a tendency to exhibit interlaminar mode II fracture. Mode II interlaminar fracture can be taken advantage of in ballistic protection. Since the nanocomposite is transparent, it is a suitable candidate for transparent armour for use in viewing ports in vehicles and structures.

1.1 Transparent Armor

The armor used in armored vehicles such as tanks and warships were, in their initial iterations, a thick monolithic layer of steel. As the projectiles they were designed to defeat became larger and more powerful, the layer of steel was thickened, adding tremendous amounts of weight to the vehicle. Modern armored vehicles rely on laminated armor systems *Chan* (1997) designed to protect the interior while reducing the weight of the vehicle.

There is a similar trend in the transparent armor used in windows and viewing ports of armored vehicles in moving to laminated materials, sandwiching a layer of

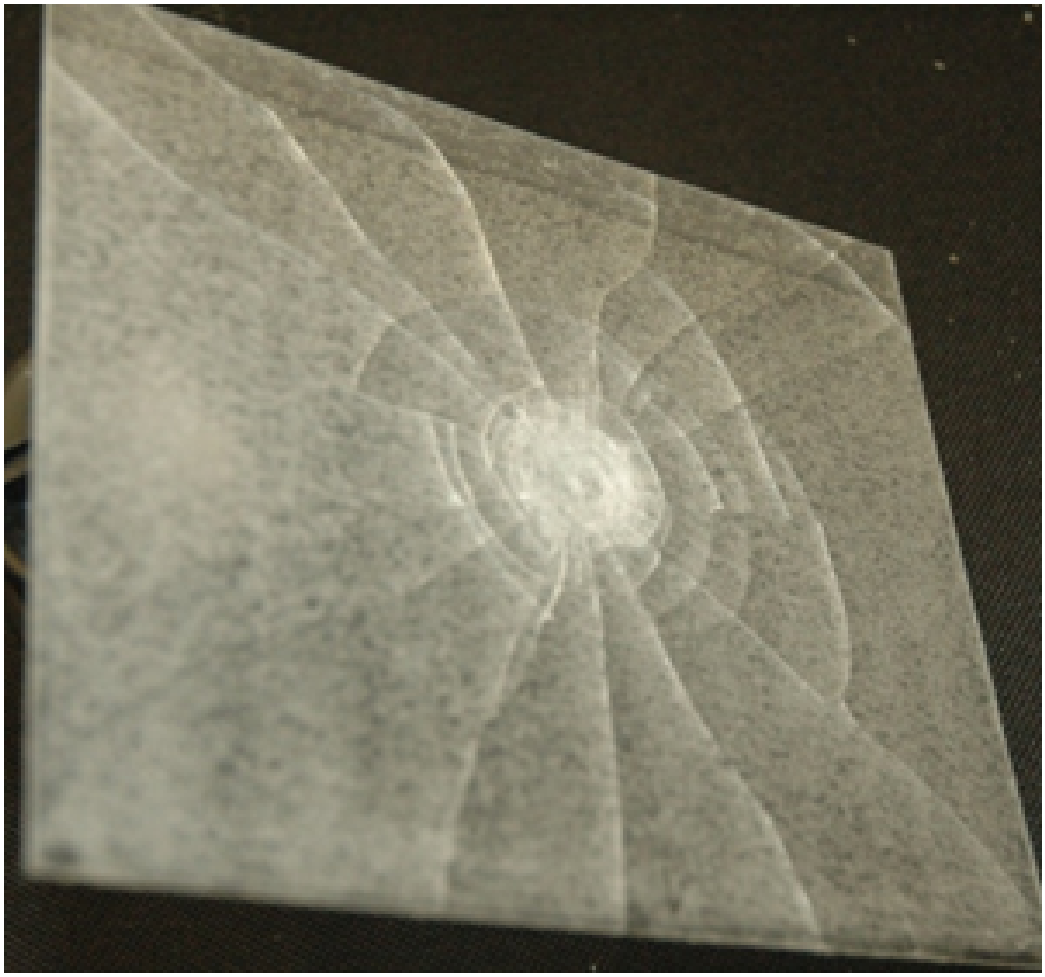

Figure 1.2: Spider web cracks in glass

polycarbonate *Gunnarsson et al.* (2009) within two layers of glass. There is an additional requirement that the materials used in this application be optically transparent, to allow the passage of light to occupants or sensors on the interior.

Primarily used in defeating small arms fire, transparent armor found on armored cars aims to dissipate the kinetic energy of an incoming bullet through the deformation of the tough polycarbonate layer and the fracture into a spider's web of the first glass layer to meet the bullet, as seen in figure 1.2. The primary function of the glass is to protect the polycarbonate from scratches and subsequent clouding.

Because the types of materials to be used in transparent armor systems are so limited, many of the mechanisms that provide advantages to non-transparent laminated

armor systems in defeating an incoming projectile cannot be exploited in transparent laminated armor. For example, hard ceramics are often used in laminated tank armor, designed to abrade the incoming projectile.

Nanocomposites could be a strong addition to modern laminated transparent armors. Some nanocomposites are transparent, even if their constituent materials are not. For example: Montmorillonite (MTM) is normally an opaque and yellow powder, but LBL nanocomposite films made incorporating MTM are transparent to the visible spectrum of light. Using a LBL nanocompositing process, it might be possible to incorporate materials into laminated transparent armor that, if incorporated by traditional means, would result in an opaque composite. This would allow transparent armor manufacturers to add greater functionality to their transparent armor.

1.2 Main Contributions and Organization of Thesis

In this thesis, the suitability of LBL nanocomposites for incorporation into laminated transparent armor is explored. Initial tests on free standing LBL nanocomposite film demonstrate that these films possess a unique fracture mechanism, that makes them susceptible to developing shear fracture between monolayers, independent of how they are loaded. Incorporating this mechanism into transparent armor would effectively spread the energy of an incoming projectile away from the impact point. A novel method of deposition is developed in order to produce the material in a large enough format for impact testing, and indicates how this material could be produced on a large scale. Tests indicate that there are advantages of the LBL nanocomposite over similar thicknesses of monolithic polymer and that the fracture mechanisms that were present in the free standing film are also present in the film when incorporated into a composite block.

The dissertation is organized as follows; Chapter II provides a detailed description of the development of a novel scale-able spray deposition machine, which is able to

deposit film on a suitable material of any size, if the machine is made large enough. Chapter III describes the initial tests and numerical modeling done on free standing film, in order to characterize the fracture toughness of the film when a crack is grown perpendicular to the normal of the film. Chapter IV demonstrates that the nanocomposite film is susceptible to mode II fracture parallel to the normal despite having no applied load in that direction, in a series of fracture tests done while the material is under observation within a scanning electron microscope. Chapter V describes the impact tests done on composite glass plates incorporating the LBL nanocomposite. Chapter VI describes additional tests which are performed on the nanocomposite in order to further understand the fracture properties. Chapter VII details a numerical study performed on the composite glass plates in chapter V to characterize the performance of the nanocomposite later.

CHAPTER II

THE DESIGN OF A NOVEL AUTOMATED MANUFACTURING PROCESS FOR LAYER BY LAYER DEPOSITION

In this chapter, manufacturing of Polymer Nanocomposites by LBL deposition is discussed. In particular, various large scale deposition devices are described. These devices were instrumental in obtaining large scale samples suitable for impact testing. This manufacturing process can be scaled up such that any sized object, made of a suitable material, could be coated in a LBL film.

2.1 Classical LBL Dipping Machines

Until recently, LBL polymer nanocomposites were deposited by a variety of dipping machines. These machines would dip glass slides in charged polymer or nanoparticle solutions and rinse them in a water bath between dipping steps. The deposition solutions are held beakers and are not replaced between cycles. The rinse water are also held in beakers but is replaced between rinses. A schematic for LBL deposition is included below in figure 2.1.

The method of LBL deposition seeks to obtain controlled and thin(nanometer scale) layers of material. In order to do so, oppositely charged polymer and/or

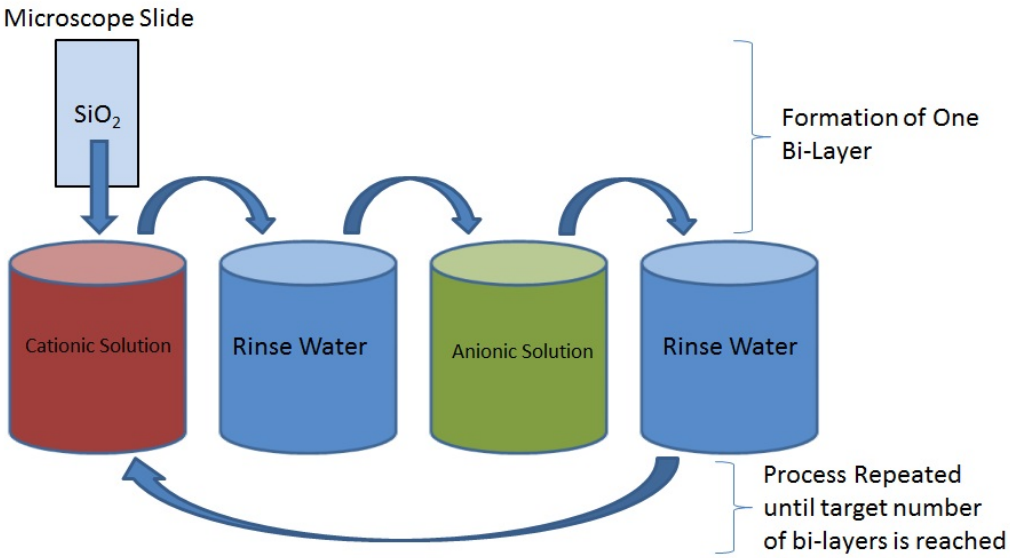

Figure 2.1: Schematic for LBL Deposition

nanoparticle dispersions in water are deposited on a glass slide, rinsing is performed between each deposition step in order to rinse off polymers and/or nanoparticles that are not firmly attached to the preceeding layer. The nanocomposite has to be composed of two oppositely charged materials in order for the layers to grow with each step.

The first family of PU and PAA polymer nanocomposites was manufactured in this way. Glass slides are attached to a dipping machine. To deposit the PU layer, the glass slide is dipped into a diluted solution (3.0 wt%) of Cationic PU for 30 seconds. The Cationic PU is obtained from HEPCE Co. and has an original dilution of 30wt%. The slides are then rinsed in a running water bath for 1 minute before depositing the PAA layer. To deposit the PAA layer, the glass slide is dipped into a 1wt% solution of PAA for 30 seconds. The slides are then rinsed in a running water bath for a minute before depositing the PU layer. A deposition of one PU layer and one PAA layer is called a bilayer. The film is built up by repeating these steps to obtain 100 bilayers.

These LBL dipping machines can deposit on 3 to 6 standard microscope glass slides simultaneously. This gives a yield of 6 to 12 films that are 1inch by 2.5inches per

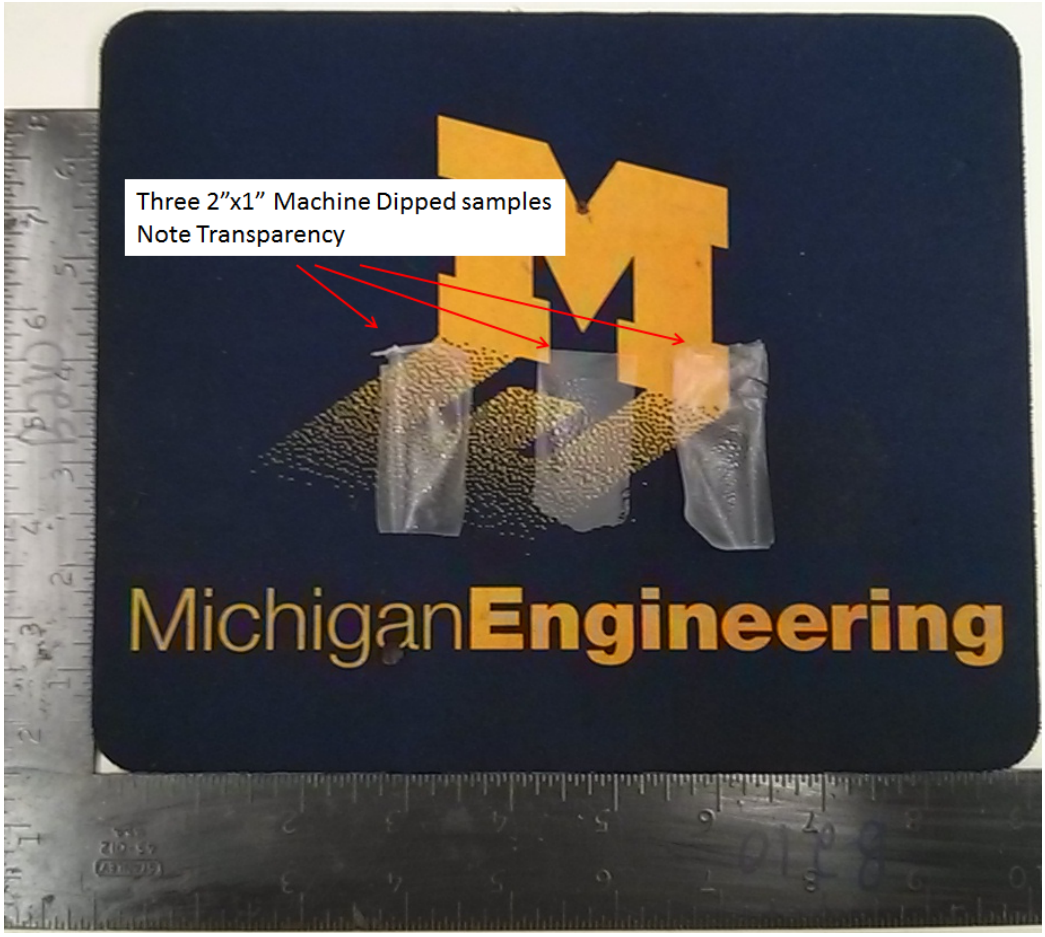

Figure 2.2: Detached LBL Film manufactured by Dipping Machine

deposition cycle, a sample of these films can be seen in figure 2.2. The commercially available nanostrata Deposition machine is shown in figure 2.3. A sample of the thickness can be seen in figure 2.4, of note is inconsistency of the thickness.

2.2 Development of Large LBL Systems

In order to increase the yield of these LBL machines. Initial attempts made to increase the yield of LBL machines were focused on enlarging the dipping process. These Large Dipping Machine (LDM) dipped large (1' x 1' x 1.1mm) pieces of Borofloat Glass obtained from Cincinatti Gasket in correspondingly large (10 gallon) baths of solution and rinsing water. The problem faced by these LDM was getting

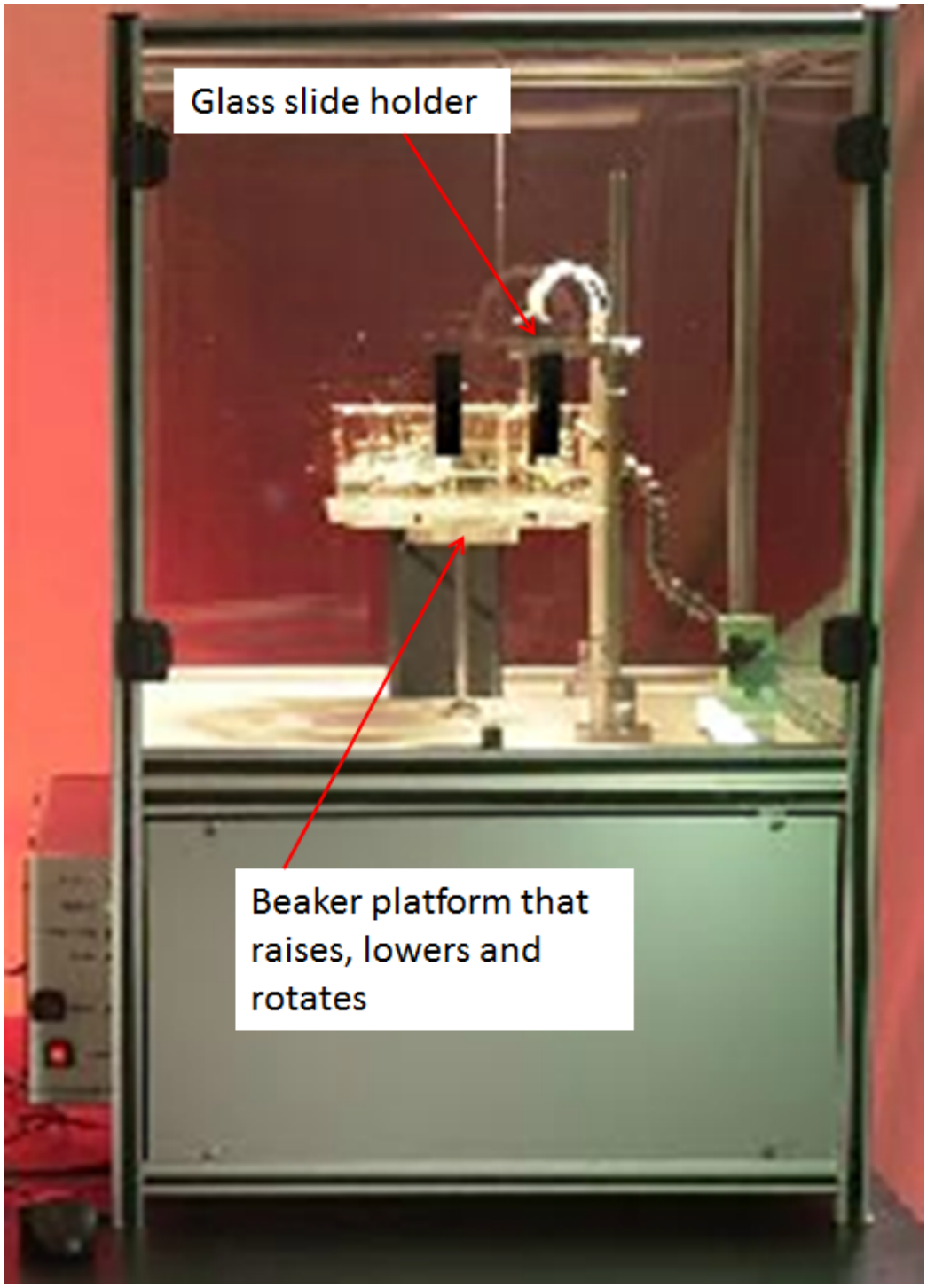

Figure 2.3: Nanostrata Automated Dipping LBL Deposition Machine

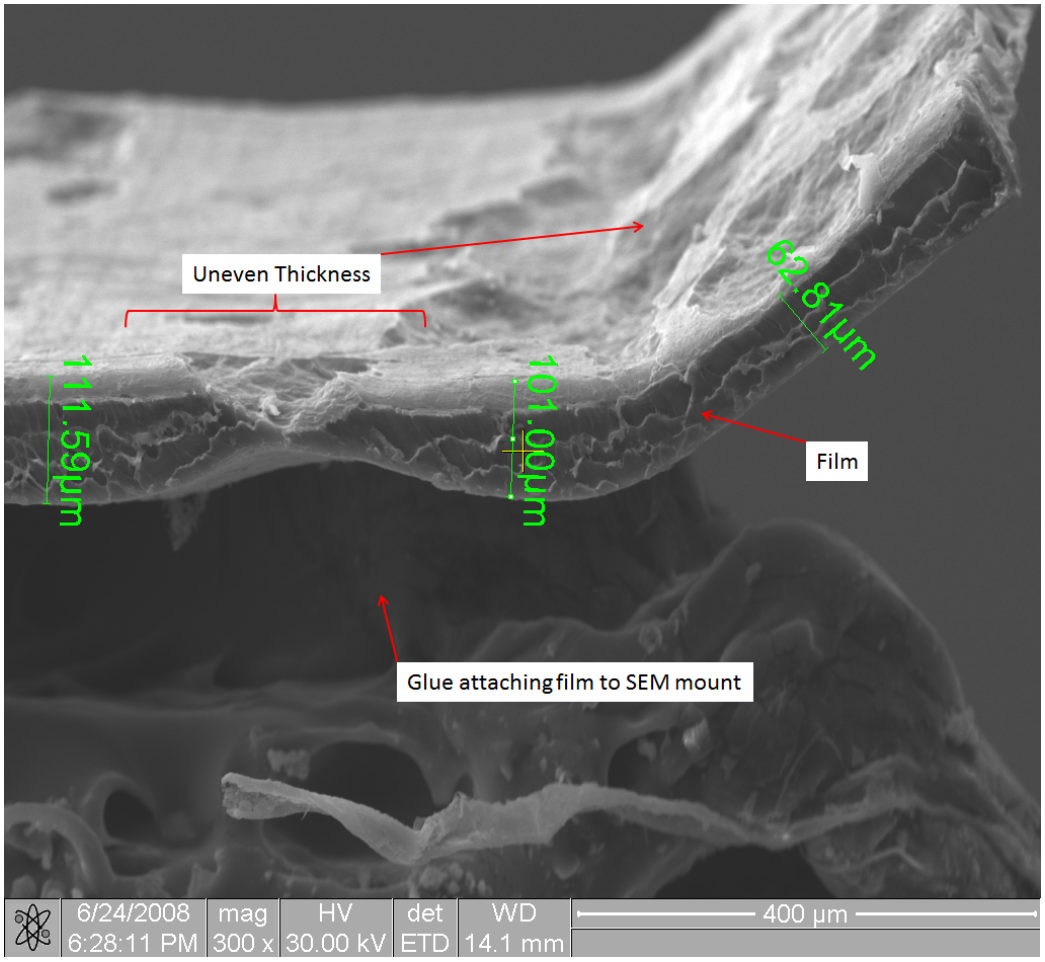

Figure 2.4: Film Thickness of PU/PAA manufactured by dipping machine

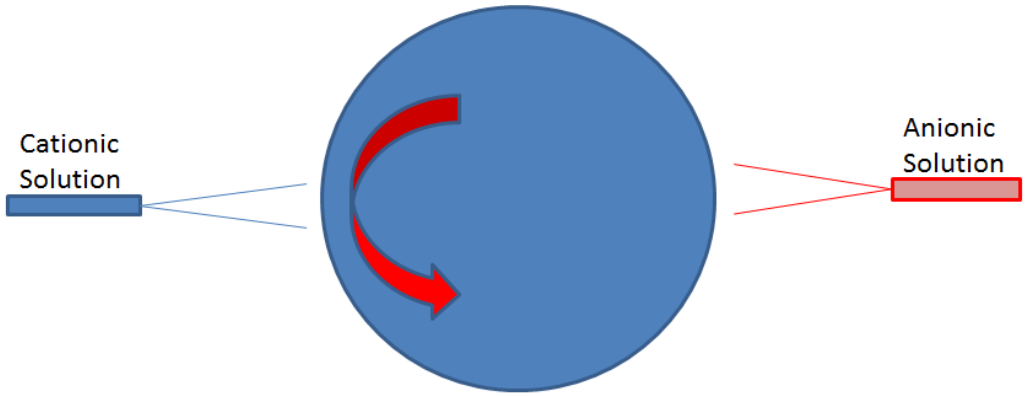

Figure 2.5: Schematic for Rotating Drum LBL Deposition machine

enough clean water in the rinsing bath. Getting enough water flow in order to entirely replace the water in a bath suitable for rinsing multiple layers of 1ft by 1ft glass was uneconomical and going to larger pieces of glass would not be possible. For example, the LDM used a 10 gallon bath would require a refill rate of 20 gallons/minute to make the rinse water clean between rinse cycles.

Subsequent attempts made involved the use of High Volume Low Pressure (HVLP) sprayers, which are used in the application of liquids to large surfaces, the most common usage for these sprayers is the application of paint to cars and other large objects. An early example of these sprayer LBL machines sprayed on the two reactants on opposite sides of a rotating substrate mounted on a drum. Rinsing was performed by flowing water over the substrate between the reactant sprayers. This flowing rinse system was rarely used because it would damage most films. A schematic of the rotating drum setup can be seen in figure 2.5. Films that are not rinsed have a bubbly appearance and are not smooth, as seen in figure 2.6. The film produced by the rotating drum ranges from 0mm to approximately 1mm thickness.

In the work that contributed to this thesis, it was suggested that the rinse water is sprayed onto the substrate with another HVLP nozzle. This would necessitate a move away from drum systems to a linear system in order to accomodate for the space

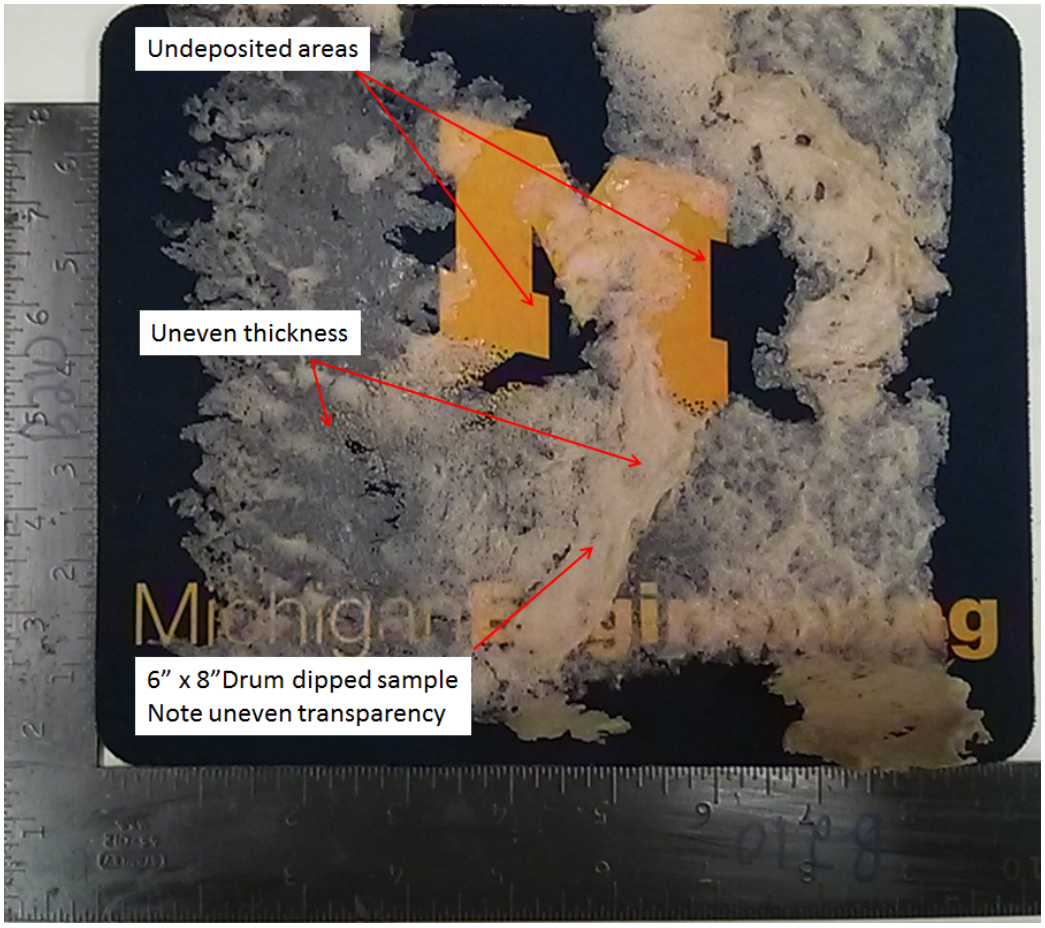

Figure 2.6: Detached LBL Film manufactured by Rotating Drum LBL Machine

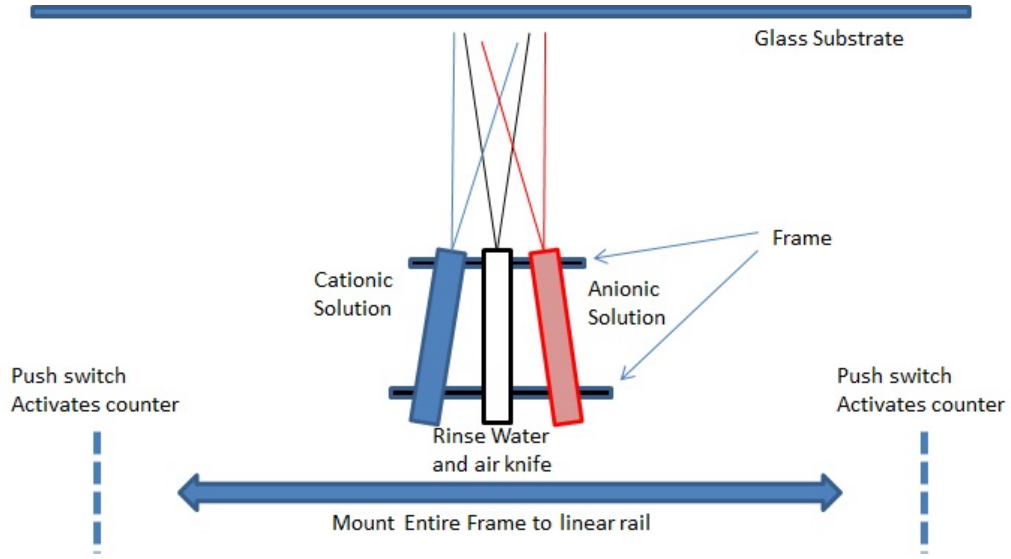

Figure 2.7: Schematic for LBL Spraying Machine

required for the additional volume of rinse water (relative to solution). The linear system allows us to incorporate multiple rinse passes for each solution deposition pass, while maintaining a low flow of rinse water, so as not to damage the film. A schematic of the linear system is included in figure 2.7. In order to test the concept, it was decided to perform the deposition of PU/PAA manually.

This manual test of the concept was performed in a paint booth, because of the toxic nature of PAA. The researcher was dressed in personal protective equipment - chemical resistant lab coat, latex gloves and full face mask respirator. A triple spray gun set, manufactured by Vaper, was used to apply the solutions and rinse water. Due to the large volume required, the largest nozzle (1.7mm) was selected to spray the rinse water, the 1.4mm nozzle was selected to spray the relatively more viscous PU solution and the 1.0mm nozzle was used to spray the PAA solution. It was decided that as little would be changed from the dipping process as possible, with respect to dipping times and solution concentrations. The dilutions of both the PU solution and PAA solution were kept constant from the dipping machines. As far as possible with a manual test, solutions were left on the pane for 30 seconds before rinsing. Rinse time was generally longer than 2 minutes, because of the large surface that required

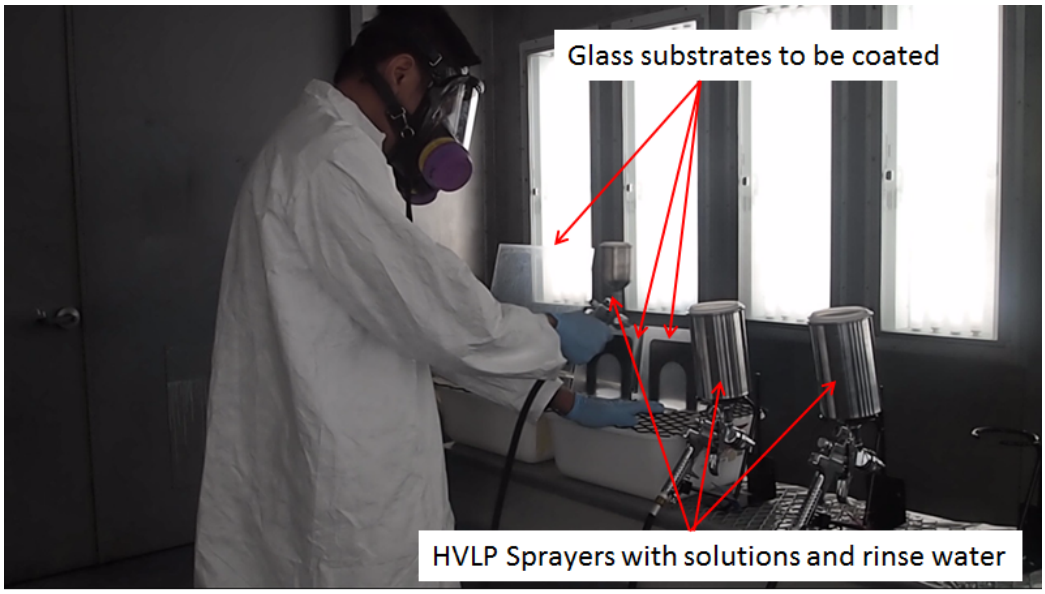

Figure 2.8: Manual Deposition of LBL by Spraying

rinsing, it was necessary to rinse the substrates until the runoff was clear. Two 12 inch by 12 inch and one 6 inch by 6 inch borosillicate glass panes were selected as the deposition substrates, these substrates were held vertically, so that gravity would assist in pulling the rinse water off the surface. The Experimental deposition setup is seen in figure 2.8. The borofloat glass substrate is obtained from Cincinatti Gasket.

This deposition concept was successful in producing PU/PAA of a very uniform nature. Whereas the dipped PU/PAA produced films with a large variance in thickness, the spray concept produced films that were more uniform but thinner. Measured in a Scanning Electron Microscope (SEM), the dipped PU/PAA samples have a thickness of 40 $\pm$ 10 micron and the sprayed PU/PAA samples have a thickness of 21 $\pm$ 1 micron. It is unnecessary to hot press the sprayed PU/PAA in order to produce a flat sample for testing as it was necessary for dipped PU/PAA.

2.3 Development of LSDM

After testing the concept manually in a paint booth, a robot was constructed inside of a fume hood to perform the deposition. The robot consists of three independent systems: a linear motion rail from Velmex, an automatic HVLP system from Anest-Iwata and a custom built electronics suite to activate the spray system. Three HVLP sprayers are mounted to the linear motion rail, arrayed in an arc to spray the same point in space about a foot away from the middle nozzle. One HVLP system sprays PU solution, another HVLP system sprays PAA solution and the last sprays the rinse water. The HVLP system is powered by the building air supply and building tap water is used to rinse the plates.

The linear motion rail is set to repeatedly move from edge to edge. Push-switches are placed on the limit of motion of the rail to set off the counter in the electronics suite. When the counter in the electronics suite is activated, it switches between the proper HVLP sprayers in a pre-determined order. The suite can be reprogrammed as necessary if the sprayer is set to a different travel length or has to deposit a different system. The sprayer was set to mimic the manual spray deposition, spending 3 times as much time rinsing each cycle when compared to depositing. The Automated **LDSM!** is seen in figure 2.9.

The LSDM setup allows us to deposit a single 25 inch by 10 inch surface, as opposed to twelve separate 1 inch by 2.5 inch surfaces in similar time frames. As an added incentive, the film thickness distribution is greatly improved, due to the better rinsing in the LSDM. A detached sample of the film is included in figure 2.10. The thicknesses measured in figure 2.11 indicate that PU/PAA manufactured by spraying is much more consistent than those manufactured by dipping, there are fewer imperfections in thickness caused by uneven rinsing.

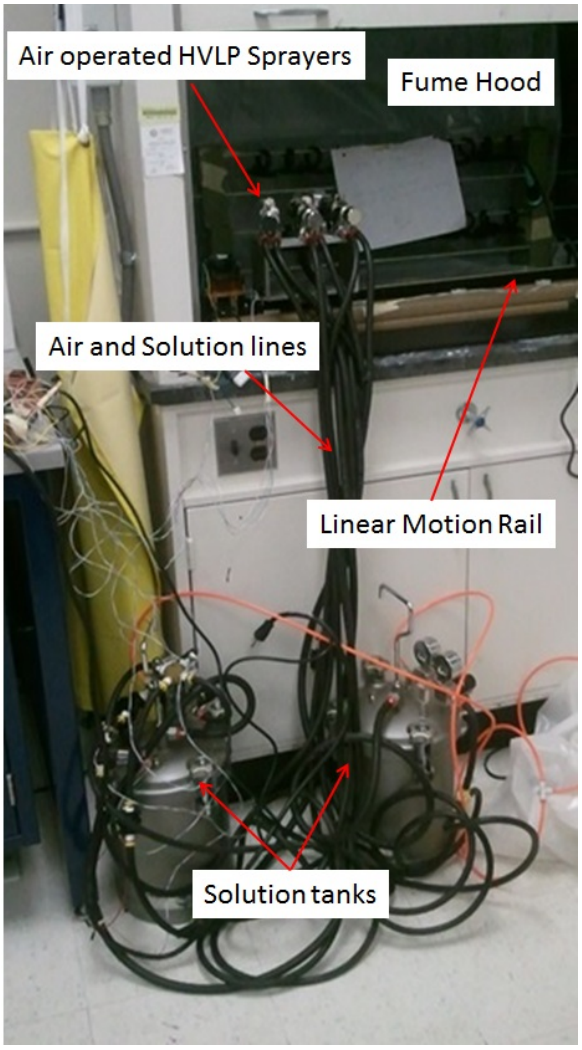

Figure 2.9: Automated LDSM

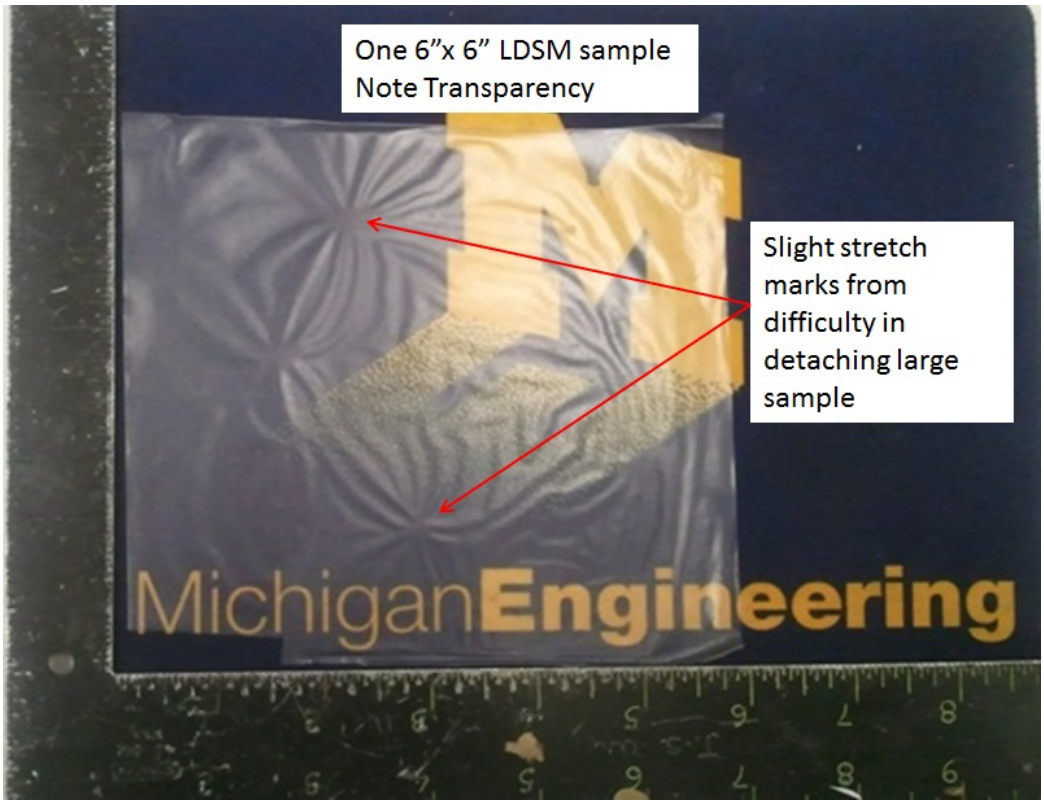

Figure 2.10: Detached LBL Film manufactured by LSDM

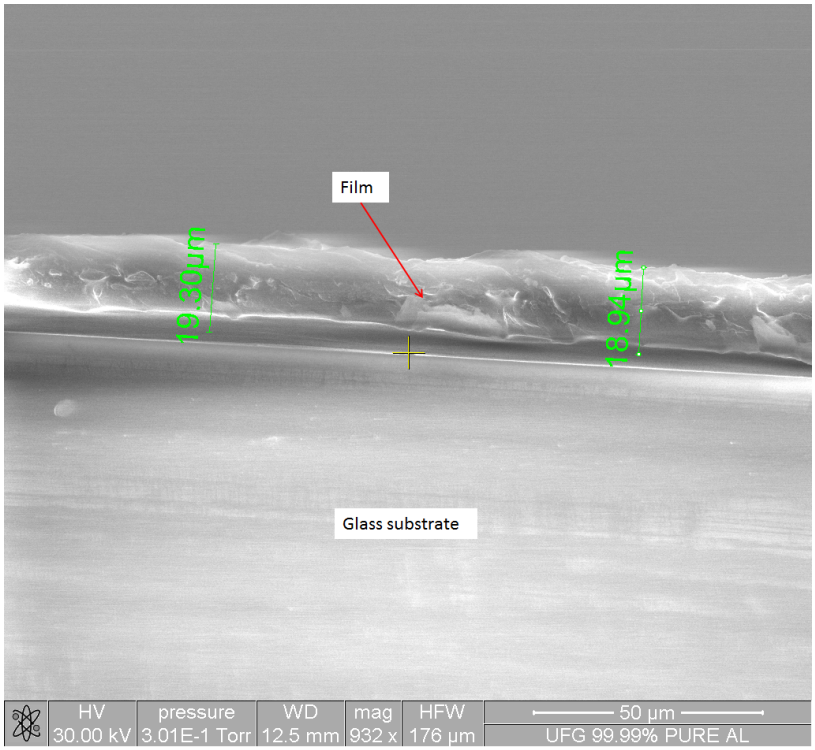

(a) Sample 1

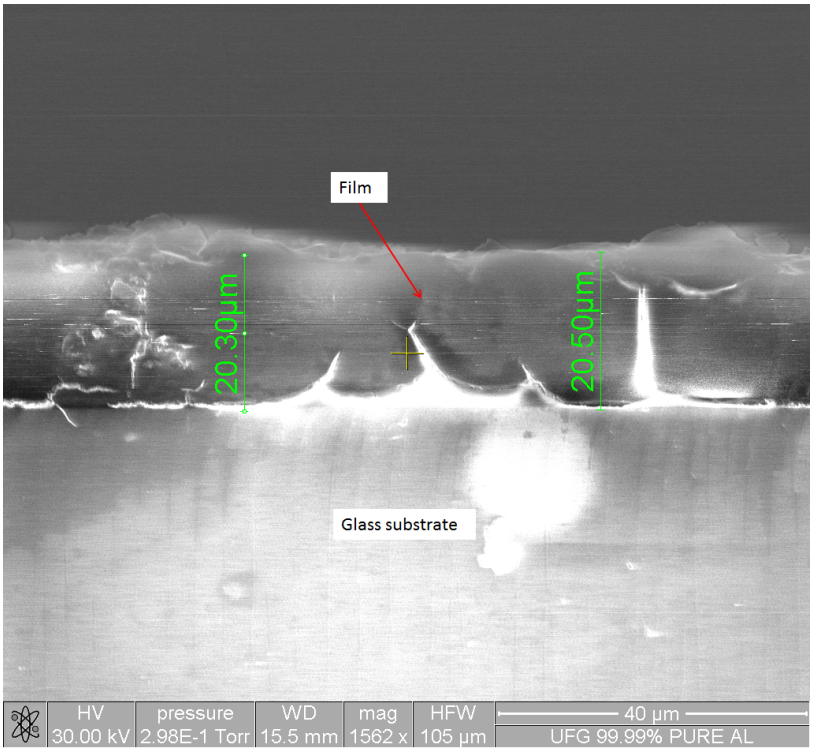

(b) Sample 2

Figure 2.11: Film Thickness of PU/PAA manufactured by LSDM

2.4 Assembly of Impact Test Specimens

The test assembly for impact consists of three layers: A 1.1mm thick borosillicate glass slide, the nanocomposite and a 1 inch thick borosillicate glass block. The nanocomposite is deposited by the LSDM on the glass slides, the nanocomposite is then bonded to a larger glass block. In order to bond the nanocomposite to the glass block, another layer of PU is deposted on the substrate and the substrate is rinsed, the borosillacate slide with the "wet" PU layer is then attached to the borosillicate glass block. This process results in similar bonding between the nanocomposite and the top glass slide, as well as the nanocomposite and the bottom glass block.

5" x 5" x 1" Borosillicate Glass blocks are obtained from Cincinatti Gasket.

2.5 Concluding Remarks

A novel automated manufacturing facility to deposit large sheets of Layer-by-layer nanocomposite films has been designed and manufactured. This facility allows us to perform tests on larger samples, increases the production rate, and enables much of the work presented in this dissertation.

CHAPTER III

EXPERIMENTAL DETERMINATION OF IN PLANE MODE I FRACTURE TOUGHNESS OF POLYURETHANE(PU)/POLY(ACRYLIC-ACID) NANOCOMPOSITE FILM

This chapter characterizes the fracture toughness of LBL manufactured thin films with elastic PU, a tough polymer, and PAA as a stiffening agent. A Single Edge-Notch Tension (SENT) specimen is used to study mode I crack propagation as a function of applied loading. Experimental results for the full-field time histories of the strain maps in the fracturing film have been analyzed to obtain R-curve parameters for the nanocomposite. In particular, by using the strain maps, details of the traction law are measured. A validated finite strain phenomenological viscoplastic constitutive model is used to characterize the nanocomposite film while a Discrete Cohesive Zone Model (DCZM) is implemented to model the fracture behavior. The LBL manufactured nanocomposite is found to display a higher fracture toughness than the unstiffened base polymer.

3.1 Characterization of the Mode I Fracture Toughness

Of concern in this paper is the characterization of fracture toughness of exponential LBL manufactured polymer nanocomposites composed of a water-soluble polymer and a water-soluble stiffening agent that has a good distribution of the hardening agent through the polymer matrix *Podsiadlo et al.* (2007), *Podsiadlo et al.* (2008). The exponential LBL method has lead to a significant reduction in the manufacturing time of the assembled films. The polymer and the stiffening agent are oppositely charged, resulting in strong ionic bonds between the polymer matrix and the hardening agent. In the present study, tough and elastic polyurethane is used as the base matrix polymer, and PAA is used as the stiffening agent, resulting in a nanocomposite with improved stiffness and considerable ductility.

When a pre-existing crack in these films is advanced by the application of mechanical loads, severe crack blunting is first observed with a large plastic zone surrounding the crack tip that dissipates energy. This plastic zone can activate several nanoscale mechanisms that leads to a R-curve response *Suo and Fan* (1992). The additional toughening is regarded as a basic material property that can be captured by a homogenized, non-linear traction-separation law, in conjunction with a suitable finite element simulation of specimen geometry and loading. In order to carry out this analysis, it is also necessary to characterize the constitutive response of the films undergoing finite deformation.

The fracture toughness is measured by carrying out a series of SENT mode-I fracture tests on free standing nanocomposite thin films (plane stress). Numerical simulation of the fracture tests in association with an accurate finite deformation constitutive model for the film material leads to a method that allows calculation of the fracture energy. In the numerical simulation, carried out using the commercial software ABAQUS, a DCZM *Xie and Waas* (2006) is implemented to represent the material ahead of the initial crack. During the quasi-static growth of the crack, an

increment of external work input is balanced by the sum of the stored strain energy, the plastic energy dissipated and the energy associated with fracture. Therefore the latter can be determined by knowing the plastic energy dissipated, the elastic energy stored and the external work done to advance the crack.

To accurately obtain the plastic energy dissipated while accounting for loading rate effects, the film's constitutive behavior has to be accurately modeled for both loading and unloading that occurs during the crack growth event. A phenomenological viscoplastic constitutive model, which is an extension of the Arruda-Boyce model *Arruda and Boyce* (1993), *Qi and Boyce* (2004), is used to capture the nonlinear large strain viscoplastic behavior with large residual plastic strains after unloading.

The DCZM elements which represent the fracture zone are prescribed through a nonlinear traction separation law which is iterated to match the numerical predictions to the experimental measurements. A traction separation law has two defining characteristics - the cohesive strength and the fracture toughness *Sun et al.* (2008). Since the cohesive strength can be determined from careful examination of the experimental strains, the fracture toughness distribution is the only unknown for which iteration is needed. The traction separation law numerically reproducing the experiment therefore provides the fracture toughness distribution in the fracture zone. The fracture toughness distribution that results in the best match of the numerical simulation to the experiment gives us insight to the toughening mechanisms at work in the fracture zone. R-curve behavior is observed along the fracture zone. A larger fracture toughness and cohesive strength are observed further from the initial crack, implying that both these quantities are increased as more plastic work is done in the neighboring substrate as the crack advances.

3.2 Experiments

3.2.1 Manufacturing the films and samples

The films are manufactured by alternately dipping glass slides into dilute aqueous dispersions ($1wt.\%$) of positively charged polyurethane and negatively charged poly(acrylic acid) to obtain the nanocomposite PU/PAA. To manufacture a single film, this process is repeated 100 times and produces a thin film that has an average thickness of $40\mu m$. The films are detached from the glass slide using hydro-fluoric acid and then dried in a heated chamber. Single-film samples are manufactured on standard microscope glass slides, resulting in a length of approximately 70mm and a height of 25mm. These are cut to the appropriate sizes for various characterization tests. A free standing film is shown in figure 3.1. The PU/PAA samples discussed in this paper are all five-film stacks, and are manufactured by pressing 5 single-film samples together in a heated hydraulic press at 110 °C and 15 MPa for 30 minutes. A pure cationic polyurethane (PU) sample is also made from the polyurethane solution by heating the solution in a petri dish, thereby removing the water molecules. The pure PU sample is studied for the purpose of comparison.

3.2.2 Tensile tests of the films

The strain rate-dependent properties of the films are measured by tensile tests using specimens illustrated in figure 3.2. Tensile test samples are manufactured to a total length of $25 \pm 1mm$, a gauge length of $13 \pm 2mm$ and a height of $2.5 \pm 0.5mm$. The tests were carried out on samples that were between $200\mu m$ to $300\mu m$ thick, under displacement control loading at nominal rates of 0.16mm/s and 0.016mm/s. Characteristic engineering stress-engineering strain curves for the samples are shown in figure 3.3. Strains are determined using optical images taken with a high resolution camera of a speckle pattern distributed on the surface of the film using acrylic paint

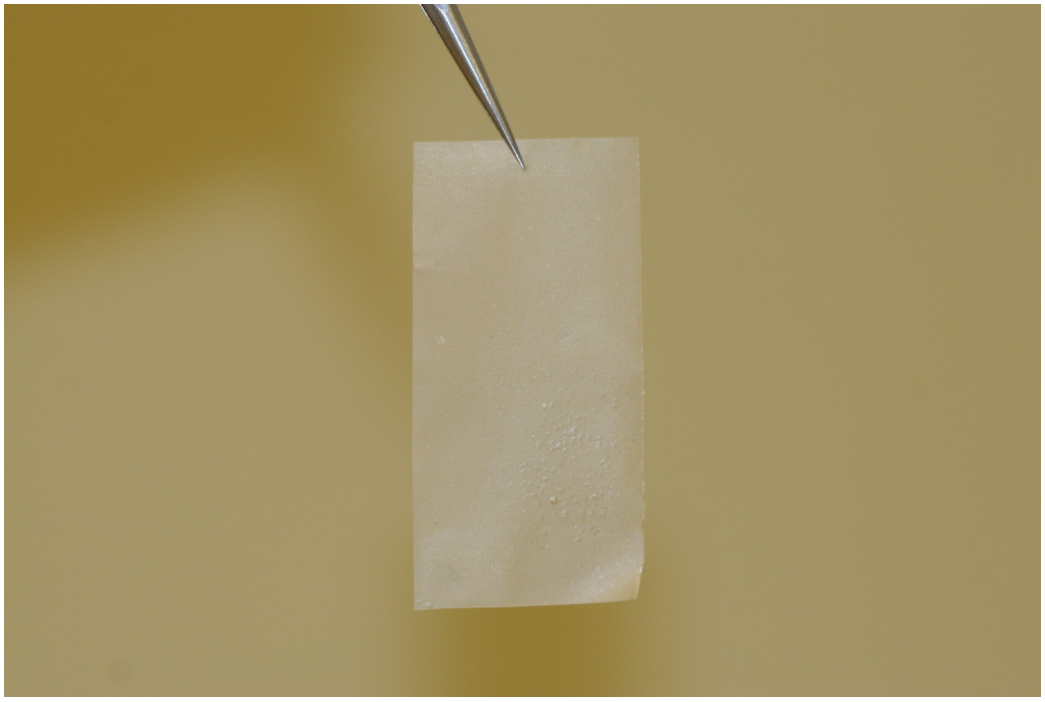

Figure 3.1: Photograph of translucent eLBL PU/PAA film after detaching and heating

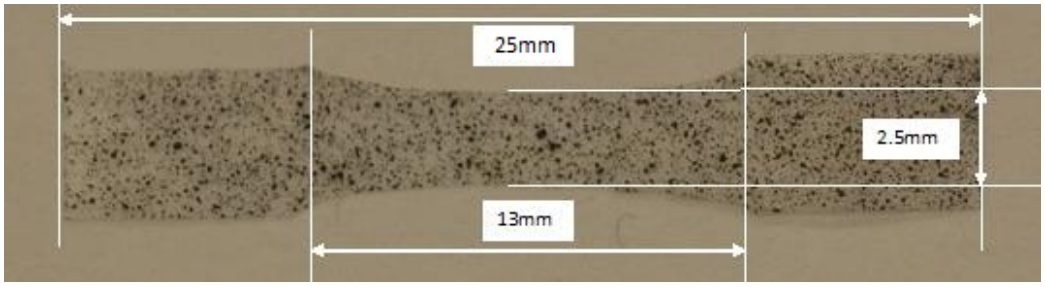

Figure 3.2: Tensile test specimens

applied with an airbrush, and the tensile force in the specimens is measured with a load cell attached to the mechanical testing machine. Thicknesses of the samples are measured with the aid of a scanning electron microscope. The samples are coated with a 5nm thick gold layer to prevent charging and damage of the sample in the scanning electron microscope. The tensile test results are used to characterize the film material for the finite element model that is used in the present work.

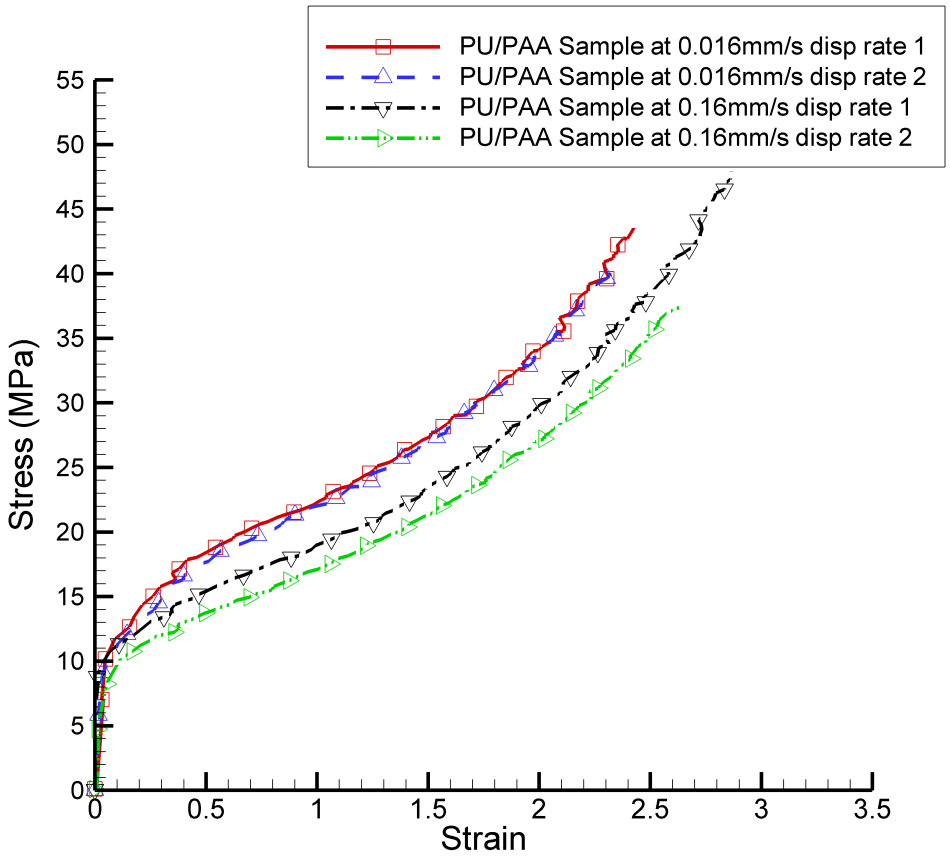

Figure 3.3: Characteristic engineering stress-engineering strain curves of 5 film PU/PAA stacks at different stretch rates

3.2.3 Single notch fracture tests

The fracture toughness of a thin film in plane stress is measured by matching numerical simulations to physical experiments of a single-edge notch tension mode-I fracture test. This section describes these experimental fracture tests.

The samples are attached to flat sample holders with a thin layer of epoxy and a single notch is made with a surgical razor blade in the film perpendicular to an edge as shown in figure 3.4. The free standing film between the sample holders is $5 \pm 0.3mm$ by $25 \pm 2mm$. The initial crack is cut to dimension of $4.5 \pm 0.5mm$, leaving an un-fractured height, h_0, of $20.5 \pm 0.5mm$. A fixed coordinate system is used to discuss the experimental results and associated numerical simulation results. The origin of the coordinate system is located along the expected crack plane, at the midpoint of the height of the specimen, as indicated in figure 3.4. The fracture tests are carried out on a displacement controlled table-top tensile test setup with a step-motor drive. The setup is shown in figure 3.5. The displacement rate is set to 0.003mm/s. Images of the speckle pattern are captured once every ten seconds. The displacement between the sample holders is measured with a Linear Variable Differential Transformer (LVDT) and is confirmed with the data obtained from the speckle pattern. The tensile forces are measured with a 150N load cell. The resolution of the load cell is 0.0068N, which corresponds to a resolution in stress of 0.0013MPa. The resolution of the LVDT is 0.00012mm. The strain resolution of the digital image correlation technique is 0.001.

3.2.4 Force displacement description of fracture tests

The PU/PAA samples all fractured in a uniform manner, with the crack propagating cleanly through the un-fractured height of the sample in the middle (the "ligament") of the sample. Figures 3.6 describe the fracture. The data set for the PU/PAA samples show minimal variation - samples 1, 2 and 3 represent a repeatable

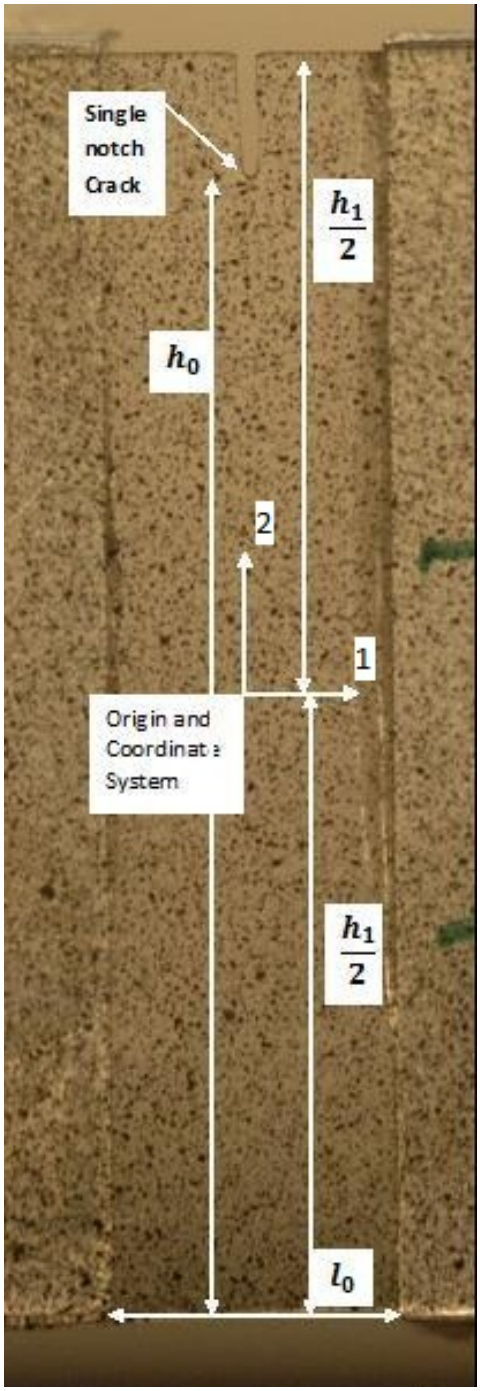

Figure 3.4: Dimensions of Experimental setup of film samples

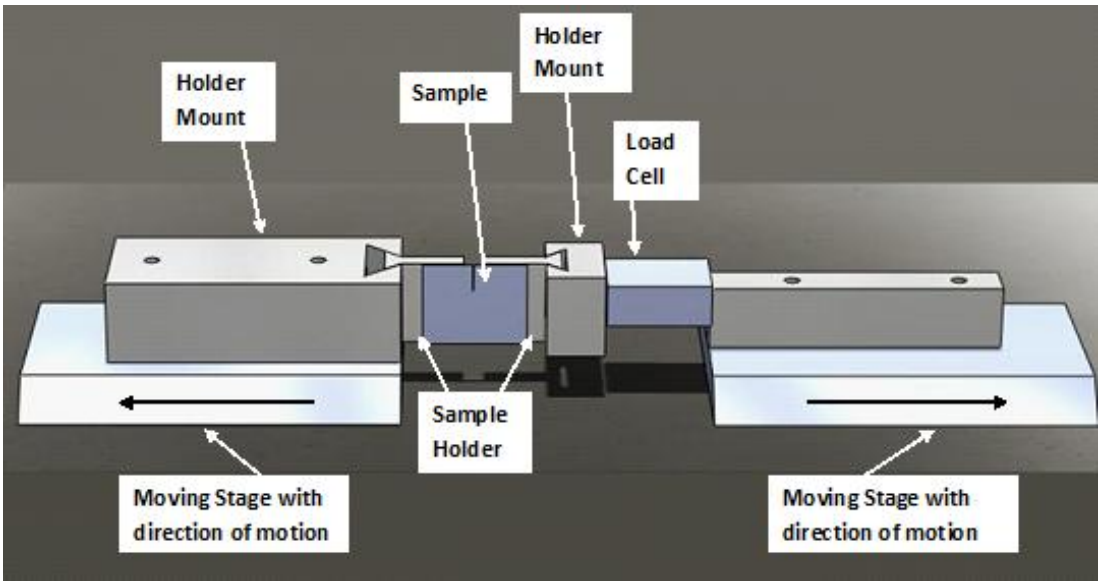

Figure 3.5: Experimental Setup

data set. These curves are shown in figure 3.7.

The data set for the pure PU samples also shows minimal variation, the two samples tested agree with each other. These curves are shown in figure 3.8. The PU/PAA samples have a maximum stress of 16 MPa and a maximum normalized displacement of 1.45. The PU/PAA samples also have an overall energy density of 80.9 N/mm. This energy density is obtained by normalizing the total energy expended by the ligament cross-sectional area. It is noted that the overall energy density includes the energy expended in the plastic deformation of the substrate as well as the fracture of the specimen. The PU fracture tests show that the pure polyurethane has a much lower maximum stress of 4 MPa, but a higher normalized displacement of 4.16. The overall energy density of pure PU is 58.2 N/mm. Figure 3.8 is a comparison of the normalized force against normalized displacement curves for pure PU and PU/PAA.

3.2.5 Crack location of fracture tests

The speckle patterns on either side of the crack tip are analyzed by following the deformation history of selected isolated speckles on either side of the crackpath. For

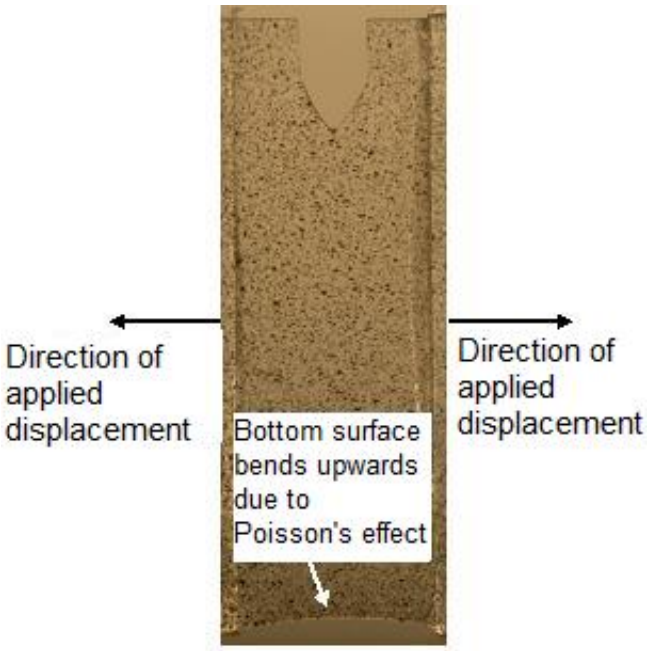

(a) Experimental photograph of Fracture at timestep t

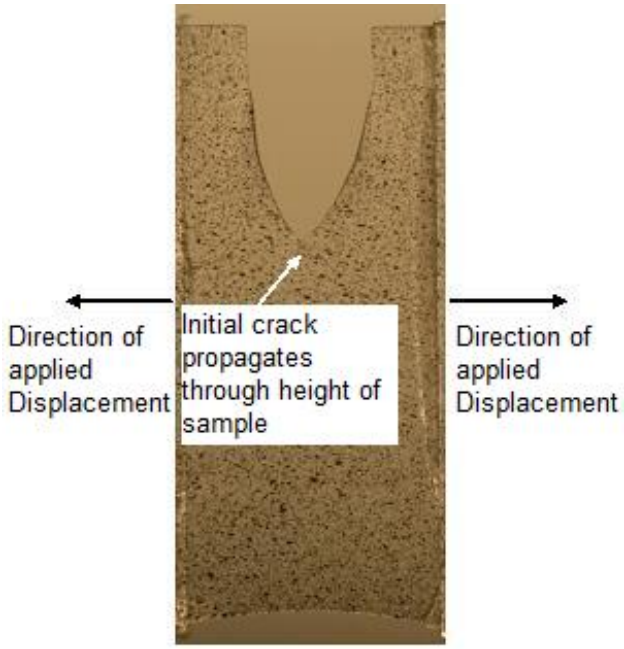

(b) Experimental photograph of Fracture at timestep $t + \delta t$

Figure 3.6: Description of Fracture

Initial crack propagates through the height of the sample, resulting in fast fracture.

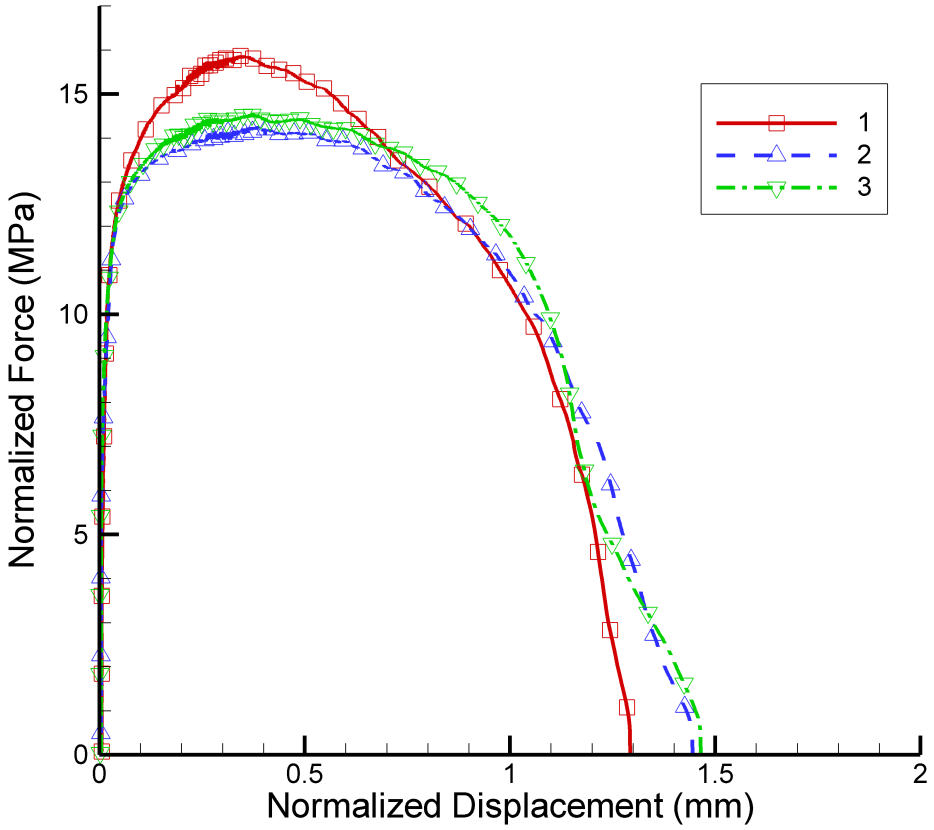

Figure 3.7: Normalzed fracture curves for 5 film PU/PAA stacks

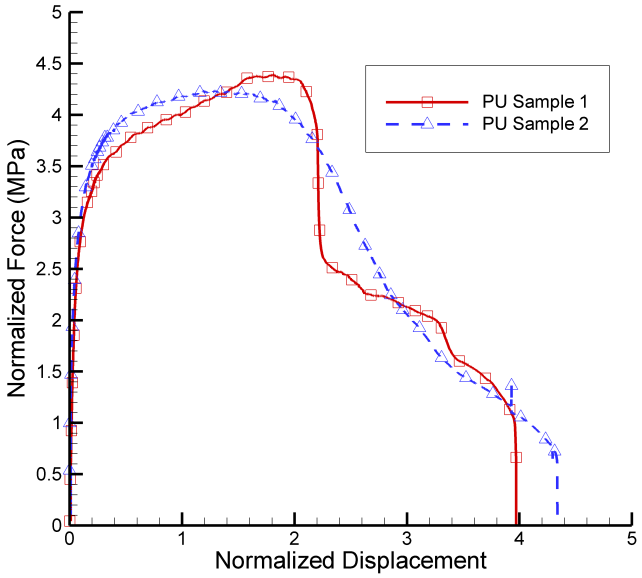

(a) Normalized fracture curve for pure polyurethane

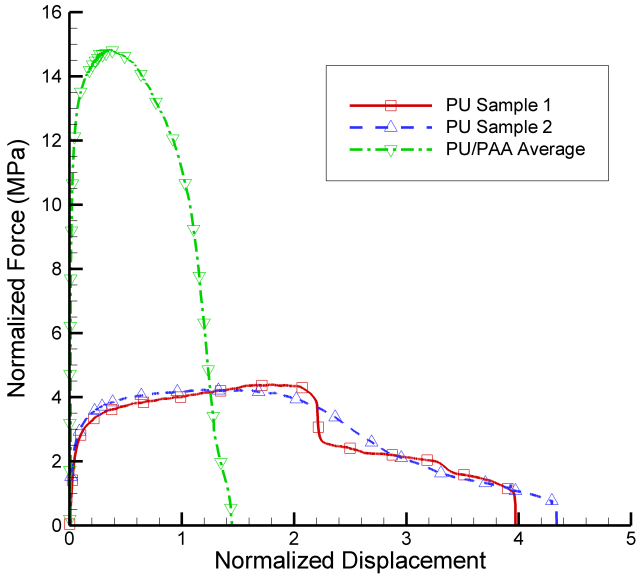

(b) Normalized fracture curve for pure polyurethane and 5 film PU/PAA Stack

Figure 3.8: Normalized fracture curves for (a)pure polyurethane and (b)PU/PAA and pure polyurethane

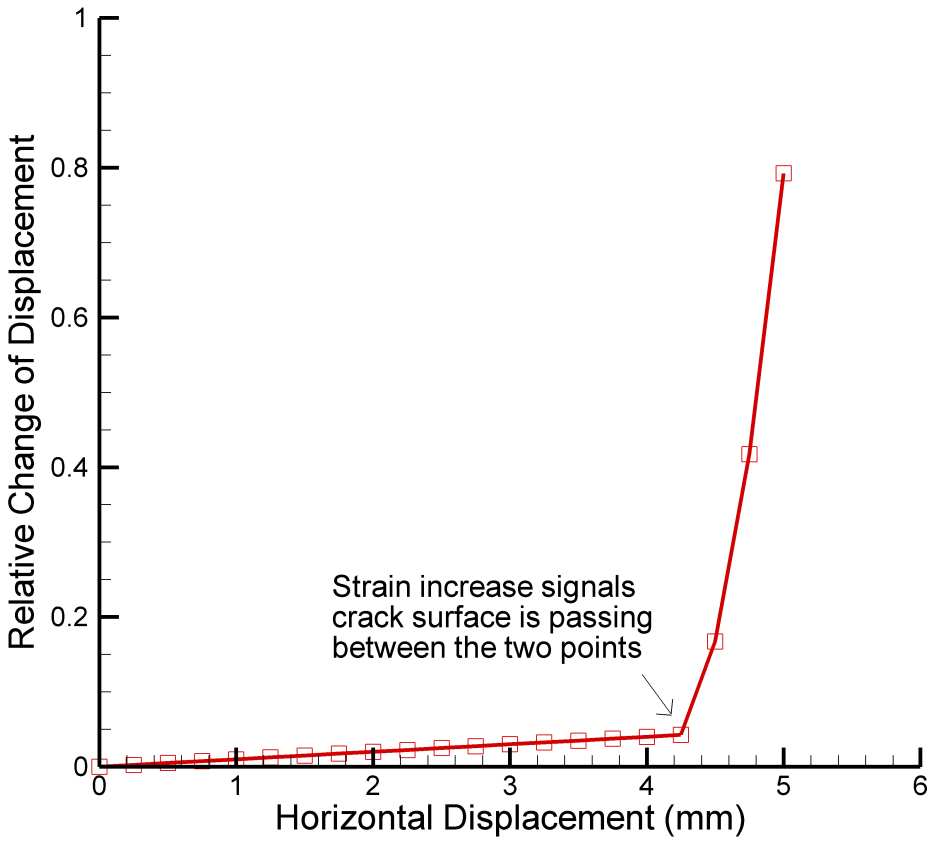

Figure 3.9: Sample strain of two dots on either side of crack surface

each unique pair of speckles, the relative change of distance-horizontal displacement plots are obtained as in figure 3.9. It is determined that the crack has moved between a pair of speckles when the rate of relative change of distance between them increases abruptly, indicating that the material between them has broken at that time step. In this manner, the instantaneous crack position as a function of time, and hence, as a function of external load is recorded. A typical crack position graph for the PU/PAA sample is shown in figure 3.10.

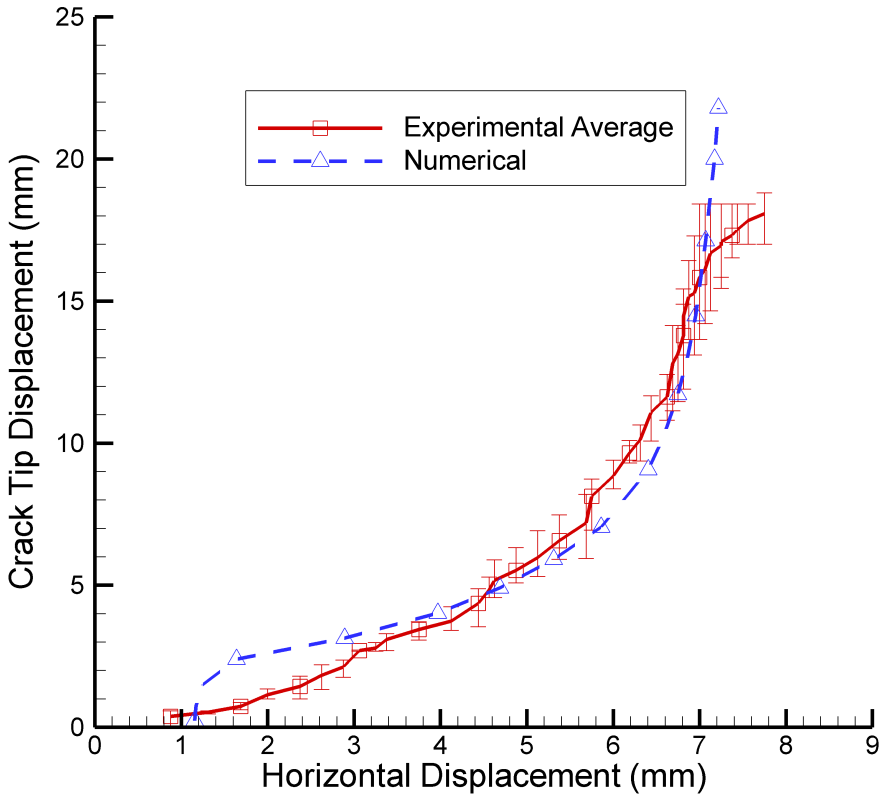

Figure 3.10: Comparison of Experimental and Numerical Crack Position Curves for 5 film PU/PAA stack

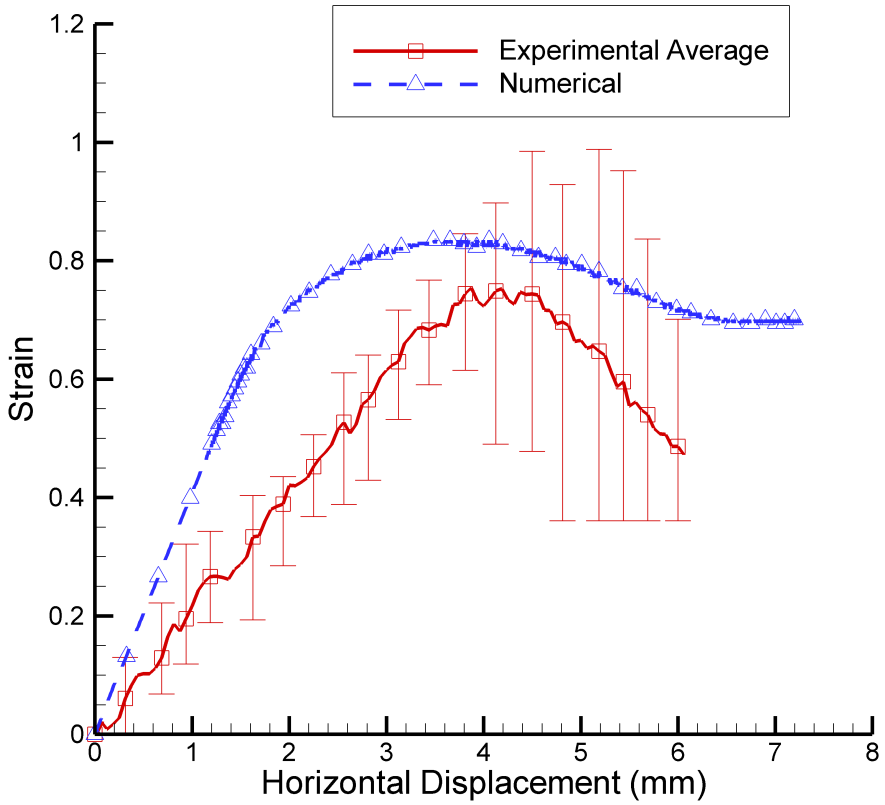

Figure 3.11: Comparison of Experimental and Numerical Strain Curve at Y=5mm for 5 film PU/PAA stack

3.2.6 Strain map of fracture tests

In addition to the force-displacement data, the speckle images are analyzed to gather other local information. The stretches in the 1 direction are analyzed at specific points in the specimen as the crack grows. Partial unloading is observed as the crack moves past specific points. Plots for the PU/PAA samples are included in figure 3.11 and 3.12.

The Lagrangian strain tensor E_{ij} can be related to several deformation measures as shown in *Fung* (1969). The E_{11} component strain is related to the principal stretch λ_1 through:

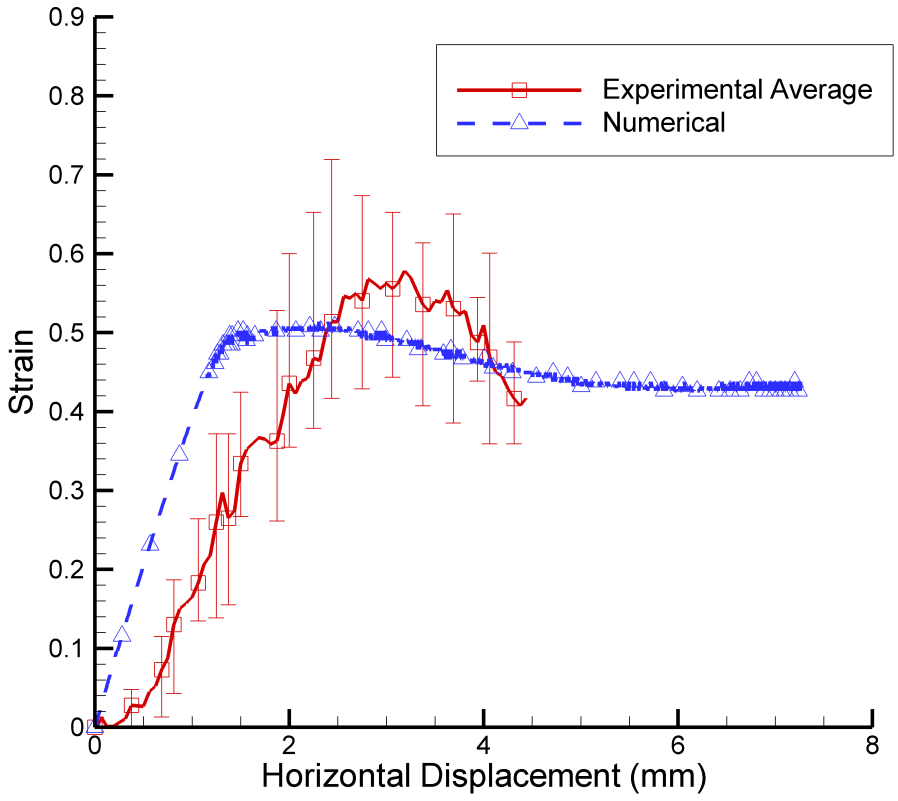

Figure 3.12: Comparison of Experimental and Numerical Strain Curve at Y=7.5mm for 5 film PU/PAA stack

$$\lambda_1 \;=\; \sqrt{1+2E_{11}} \tag{3.1}$$

where

$$E_{11} \;=\; \frac{du_1}{dX_1} \;+\; \frac{1}{2}\left[\left(\frac{du_1}{dX_1}\right)^2 \;+\; \left(\frac{du_2}{dX_1}\right)^2\right] \tag{3.2}$$

and,

$$u_i \;=\; x_i \;-\; X_i. \tag{3.3}$$

Here, u_i is the i^{th} displacement component which is related to the undeformed, X_i, and deformed, x_i, coordinates of the material point being analyzed.

3.2.7 Full-field strain maps and fracture stress calibration

In addition to the stretches computed as described above, Aramis software version 1.6 is used to calculate strain maps of the sample during deformation. A sample strain, E_{11}, map is shown in figure 3.13. The Aramis strain maps show that a strain concentration moves ahead of the crack tip. The onset of the strain concentration signals the activation of the fracture event. Consider a horizontal line drawn across the Aramis plot in figure 3.13. It is seen that the E_{11} strain is uniform across this horizontal cross section. The same horizontal line is drawn in figure 3.13 and here it is noted that the E_{11} strain is no longer uniform. This indicates that the strain at the centerline is higher than near the grips. This strain concentration indicates that there is softening in this region, allowing the strain to increase much more at this location for a given state of loading. This softening is associated with the rate dependent plastic energy that is dissipated while the crack is advancing, consequently, capturing this plastic dissipation accurately is needed in order to extract the fracture toughness of the films. The stress at which the fracture event is activated can be identified

by examining the true stress-true strain curve from the material characterization tests. Since the full-field strains are extracted from the Aramis data, correlating this strain to the true stress-true strain curve allows determination of the local stress. This process is repeated for different points along the centerline and a fracture stress calibration is obtained in the form of an R-curve *Gdoutos* (1990), *Suo and Fan* (1992). The experimental fracture stresses as a function of position as well as the R-curve representing the changing resistance to crack advance are shown in figure 3.16. This measured distribution of cohesive strength is important in establishing numerical models for studying fracture of these films.

In addition, strains along various sections drawn in figure 3.13 are expressed in figure 3.14. It is observed that strains are concentrated most in sections closest to the crack tip. At sections far enough from the crack tip, strains along the section are uniform.

These higher strain concentrations near the crack tip are an expression of the substrate strain and crack process zone growth. A schematic of what is occurring in the process zone is shown in figure 3.15. The higher crack process zone opening nearest the crack tip contributes to the higher strain in this region.

It is noted that the critical stresses presented in this section are much lower than the failure stresses shown in the uniaxial tension test in figure 3.3. This phenomenon is explained later in section 4.2.5. In addition, the strain fields observed by the Digital Image Correlation program are averaged over an area. This results in lower strain and stress concentrations than if strains were measured at a point or provided by the analytic solution. This phenomenon is illustrated in figure 3.17, which is a graph of the strain variation of a linear elastic solid, which is proportional to, $\frac{K}{\sqrt{2x\pi}}$, normalized by $\frac{K}{\sqrt{2\pi}}$, as a function of displacement to the crack tip along a line ahead of the crack tip *Anderson* (2005). In addition, the strains are averaged over various lengths measured from the crack tip, showing that the average strains are lower than

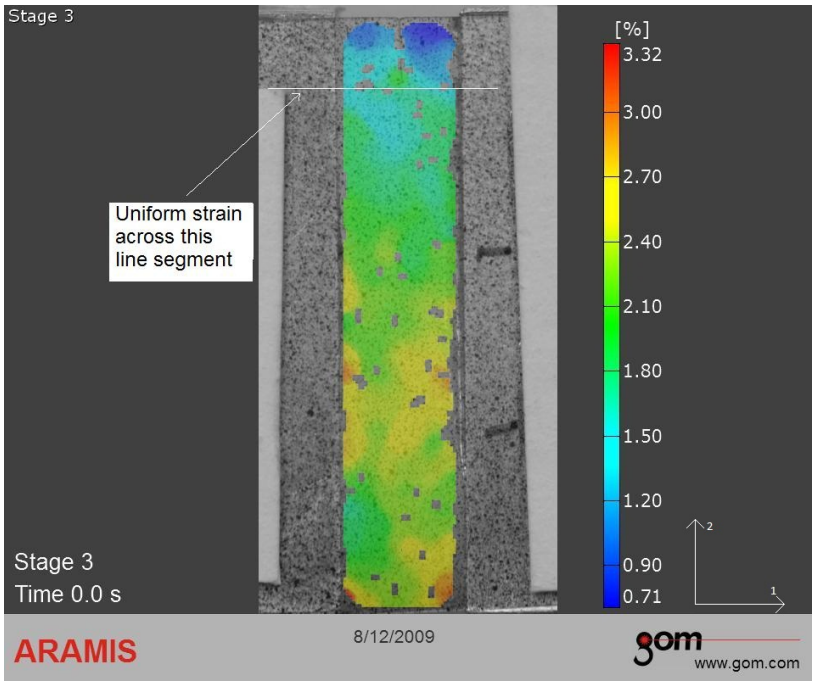

(a) Strain map at timestep 90s (0.0584mm,41.21N)

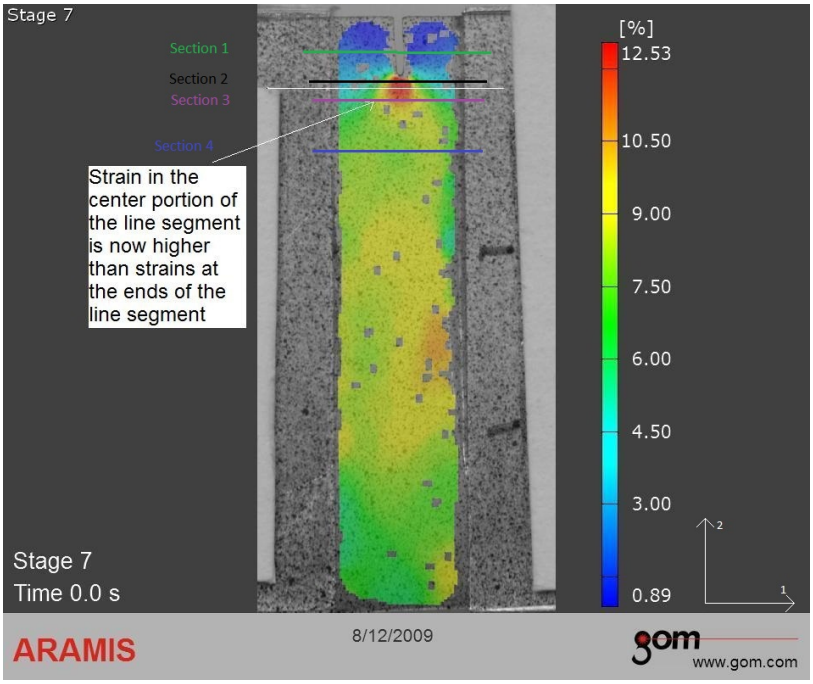

(b) Strain map at timestep 210s (0.3756mm, 68.16N)

Figure 3.13: Aramis Strain Maps

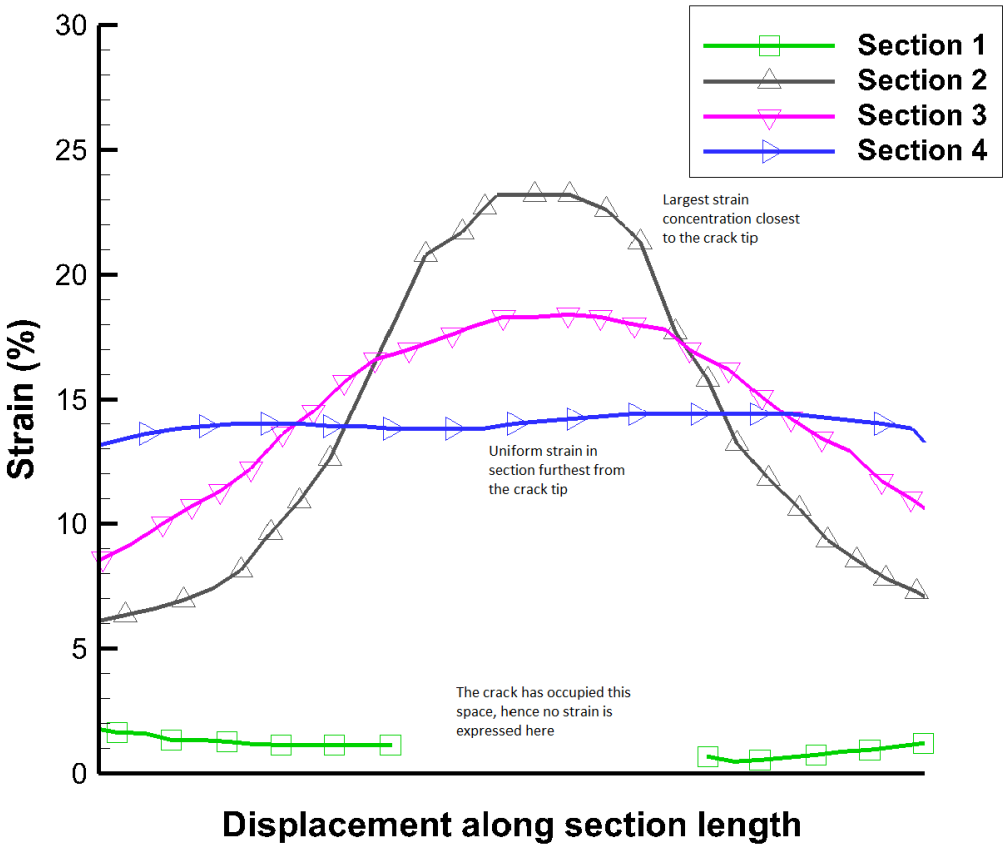

Figure 3.14: Section Strains

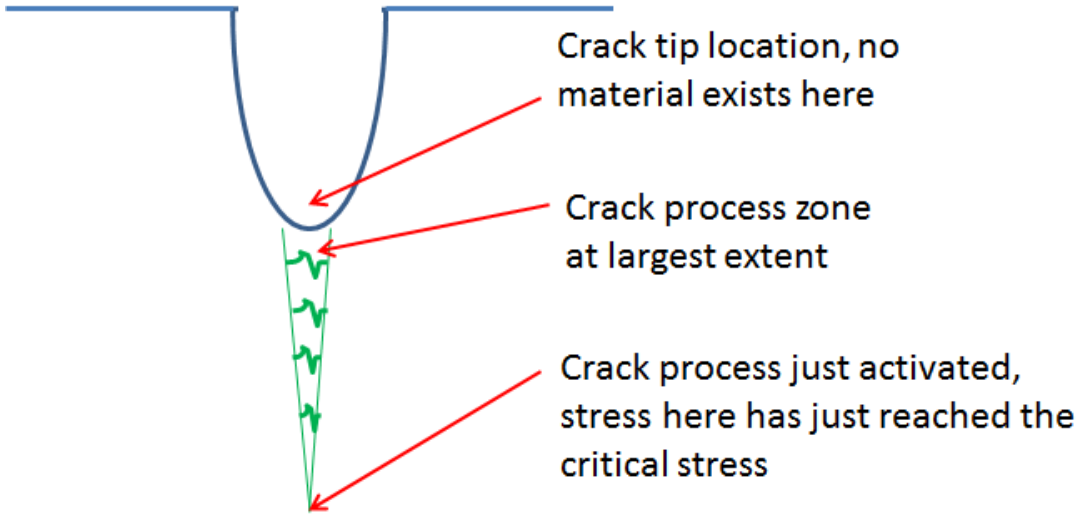

Figure 3.15: Crack Process Zone

the maximum strain observed in that interval, and the amount the average strains are lower than the maximum value is dependent on the length over which strains are averaged. The measurement of the strains over an area necessarily result in a lower measured critical strain and therefore, a lower measured critical stress as well. This is acceptable because the finite element method used to characterize the fracture toughness later on also results in averaged and lower critical stresses than the analytical solution.

3.3 Finite Element Model

3.3.1 Description of the PU/PAA constitutive model

The large deformation stress-strain behavior of the polymer nanocomposite shows the following response:

1. Nonlinear large strain visco-plastic behavior

2. Strain rate dependence which is low but is present

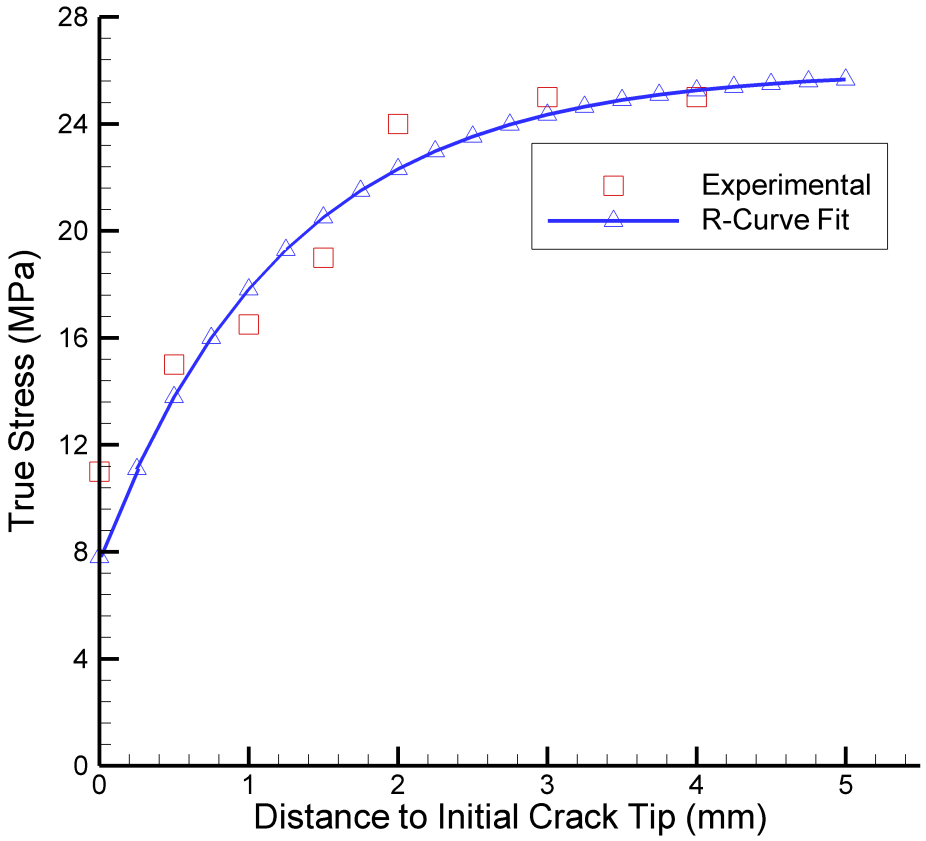

Figure 3.16: Stress Calibration for PU/PAA

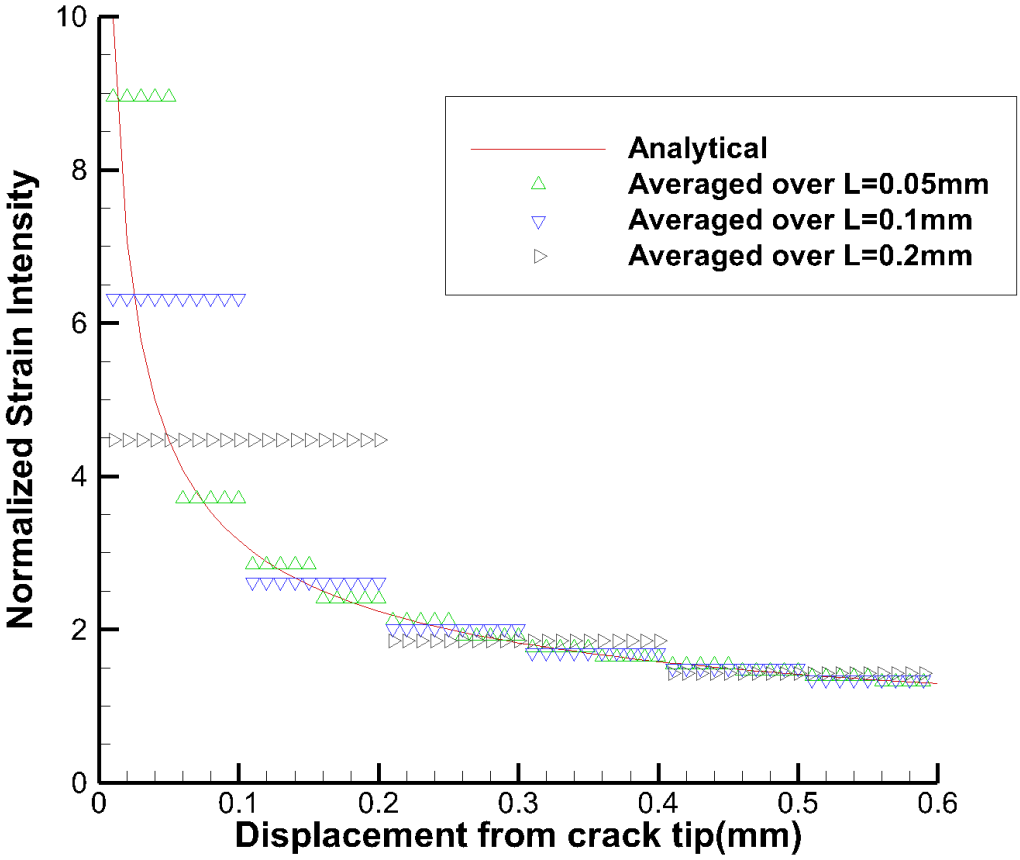

Figure 3.17: Strain Intensity

3. High plastic strains after unloading.

A phenomenological viscoplastic constitutive model was developed that captures the observed macroscopic mechanical response of the material. The kinematics of the constitutive model developed for the PU/PAA polymer nanocomposite is based on that for thermoplastic polyurethane (TPU), developed by Qi and Boyce *Qi and Boyce* (2004), *Qi and Boyce* (2005), a schematic representation of which is shown in figure 3.18. There are two branches that are in parallel - a non-linear spring branch which is based on the 8-chain Arruda-Boyce model, *Arruda and Boyce* (1993), and the elasto-viscoplastic component, which in turn consists of a linear elastic spring and a viscoplastic dashpot. The macroscopic deformation gradient $\mathbf{F}$ acting on both these branches is the same and the total Cauchy stress $\mathbf{T}$ is the sum of the contributions from each branch.

$$\mathbf{F}^N = \mathbf{F}^V = \mathbf{F} \tag{3.4}$$

$$\mathbf{T} = \mathbf{T}^V + \mathbf{T}^N \tag{3.5}$$

where, the superscript N refers to the Non-linear hyperelastic spring and V to the visco-plastic branch in the model.

The hyperelastic rubbery spring captures the entropy change due to the orientation and stretching of the molecular network. The 8-chain model developed by Arruda and Boyce, *Arruda and Boyce* (1993), is used in computing the stresses as it captures the equilibrium large stretch behavior accurately. Volume changes are neglected in this branch by computing the stresses based on the deviatoric part of the macroscopic deformation gradient as shown below. The reader is refered to *Arruda and Boyce* (1993) for more details of the present model. The expression for the Cauchy stress in this branch is a function of the

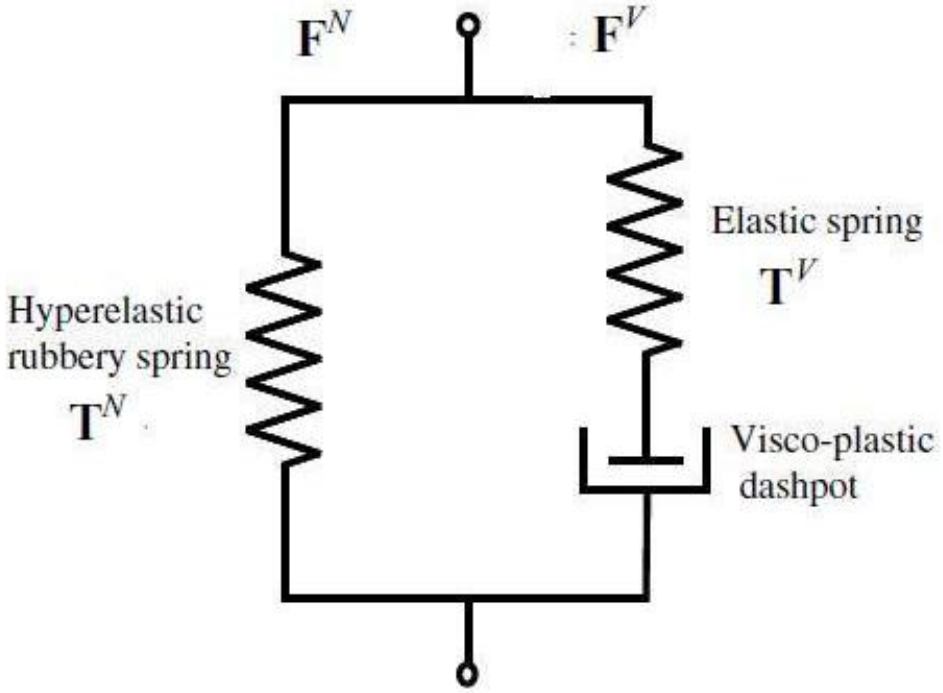

Figure 3.18: Constitutive Model

$$\mathbf{T}^N = \frac{\mu_r}{3J}\frac{\sqrt{N}}{\lambda_{chain}} L^{-1}\left(\frac{\lambda_{chain}}{\sqrt{N}}\right)\bar{\mathbf{B}}' \tag{3.6}$$

$$\lambda_{chain} = \sqrt{\frac{\overline{\lambda}_1^2 + \overline{\lambda}_2^2 + \overline{\lambda}_3^2}{3}} \tag{3.7}$$

$$\bar{\mathbf{F}}^N = J^{-1/3}\mathbf{F}^N \tag{3.8}$$

$$\bar{\mathbf{B}} = \bar{\mathbf{F}}^N \bar{\mathbf{F}}^{N^T} \tag{3.9}$$

$$\bar{\mathbf{B}}' = \bar{\mathbf{B}} - \frac{1}{3} tr\left(\bar{\mathbf{B}}\right)\mathbf{I} \tag{3.10}$$

$$L^{-1}(\xi) \approx \xi\frac{3-\xi^2}{1-\xi^2} \tag{3.11}$$

where $\mu_r = nk\Theta$, with n being the chain density (number of molecular chains per unit reference volume) of the underlying macromolecular network, k is the Boltzmann's constant and Θ is the absolute temperature. N is the number of "rigid links" between two crosslinks and B is the isochoric left Cauchy-Green tensor. λ_{chain} is the stretch on each chain in the eight-chain network that is computed based on the squares of the principal stretches λ_1, λ_2 and λ_3, which are obtained by the spectral decomposition of the left Cauchy-Green strain tensor.

The elasto-viscoplastic branch has a multiplicative split of the deformation gradient, which is used in computing the part of the deformation seen by the linear elastic spring. The initial elastic part of the overall nonlinear macroscopic response of the material is accounted for through the stress contribution from the linear spring.

$$\mathbf{F}^V = \mathbf{F}^{Ve}\mathbf{F}^{V\upsilon} \tag{3.12}$$

where $\mathbf{F}^{Ve}$ is the deformation gradient of the elastic spring and $\mathbf{F}^{V\upsilon}$ is the deformation gradient of the visco-plastic dashpot. Furthermore, the decomposition of the velocity gradient L_V gives

$$\mathbf{L}^V = \dot{\mathbf{F}}^V \mathbf{F}^{V^{-1}} = \dot{\mathbf{F}}^{Ve} \mathbf{F}^{Ve^{-1}} + \mathbf{F}^{Ve} \dot{\mathbf{F}}^{V\upsilon} \mathbf{F}^{V\upsilon^{-1}} \mathbf{F}^{Ve^{-1}} \tag{3.13}$$

$$\mathbf{L}^{V\upsilon} = \dot{\mathbf{F}}^{V\upsilon} \mathbf{F}^{V\upsilon^{-1}} = \mathbf{D}^{V\upsilon} + \mathbf{W}^{V\upsilon} \tag{3.14}$$

where $\mathbf{D}^{V\upsilon}$ and $\mathbf{W}^{V\upsilon}$ are the rate of stretching and the spin, respectively.

Without loss of generality, we take **?**

$$\mathbf{F}^{Ve} = \mathbf{V}^{Ve} \mathbf{R}^{Ve} \tag{3.15}$$

$$\mathbf{T}^V = \frac{1}{det \mathbf{F}^{Ve}} \mathbf{L}^e \left(\ln \ \mathbf{V}^{Ve} \right) \tag{3.16}$$

$$\mathbf{W}^{V\upsilon} = 0 \tag{3.17}$$

where, Le is the fourth-order tensor modulus of elastic constants; $\mathbf{V}^{Ve}$ and $\mathbf{R}^{Ve}$ are the left stretch tensor and the rotation tensor, obtained from the polar decomposition of the elastic deformation gradient.

The visco-plastic stretch rate $\mathbf{D}^{V\upsilon}$ is constitutively prescribed as

$$\mathbf{D}^{V\upsilon} = \frac{\dot{\gamma}^\upsilon}{\sqrt{2}\bar{\tau}_\upsilon} \bar{\mathbf{T}}^{V'} \tag{3.18}$$

where $\dot{\gamma}^\upsilon$ denotes the visco-plastic shear strain rate and τ_V is the equivalent shear stress. The constitutive equation for the evolution of visco-plastic shear strain rate is given as

$$\dot{\gamma}^{v} \;=\; \dot{\gamma}_0 exp\left[-\frac{A\cdot s}{k\Theta}\left[1-\left(\frac{\bar{\tau_V}}{s}\right)\right]\right] \tag{3.19}$$

in which $\dot{\gamma}_0$ is the pre-exponential factor proportional to the attempt frequency and s is the athermal shear strength, which represents the resistance to the visco-plastic shear deformation.

$$\bar{\tau_V} = \left[\frac{1}{2}\bar{\mathbf{T}}^{V'} : \bar{\mathbf{T}}^{V'}\right] \tag{3.20}$$

The rate and temperature dependency of the material is captured within the evolution equations for the dashpot.

The uniaxial tension tests performed on PU/PAA polymer nanocomposite helps in understanding the overall macroscopic response of the material during loading and unloading. In the use of the constitutive model for the numerical computation of fracture toughness, it is essential to fit both the loading and unloading, so as to accurately match the area under the stress-strain curve. On comparing the mechanical behavior of polyurethane with that of PU/PAA nanocomposite, we notice significantly higher residual plastic strains after unloading in the latter. The evolution in the athermal shear strength is essential in fitting the unloading response of the polymer nanocomposite. *Boyce et al.* (1988)

$$\dot{s} \;=\; h\left(1-s/s_{ss}\right)\dot{\gamma}^{p} \text{ with,} s\left(0\right) \;=\; s_0 \; s\left(\infty\right) \;=\; s_{ss} \tag{3.21}$$

where h is a measure of the rate of increase in s.

3.3.2 Implementation of the constitutive model and identification of material parameters

A fully three-dimensional model based on the described constitutive equations was implemented as a user defined material (umat) subroutine in the commercial finite element application Abaqus. This subroutine was used in running simulations at the same strain rates as used in the experimental uniaxial tensile tests. The material parameters were varied to fit the true stress vs. true strains for the polymer nanocomposite. All simulations were run at a constant temperature of 296 K with prescribed displacement vs. time function.

Comparison of the results from the uniaxial tension experiments and the simulations show the following key characteristics of the constitutive model. These are compared in figures 3.19 through 3.21 for slow through fast rates of strain.

- The general nonlinear response of the material during loading is matched well as we observe the initial elastic response followed by the strain hardening and finally the steep rise in the stresses.

- The low strain rate dependency is incorporated by adjusting the parameters associated with the viscoplastic dashpot.

- The shape of the unloading curve and the residual plastic strains can be satisfactorily matched with the experimental results. This allows for a good comparison of the area under the loading-unloading curve in both the experiments and simulation.

The determination of material parameters was done based on the experimental data. The value of Young's modulus E was found by measuring the initial slope of the stress-strain curve. Poisson's ratio ν was taken to be 0.30. The initial athermal shear

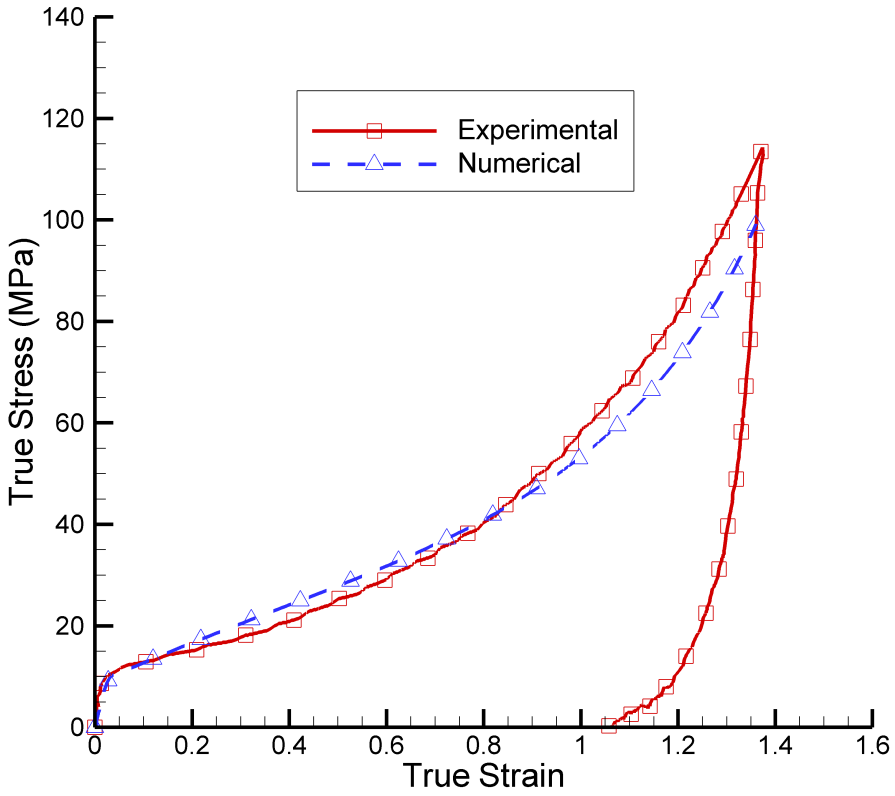

Figure 3.19: Experimental and Numerical Substrate Model Comparison of PU/PAA at 0.005/s

yield strength s_0 is calculated from the elastic constants (refer to table 1). The strain rate and temperature dependence of the initial yield are modeled with the material constants $\dot{\gamma}_0$ and A. To obtain these constants, (3.19) is rearranged to be an equation for a line

$$ln(\dot{\gamma}^v) = B + C(\frac{\bar{\tau}_v}{S}) \tag{3.22}$$

$$C = \frac{A \cdot S}{k\Theta} \tag{3.23}$$

$$B = ln(\dot{\gamma}_0) - C \tag{3.24}$$

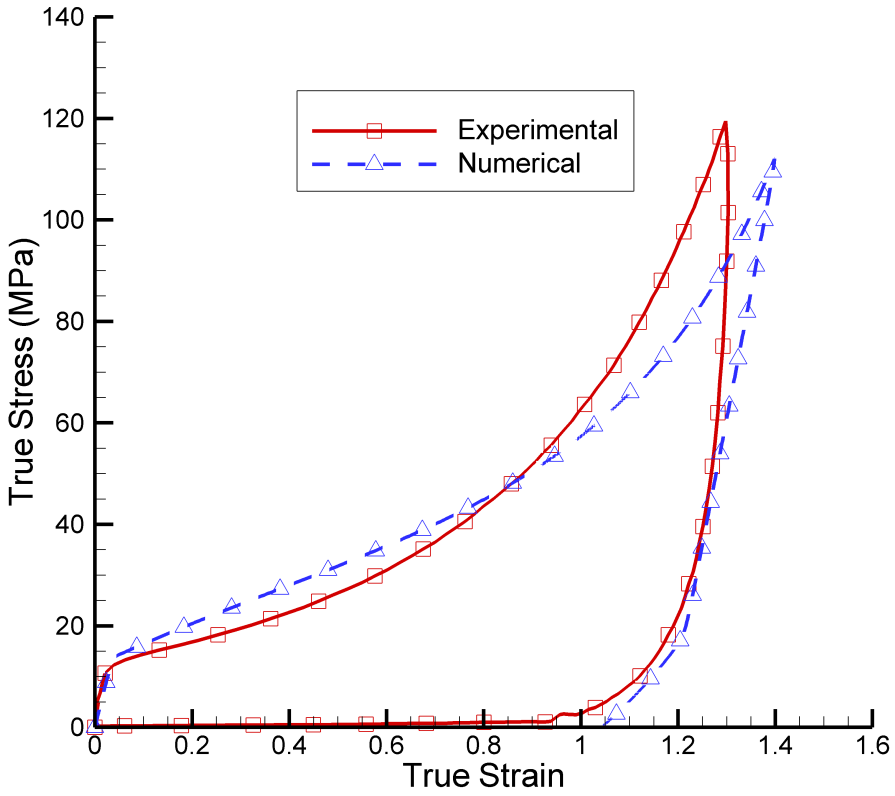

Figure 3.20: Experimental and Numerical Substrate Model Comparison of PU/PAA at 0.05/s

The tensile locking stretch $\sqrt{N}$ can be estimated by computing the limiting strain found from the stress-strain curves e^{ϵ_l}. An initial approximation for μ_r can be determined by measuring the initial slope of the strain hardening curve in the experimental data. The parameters, h and s_{ss}, are found by trial and error method, to find the best fit for both the loading and unloading part of the curve.

The material parameters identified for the PU/PAA nanocomposite are given in the following table:

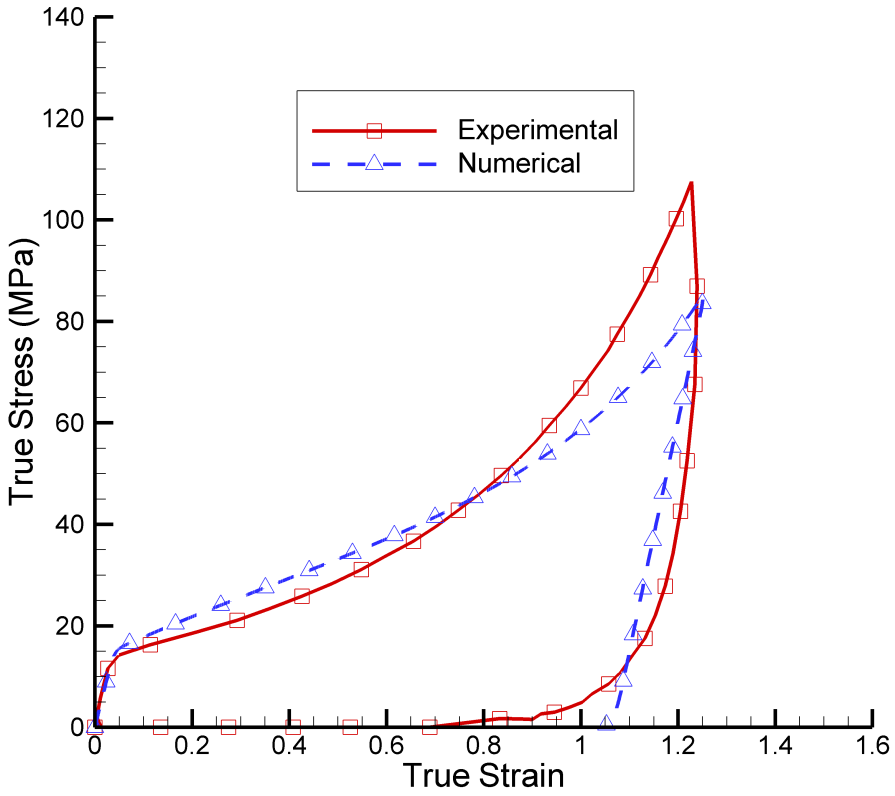

Figure 3.21: Experimental and Numerical Substrate Model Comparison of PU/PAA at 0.1/s

3.3.3 Description of the Polyurethane material model

Modeling of the mechanical response of Polyurethane is done based on the same phenomelogical approach taken for the PU/PAA polymer nanocomposite. As a first attempt to model the Polyurethane films, the constitutive model for thermoplastic polyurethanes by Qi and Boyce *Qi and Boyce* (2005) was used. This model presents a limitation in accurately simulating both the loading and unloading part of the uniaxial tests. Hence, the constitutive model for the polymer nanocomposite is applied and the material parameters identified based on the experimental results from Polyurethane films. The comparison of the material behavior of Polyurethane with respect to the PU/PAA clearly shows a comparatively lower initial elastic stiffness

Material Property	Symbol	Value
Young's Modulus	E	$620\,[MPa]$
Poisson's Ratio	υ	0.30
Pre-exponential factor	$\dot{\gamma}_0$	$10^5\,[s^{-1}]$
	A	$3.5 \bullet 10^{-18}\,[mm^3]$
Rate of resistance drop w.r.t. plastic strain	h	$60\,[MPa]$
	$C_r = nk\Theta$	$9.5\,[MPa]$
Locking Stretch	$\sqrt{N}$	$\sqrt{1.80}$
Initial athermal shear yield strength	s_0	$0.77\frac{\mu}{1-\mu}$
Steady state value of athermal yield strength	s_{ss}	$1.80 \bullet s_0$

Table 3.1: Material parameters for PU/PAA

and lower yield stress, which are reflected in the material parameters identified for Polyurethane. The material parameters for PU and PU/PAA capture the unloading part of the response after matching the loading part of the response consistently.

Comparison of the results from the uniaxial tension experiments and the simulations show the following key characteristics of the constitutive model. These are compared in figures 3.22 through 3.23 for slow through fast rates of strain.

The following are the material properties for PU:

Material Property	Symbol	Value
Young's Modulus	E	$50\,[MPa]$
Poisson's Ratio	υ	0.45
Pre-exponential factor	$\dot{\gamma}_0$	$0.1\,[s^{-1}]$
	A	$2.0 \bullet 10^{-17}\,[mm^3]$
Rate of resistance drop w.r.t. plastic strain	h	$5.5\,[MPa]$
	$C_r = nk\Theta$	$1\,[MPa]$
Locking Stretch	$\sqrt{N}$	$\sqrt{9.60}$
Initial athermal shear yield strength	s_0	$0.77\frac{\mu}{1-\mu}$
Steady state value of athermal yield strength	s_{ss}	$2.0 \bullet s_0$

Table 3.2: Material parameters for Pure PU

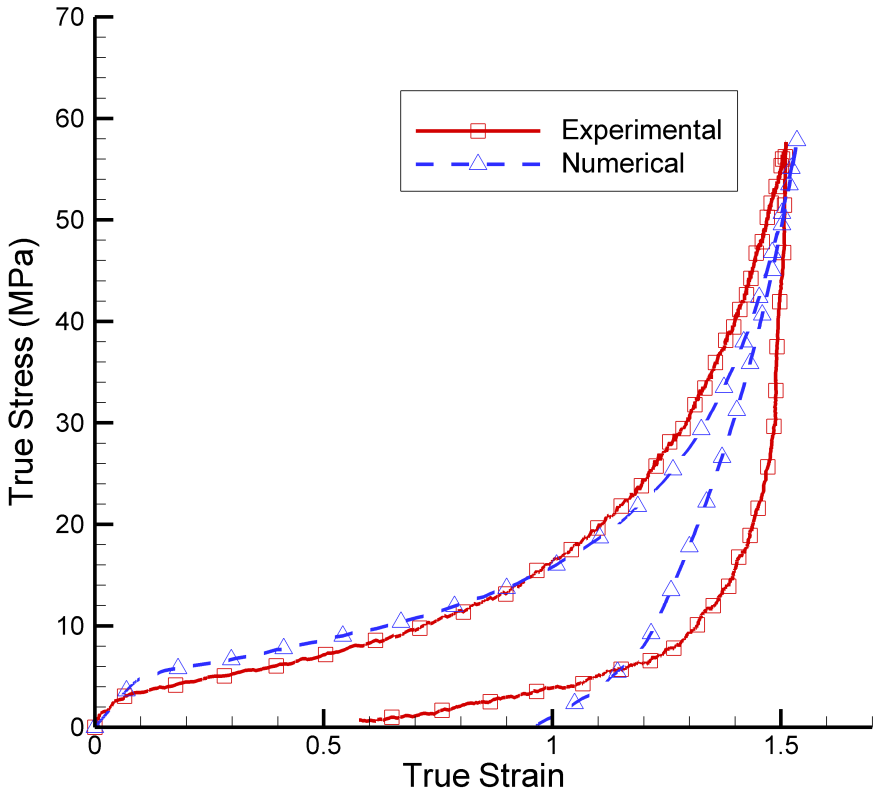

Figure 3.22: Experimental and Numerical Substrate Model Comparison of Polyurethane at 0.005/s

3.3.4 Description of the DCZM model

The DCZM model is comprised of eight-node user elements, with four nodes residing on either fracture surface. These nodes generate binding forces with their corresponding pair on the opposite fracture surface, while the fracture energy and binding forces are computed using the current surface area calculated from the positions of the four nodes. The interpretation of the fracture toughness is with respect to the *current area* of the fracture surface, since the thickness of the fracture specimen is not constrained to remain constant. Other details of the DCZM model, which includes finite rotations, are described in *Xie et al.* (2006).

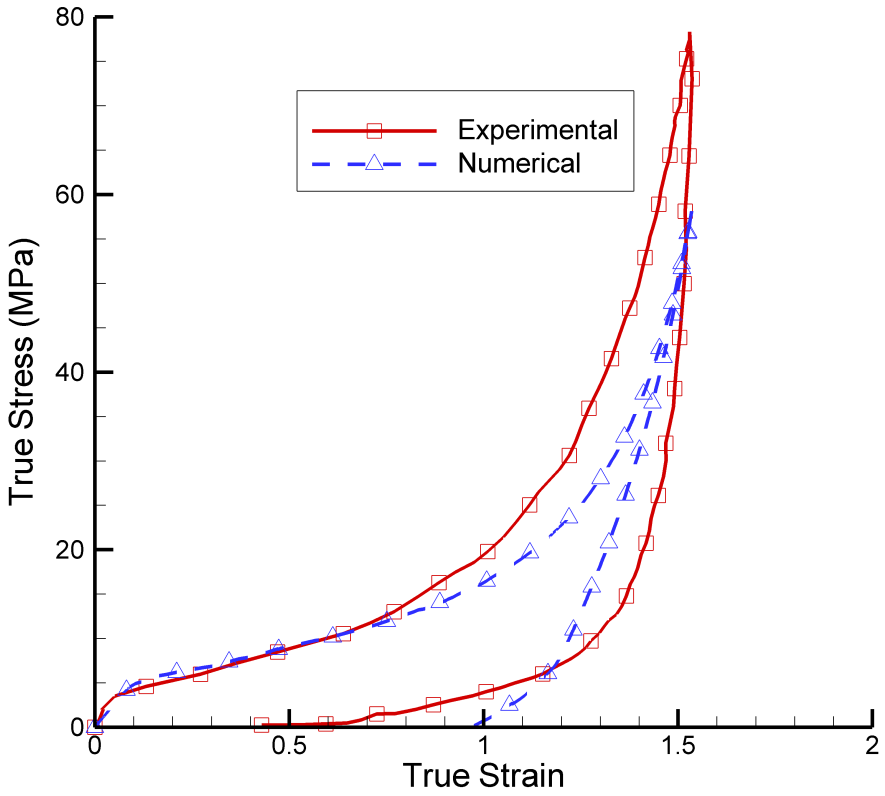

Figure 3.23: Experimental and Numerical Substrate Model Comparison of Polyurethane at 0.1/s

A modified trapezoidal traction separation law is used for the elements. The modified traction separation law is based upon the trapezoidal traction separation law for ductile materials, *Sun et al.* (2008), as shown in figure 21. The traction separation law is modified by adding an additional shallower relaxation stage. This additional relaxation stage was deemed necessary for the numerical model to converge while allowing for large deformations in the fracture process. The modified traction separation law is shown in figure 3.24, with the proportion of the fracture toughness allocated to each stage as indicated in the figure, as well as the stress turning points. Note that the fracture toughnesses of both traction separation laws shown are the same.

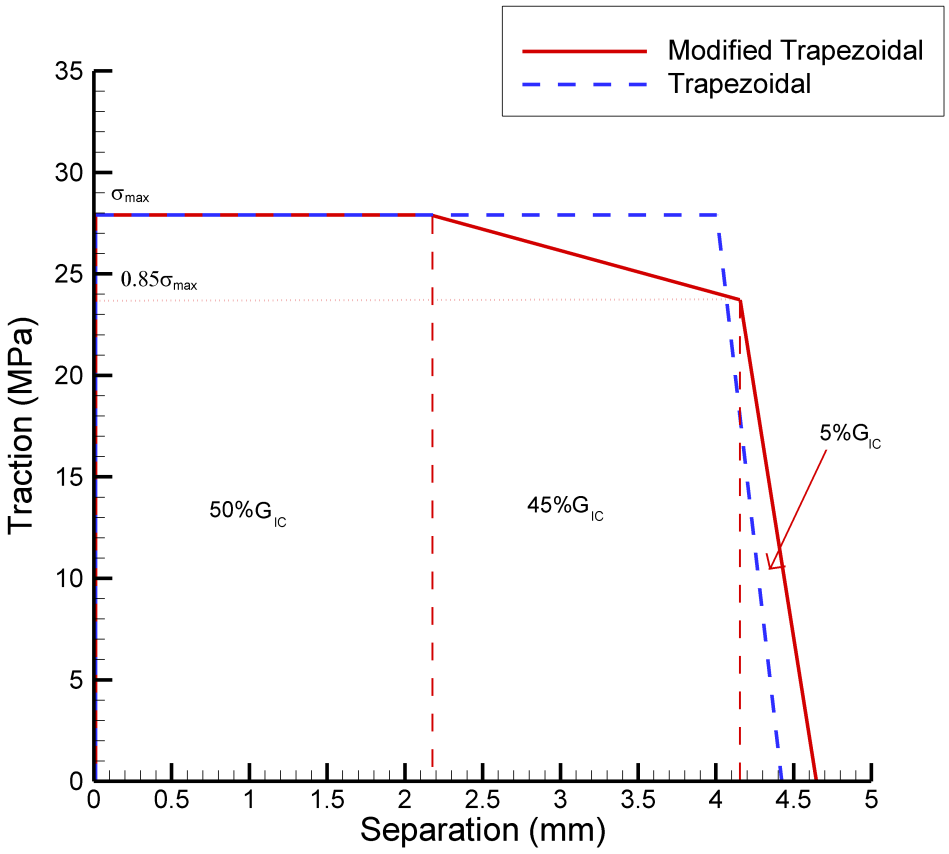

Figure 3.24: Traction Separation Laws used in the simulations

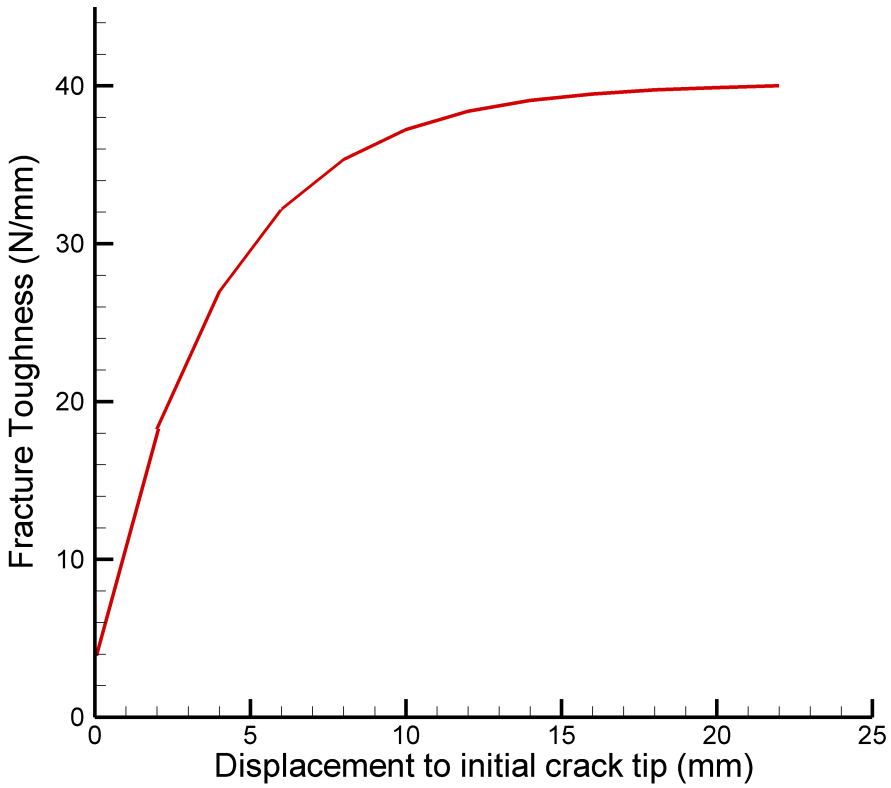

Figure 3.25: Fracture Toughness with respect to displacement

An R-curve *Gdoutos* (1990) is applied to the fracture toughness used by each element as follows;

$$G_{1c}(\delta) \;=\; G_{1c}^{SS} * \left(1 - \omega * e^{-\frac{\delta}{\gamma}}\right) \tag{3.25}$$

where δ is the distance of the element to the initial fracture surface, ω is the R-curve growth proportion and γ is the R-curve decay rate. An example of the shape of a R-curve is included in figure 3.25.

From the fracture stress calibration that was discussed earlier, a R-curve for the fracture strength is obtained as,

$$\sigma_{max}(\delta) \;=\; \sigma_{max}^{SS} * \left(1 - \omega * e^{-\frac{\delta}{\gamma}}\right) \tag{3.26}$$

Each DCZM element has the following assumed prescribed properties;

Maximum Steady State Stress	σ_{max}^{SS}
Stead State Fracture Toughness	G_{1c}^{SS}
R-curve growth proportion	ω
R-curve decay rate	γ
Various Shape Factors	G_{1c}^{i}, σ_{max}^{i}, i=1...4

Table 3.3: DCZM properties

3.3.5 Description of the numerical model

The numerical model for the PU/PAA experiment is composed of 12,060 nodes organized in 4,160 eight node plane-stress elements. The specimen is modeled using optically captured dimensions of the film. The left and right boundaries are fixed in the 2 and 3 directions. The right boundary is displaced only in the 1 direction at a rate of 7.5mm over 2500 seconds to match the experimental displacement rate. The 3 dimensional numerical model is included in figure 3.26. The process is repeated for the PU experiment, resulting in 8,200 nodes organized in 3,600 eight node elements. The displacement rates are similar to the PU/PAA experiment. During the solution process, the reaction force and displacement of the right boundary is output to a text file. In addition, the numerical solver also gives out the nodal displacements of selected substrate and DCZM elements in order to calculate the relevant mechanical parameters to interpret the results.

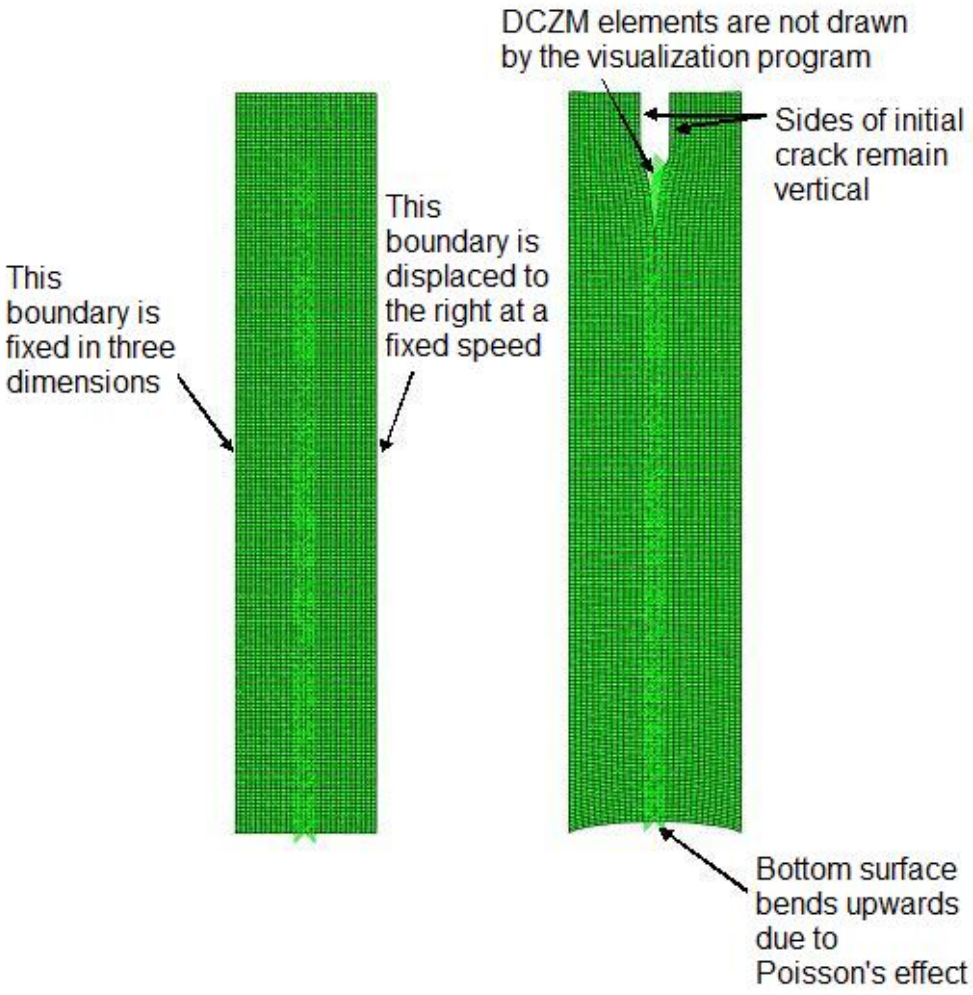

Figure 3.26: 3D Abaqus model of the fracture sample

The left and right boundaries are under full displacement control in three dimensions, the film is allowed to deform in the thickness direction. The DCZM elements are denoted by the crosses (x) in the right hand view.

3.3.6 Results of the numerical model predictions for PU/PAA and Pure Polyurethane

Iterating the DCZM elements for different R-curve variations and fracture toughnesses, a full match for the force-displacement curve is obtained and is shown in figure 3.27. The match is obtained at a critical fracture toughness of 65.4N/mm, and at a critical stress of 28MPa. In addition to the force-displacement curve, the crack point location of the experiment is also accurately matched. The crack point location is obtained in a similar fashion as in the experiment. The comparison is included in figure 3.10. The numerical prediction also show a close match for the initial slope of the strain-time plots at two locations on the substrate in figures 3.11 and 3.12. The initial slope of the numerical strain closely matches the experimental slope. The turning point of the numerical strain matches the turning point of the experiment.

In a similar manner, a full match for the force-displacement curve for pure polyurethane is obtained and shown in figure 3.28. The match is obtained at a critical fracture toughness of 61N/mm. It is noted that fracture toughness of pure polyurethane obtained in this manner maybe slightly overpredicted because the constitutive model that is used in the finite element predictions stores less plastic energy than required.

3.3.7 SEM In-Situ Experiments

Usually, the addition of nano-particles to a polymer material leads to a decrease in ductility and a corresponding decrease in fracture toughness. In the results reported here, the fracture toughness of stiffened polyurethane has been shown to be slightly larger than the non-stiffened polyurethane. Thus, it is worthy to examine the mechanisms responsible for elevating the fracture toughness. In order to do this, single-edge notch tension fracture tests are carried out *in-situ* in a Scanning Electron Microscope. These tests allow observation of the micron-scale and high nano-scale fracture mechanisms present in the composite and unstiffened polymer.

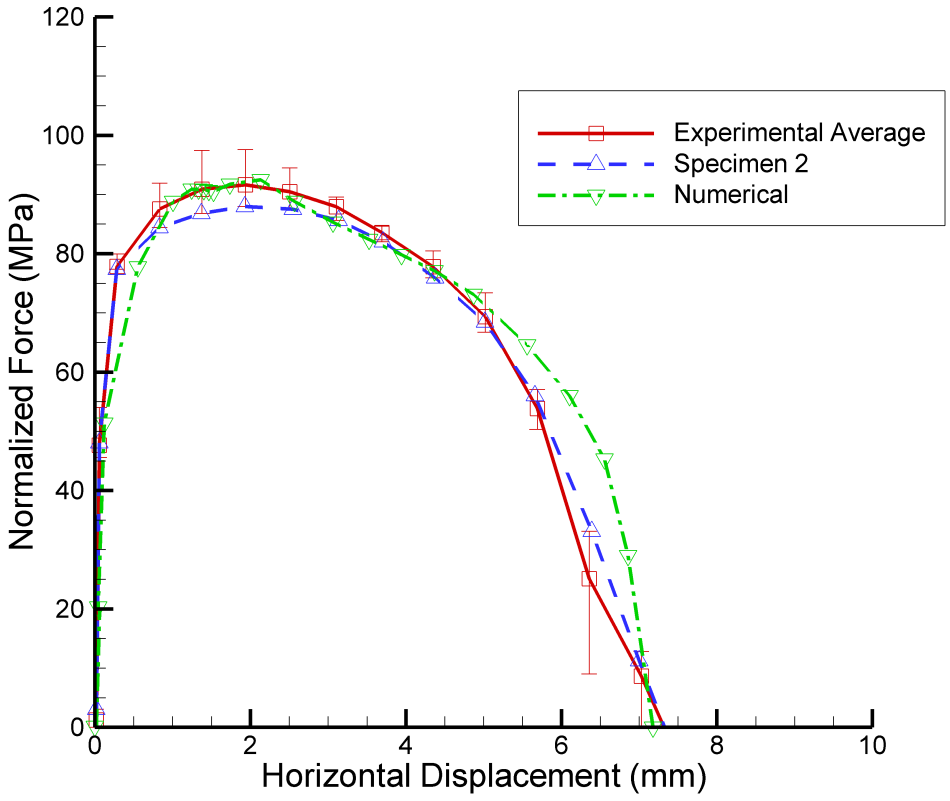

Figure 3.27: Comparison of Experimental and Numerical Force-Displacement Curves for 5 film PU/PAA stack

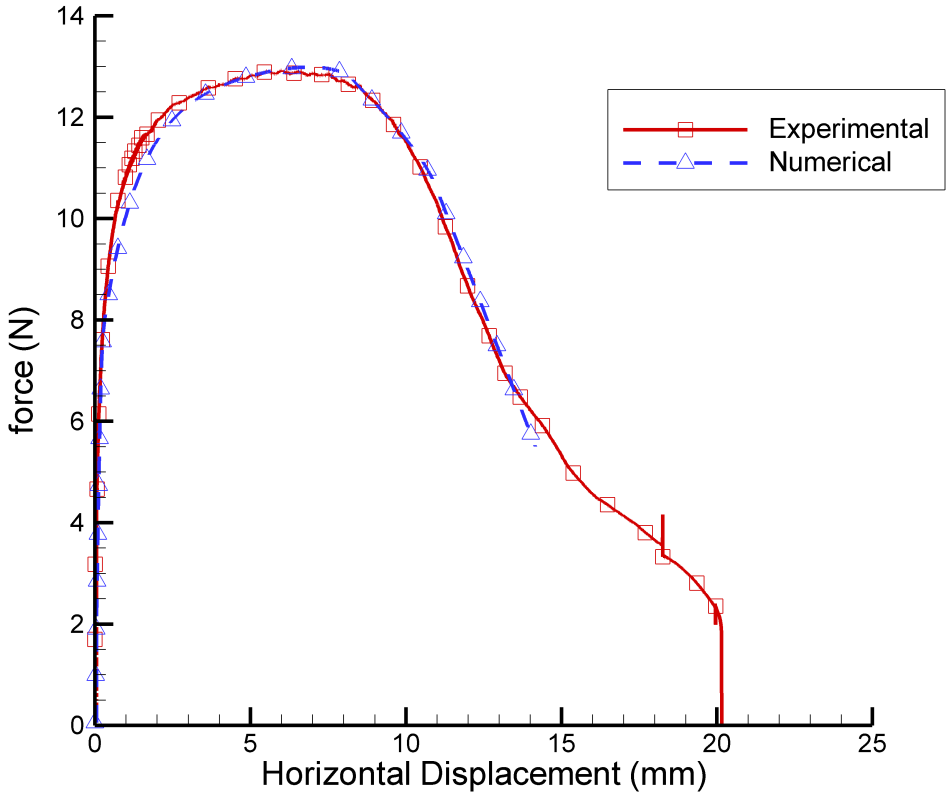

Figure 3.28: Comparison of Experimental and Numerical Force-Displacement Curves for pure polyurethane

It is observed that the layering of the nanocomposite results in large amounts of inter-layer shearing, similar to the delamination toughening reported in layered systems like Aluminum-Lithium as reported in *Rao and Ritchie* (1990). The inter-layer shearing results in the expenditure of a larger amount of energy during the fracture process. Additional energy is expended when micron sized voids grow when engulfed by the elevated stress process zone around the advancing crack.

3.4 Concluding Remarks

The fracture toughness of exponential LBL manufactured PU/PAA films has been measured though a combination of experiment and finite element based simulation. Due to the large deformations associated with the fracture event, an accurate constitutive model, validated through experiments, has been used in conjunction with a new finite deformation based formulation of the discrete cohesive zone model to extract the fracture toughness. Experimental results for full-field time histories of the strain maps in the fracturing film have been analyzed to obtain the R-curve parameters for the five stack film. This R-curve behavior implies the presence of toughening mechanisms at work in the fracture process zone. The experimental and numerical results presented in the paper show good agreement for the PU/PAA films as well as for similar fracture tests with pure polyurethane films. For the PU/PAA films, the mode I fracture toughness was found to be 65 N/mm, while for the pure PU this value was 61 N/mm. It should be noted that stiffened composites generally have lower fracture toughnesses with respect to their unstiffened base materials. In view of the enhanced stiffness and strength of the PU/PAA *Podsiadlo et al.* (2009), the LBL manufacturing process has resulted in a material with elevated stiffness and strength, while also elevating the fracture toughness.

CHAPTER IV

FRACTURE MECHANISMS OF PU/PAA IN-SITU, USING A NOVEL TEST FACILITY WITHIN A SCANNING ELECTRON MICROSCOPE(SEM)

In this chapter, Fracture mechanisms observed in the PU/PAA system as well as the PU/Clay system are described. These fracture tests were carried out SEM In-Situ, fracture mechanisms in the micron scale are observed and these observations are used to explain the measurements of fracture toughness in the previous chapter as well as the fracture mechanisms observed in subsequent chapters.

4.1 Test Setup

A SEM in-situ testing frame was borrowed from the Ford Motor Company and adapted for use in the Low Vacuum Scanning Electron Microscope (LVSEM) at the Electron Microscopy and Analysis Laboratory (EMAL) in the University of Michigan. Adaptation was necessary because the stage was built for the SEM at the ford motor company only operates in high vacuum mode. In order to prevent a build up of electrons on the surface of the specimen inside a high vacuum SEM, a thin layer of

gold atoms has to be deposited on the surface of specimen, this thin layer of gold changes the fracture mechanisms observed in the polymer composite. The LVSEM at EMAL allows us to image unaltered polymer specimens because a small amount of water vapor is introduced into the SEM chamber which removes excess electrons from the viewing surface. A mounting plate as well as adapter electronic leads for the leads. Specimens were mounted to metal plates and a notch made with a surgical razor just prior to testing. The setup mounted in the SEM can be seen in figure 4.1.

The samples are attached to flat sample holders with a thin layer of epoxy and a single notch is made perpendicular to one of the edges. The free standing film between the sample holders is $4 \pm 0.3mm$ by $12.5 \pm 2mm$. The initial crack is cut to dimension of $1.0 \pm 0.5mm$, leaving an un-fractured height, h_0, of $11.5 \pm 0.5mm$. The fracture tests are carried out on a tensile stage on loan from the Ford motor company. The tensile stage has been adapted to operate inside the FEI Quanta SEM at the EMAL at the University of Michigan.

The displacement rate is set to 0.001mm/s. The SEM takes about a second to refresh the image at a resolution of 1024 by 943 pixels, an image is automatically captured every 10 seconds. The tensile stage records the displacement of the grips with a LVDT. The tensile stage also records tensile forces with a 1000N load cell, the load cell has a resolution of 0.1N.

4.2 Fracture Mechanisms of PU/PAA

In this section, the fracture mechanisms of PU/PAA are discussed. These fracture mechanisms result in a larger created surface than simply the height multiplied by the thickness of the specimen. New surfaces are created between the layers through layer separation. New surface is also created within the layers, off the main crack path, through the growth of voids near the main crack tip of that layer.

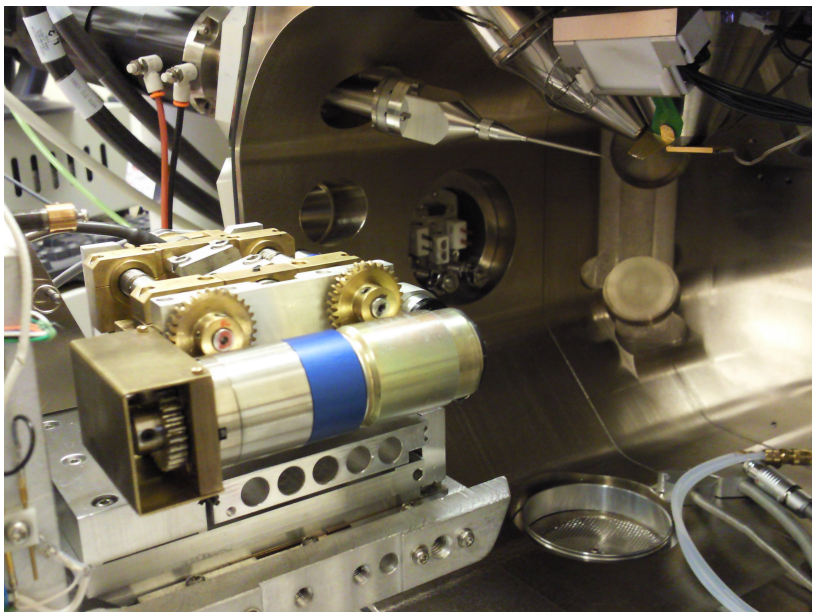

(a) Tensile Stage mounted to the SEM

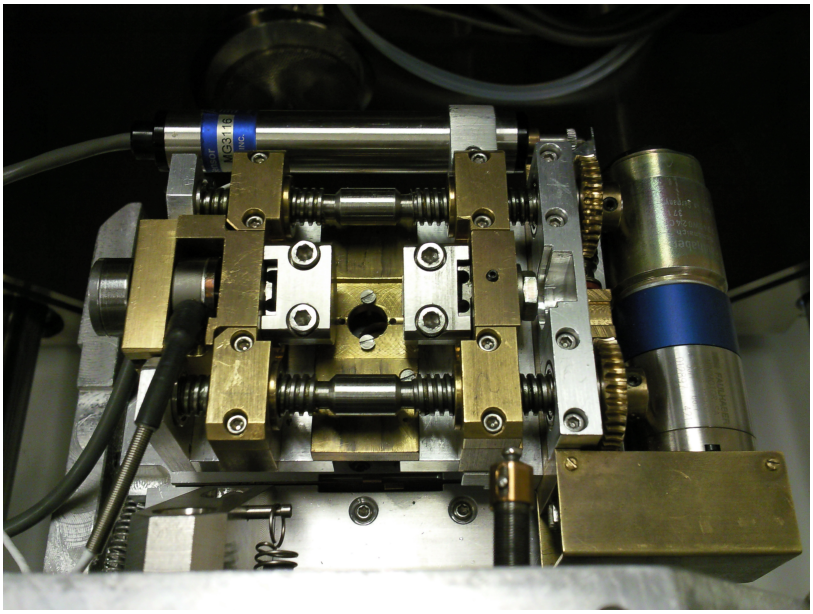

(b) Top View of Tensile Stage

Figure 4.1: SEM Experimental Setup

4.2.1 Layer Separation

Layer Separation is the growth of mode II fractures between the layers of a PU/PAA nanocomposite when a crack tip is being grown in mode I within the layers. Layer separation is enhanced by the mechanisms observed in the following subsections: Crack Tip Lag and Crack Tip Divergence. A schematic for Layer Separation is included in figure 4.2. Layer separation, caused by either crack tip lag or crack tip divergence, is directly observed in 4 out of 5 samples.

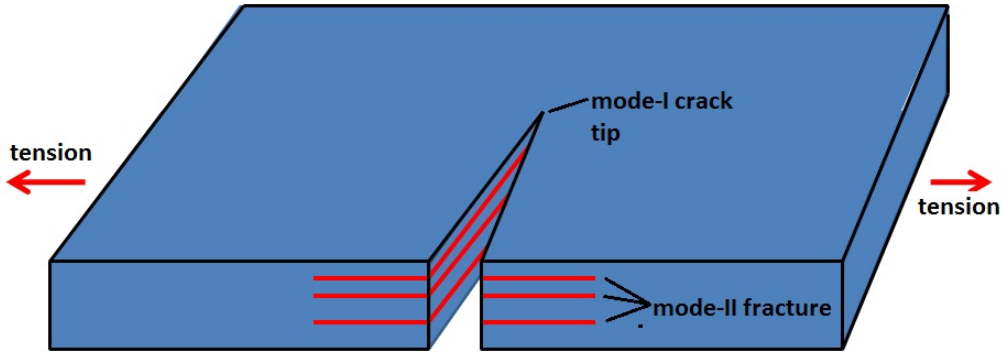

Figure 4.2: Layer Separation is the mode-II fracture between the layers of a LBL manufactured material when a mode-I crack is propagated normal to the thickness of the material.

4.2.2 Crack Tip Lag

Figure 4.3 shows the steady state crack growth of the crack tip, showing the crack tip of the bottom layer following the top layer by 0.1mm. After the specimen has been fractured, the fracture surface is imaged, showing clearly the separation of the initial cracked surface into multiple layers.

Figures 4.4 show the fracture surfaces of two separate samples, the camera's axis is perpendicular to the fracture surface. These pictures clearly show that the initial crack which is made with a surgical blade, starts as a single layer. When the crack initially grows, the single layer splits into multiple separate layers, but then recombines into a smaller number of layers in the steady state further along the crack path.

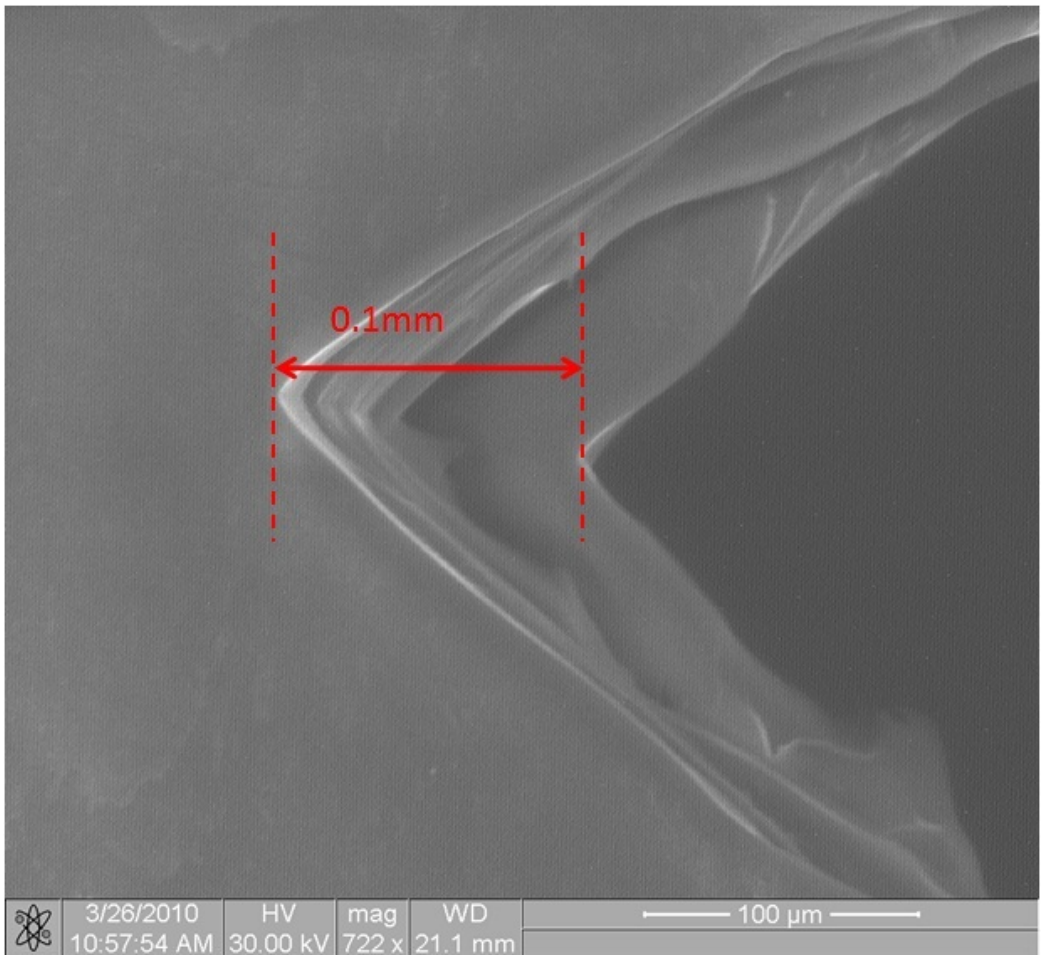

Figure 4.3: Crack Tip Lag of 100 microns

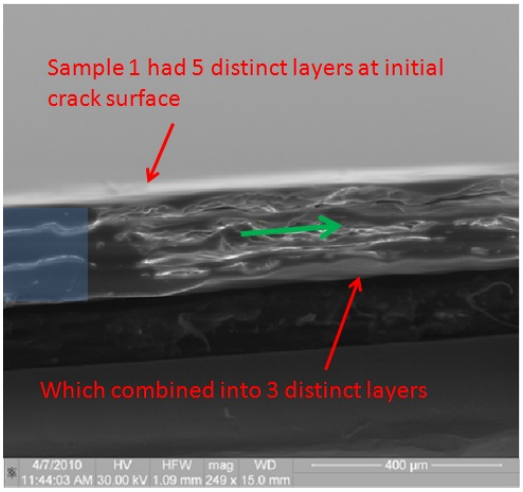

(a) Sample 1

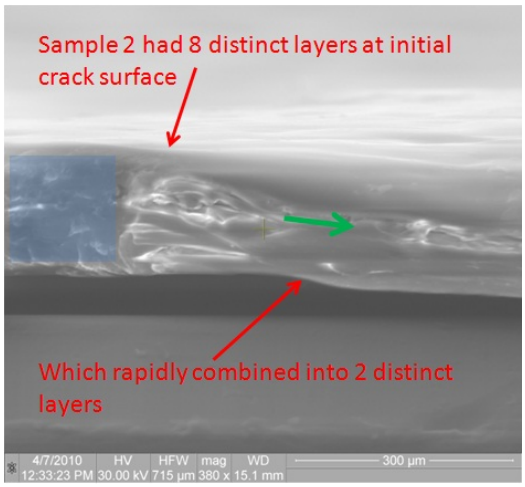

(b) Sample 2

Figure 4.4: Fracture Surface near Initial Notch for (a)Sample 1 and (b)Sample 2

4.2.3 Crack Tip Divergence

Crack path divergence is another mechanism for layer separation. The crack path has a stead state where the path of a lagging crack follows in the path of the leading crack. However, this steady state can be disrupted by the divergence of either the leading or lagging cracktip by large voids that grow slightly off the main crack path which merge with the crack tip on that layer only.

Figures 4.5 show the mechanism for crack path divergence. We observe in Figures 4.5a and 4.5b that a void, which exists only on the top layer, is growing slightly off the main crack path. This void eventually merges with the main crack on the top layer, this causes the left edge of the void to become the new crack tip, shown to be off the crack path of the other layers in Figure 4.5c.

Crack path divergence results in an even larger sheared region between two layers than between two layers which are affected by crack tip lag.

4.2.4 Void Growth

Another prominenent fracture toughening mechanism is void growth. PU/PAA has a lot of micron-sized voids, because of the LBL manufacturing process. These voids act as tiny cracks that grow when the stress concentration of the main crack tip approaches them. These cracks may or may not join the main fracture surface. If they do not lie on the main fracture surface, additional fracture surface has been created.

Figures 4.6a through 4.6c shows voids growing immediately in front of the crack tip, these voids grow exceptionally large as they are directly in the path of the crack and are located within 30 microns of a lagging crack tip. Figure 4.7 is a schematic of the void growth mechanism.

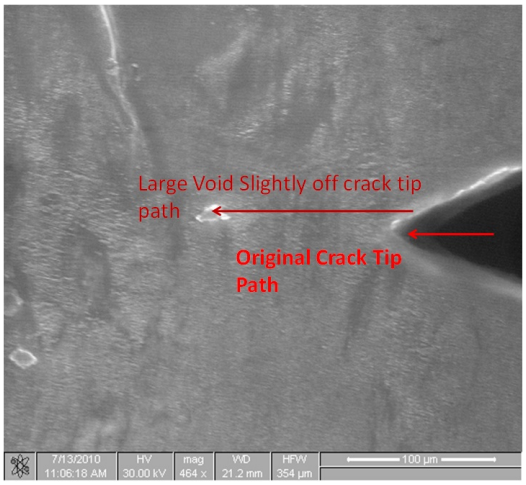

(a) large void slightly off the crack path on the top layer only

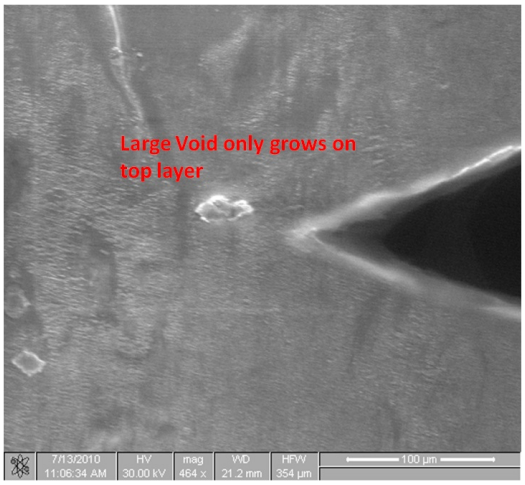

(b) large void grows

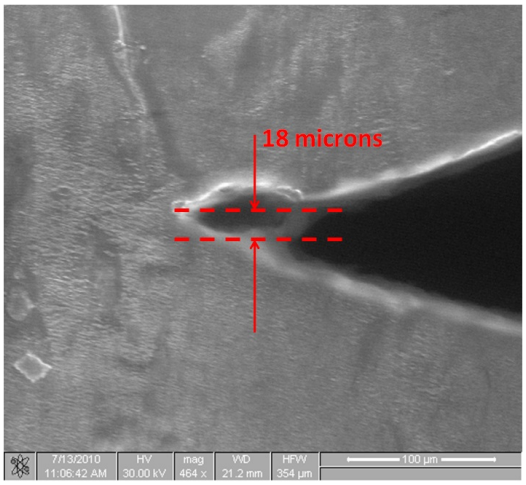

(c) large void merges with crack path, new crack tip is displaced only on top layer.

Figure 4.5: Crack Tip Divergence on the top layer of PU/PAA is the paths taken by the crack tips on two different layers differ. Large voids, which exist only on one layer, merge with the crack tip on that layer.

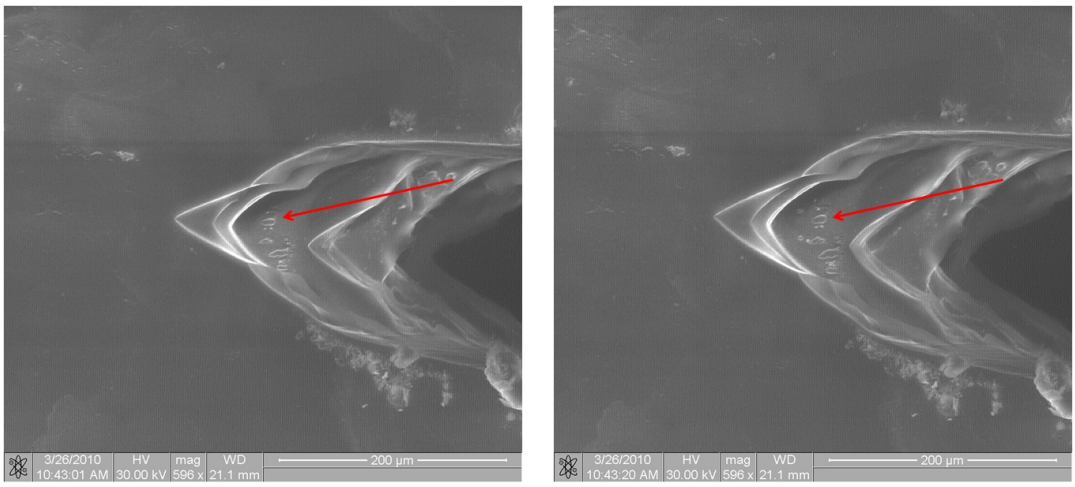

(a) t

(b) t + dt

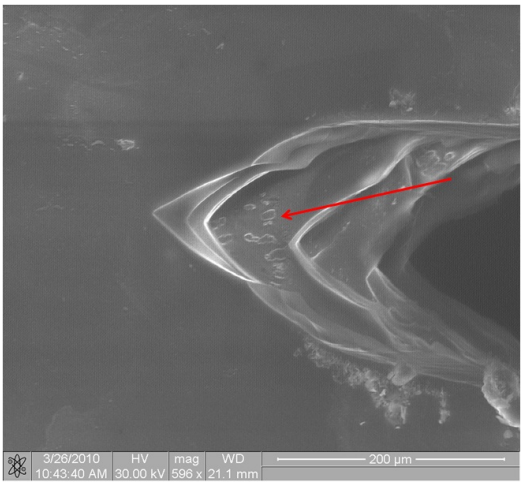

(c) t + 2dt

Figure 4.6: Progression of Void Growth

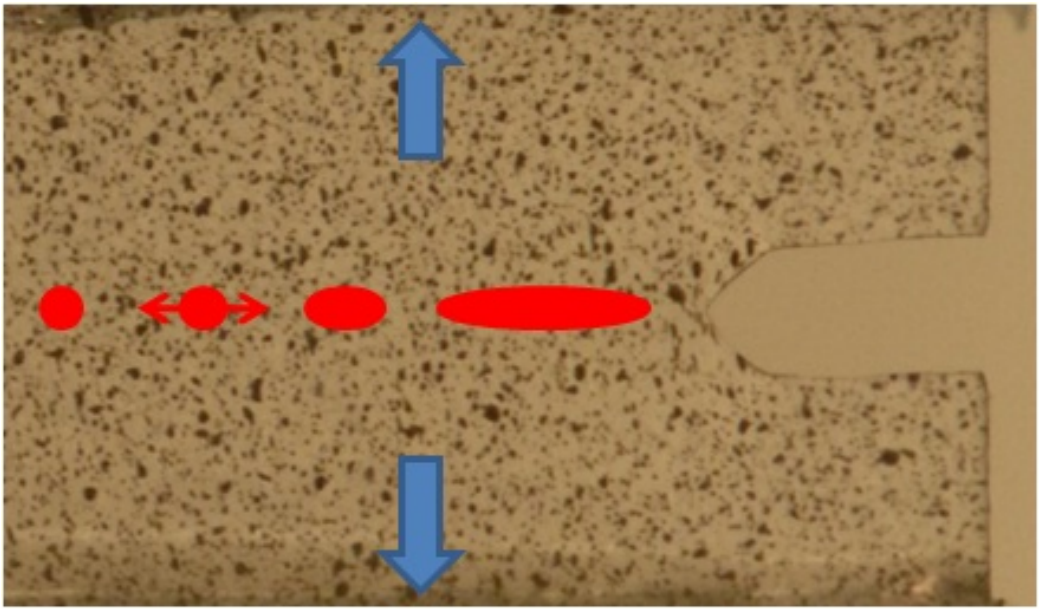

Figure 4.7: Schematic of Void Growth

Figures 4.8a through 4.8c show the sizes of voids at 2mm, 1mm and 0mm from the fracture surface. In the first two pictures, we can observe that the imperfections in the surface are roughly circular in shape and about 1 micron in size. However, at the crack tip, there are no imperfections which are circular and around 1 micron in size, the imperfections here are all elliptical and about 10 microns along the long axis. These pictures show that the voids nearest the crack tip path have grown from 1 micron to about 10 microns in length, the growth of these voids happens perpendicular to the deformation direction.

Figure 4.9 shows a representation of the voids 8mm, 4mm and 0.1mm in front of the crack tip, on the crack path at the same time step. As before, we observe that the circular 1 micron sized voids are only present far away from the crack tip. The voids near the crack tip are elliptical and have grown to about 10 microns in the longer axis. This figure shows that the voids within a certain distance of the crack tip grow. Void growth is observed on all PU/PAA samples.

These figures suggest that the crack tip strain concentrations seen in the companion paper and later in this paper, are caused by void growth.

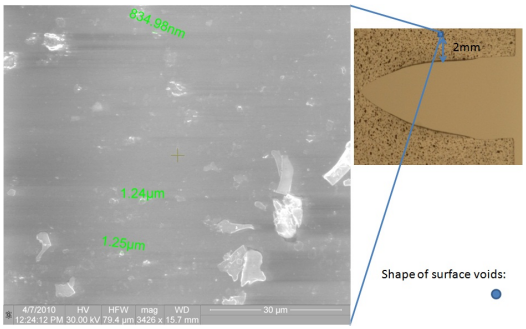

(a) Voids located 2mm from the fracture surface

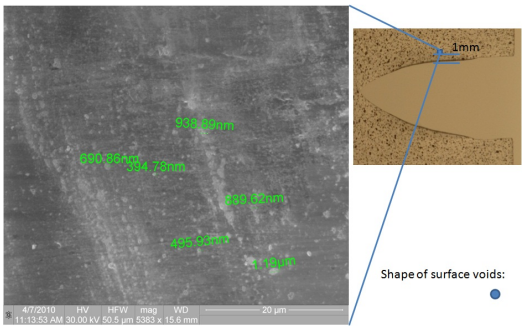

(b) Voids located 1mm from the fracture surface

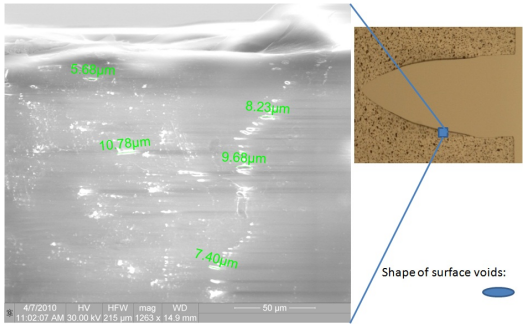

(c) Voids located near the fracture surface

Figure 4.8: Figures showing that Void Growth occurs near fracture tip

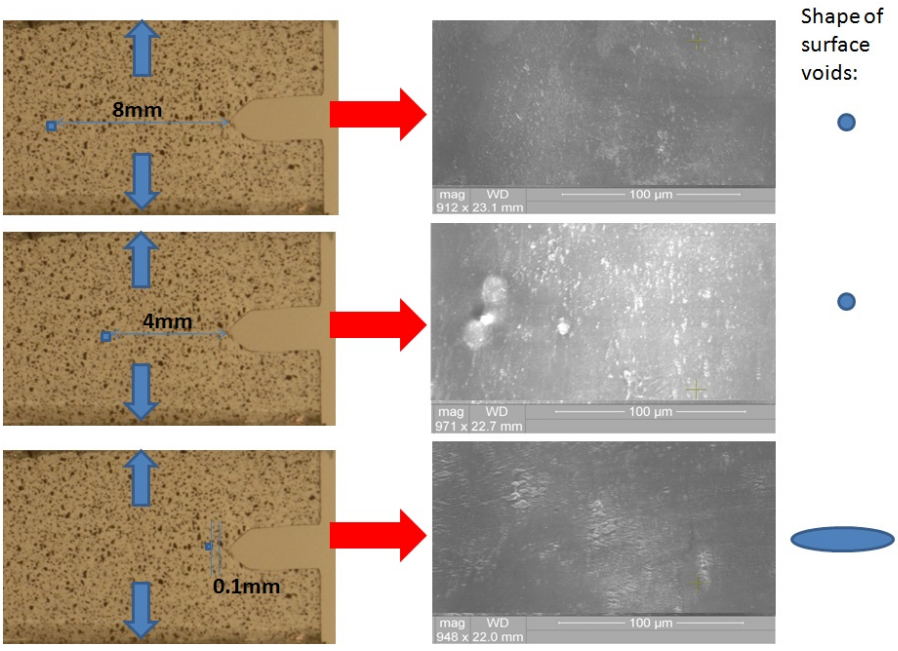

Figure 4.9: Void shape and size at differing distances from crack tip, along crack path

4.2.5 Critical Fracture Stress with respect to Fracture Mechanisms

It is shown in this section that the various fracture mechanisms are unique to the material close to the Crack tip path are an essential mechanisms prior to the development of the crack. These mechanisms are not observed in material away from the crack tip. Therefore, the critical stresses presented in section 3.2.7 can be more accurately described as the initiation of these fracture mechanisms as part of the fracture process.

Since it is the complex stress state close to the crack tip which initiates these fracture mechanisms, instead of an applied uniaxial stress, the macroscopic critical stress recorded in section 3.2.7 can be noticeably lower than that uniaxial ultimate tensile stress.

4.3 Fracture Mechanisms of PU/Clay

We are also able to observe that the voids are able to influence the path taken by the crack tip. Voiding is so active in the PU/Clay system, that the voids might grow through the thickness of the material and affect the path taken by the main crack tip. The crack tip in PU/Clay can be observed to displace from its intended path by as much as 100 microns at a time. This process results in the crack tip taking a winding path through the material, lengthening the crack path.

We observe large amounts of crack face bridging in the PU/Clay system; this is due to the large differential between the ductilities of the components. Ductile material is able to bridge the region between the two crack faces. These polymer bridges transfer load from one face to another. Slight crack face bridging can be observed in Figure 4.12. More pronounced crack face bridging is shown in figure 4.10.

Layer separation would occur at the layer with the weakest bonds. In the PU/Clay

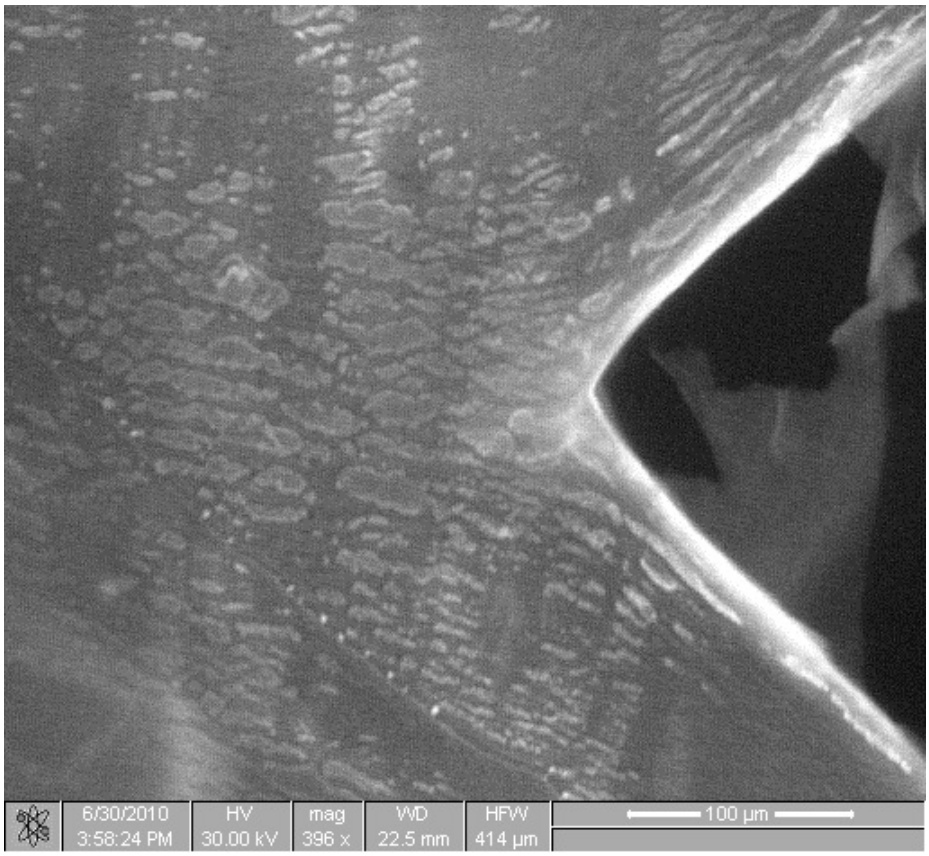

Figure 4.10: Crack Face Bridging occurs when thin bridges ductile material is pulled out of the crack faces and connecting the two faces of the crack.

system, the shearing occurs at the interface that has electrostatic bonds, and this is between the clay particles and the polymer. Spectrum analysis of the sheared surfaces in PU/Clay results in spectral maps in which there is contrast between the carbon rich (indicating polymer rich regions) map and the silicon rich (indicating clay rich regions) map as shown in figure 4.11. This indicates that one shear surface is composed of the polymer, while the other is composed of clay and the fracture plane is the layer of bonding between these two materials.

We are also able to observe that the voids are able to influence the path taken by the crack tip. Voiding is so active in the PU/Clay system, that the voids might grow through the thickness of the material and affect the path taken by the main crack tip. The crack tip in PU/Clay can be observed to displace from its intended path by

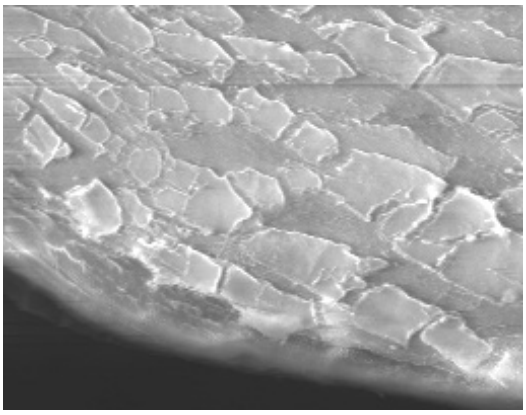

(a) SEM Image of Shear Surface close to voids (1)

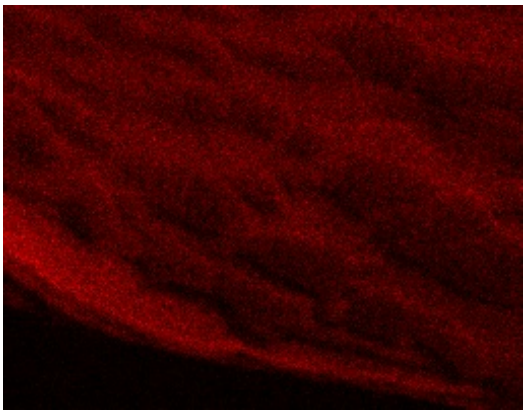

(b) Carbon Rich Regions (1)

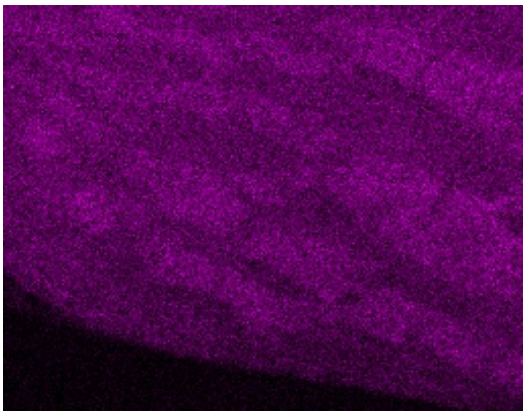

(c) Silicon Rich Regions (1)

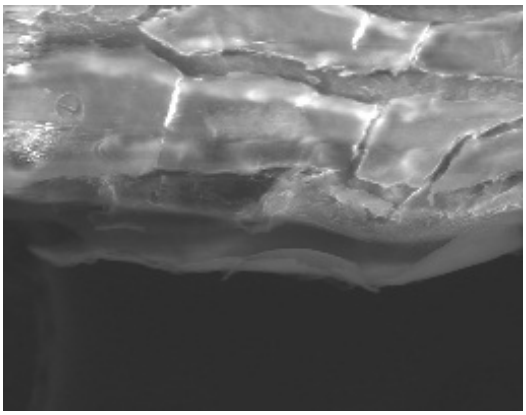

(d) SEM Image of Shear Surface close to Voids (2)

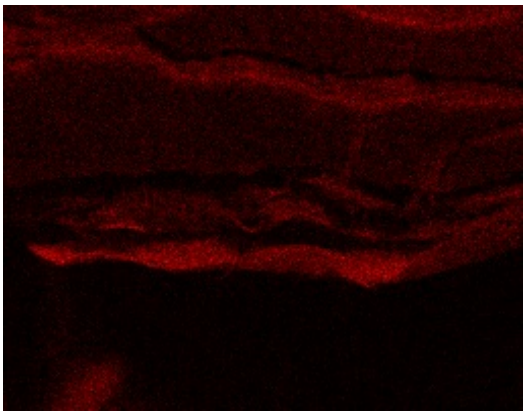

(e) Carbon Rich Regions (2)

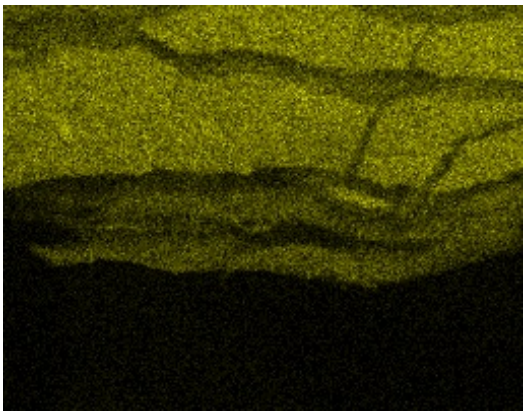

(f) Silicon Rich Regions (2)

Figure 4.11: Spectral Analysis of regions close to the voids, sheared regions expose layers rich in differing components in the nanocomposite

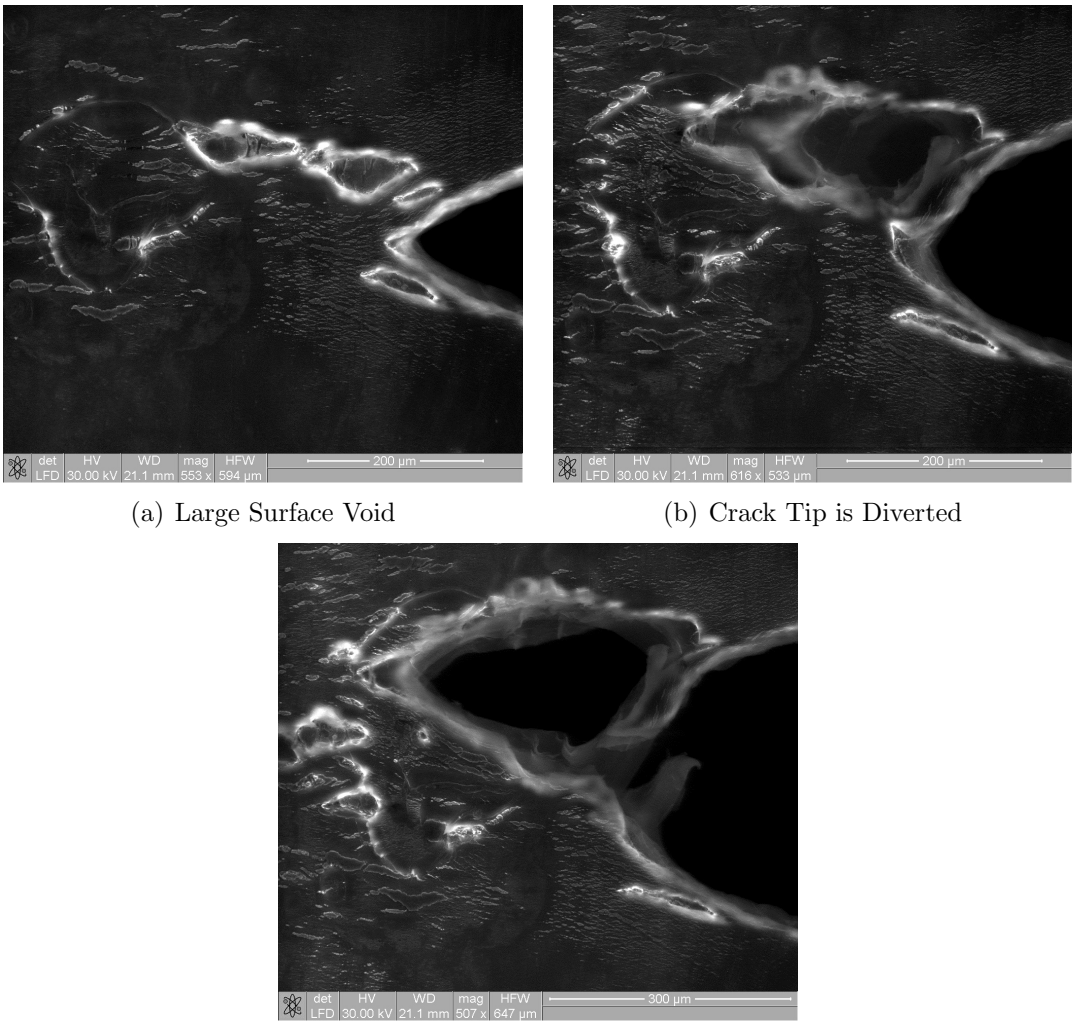

(a) Large Surface Void

(b) Crack Tip is Diverted

(c) Void has grown through thickness

Figure 4.12: Voids grow through the thickness of the material and influence the path taken by the crack.

as much as 100 microns at a time as shown in figure 4.12. This process results in the crack tip taking a winding path through the material, lengthening the crack path.

4.4 Fracture Mechanisms of Pure PU

Performing a similar test on a thin film of cast pure polyurethane, we observe none of the fracture mechanisms associated with LBL manufactured materials as described above. The single cast layer of polyurethane does demonstrate high ductility (but

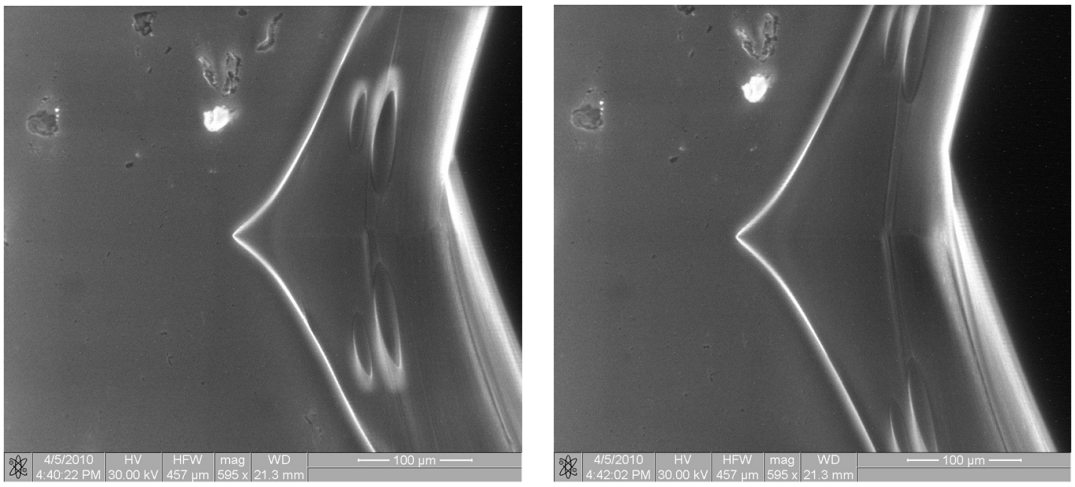

(a) Steady State Growth (b) Steady State Growth

Figure 4.13: Crack tip propagation in pure polyurethane has a constant steady state, showing huge amounts of ductility with a blunt crack tip that is sharper near the surface.

very little stiffness in comparison with the LBL nanocomposite) as expected from an elastomer, evidenced by its large crack tip angle. The crack tip also has a sharper crack tip at the surface due to the different stress state at the surface. The steady state propagation of a crack tip in pure polyurethane is shown in figure 4.13.

4.5 Concluding Remarks

This study demonstrates that LBL manufactured materials demonstrate a plethora of fracture toughening mechanisms which are not observed in other materials. Clearly, modeling these mechanisms to highlight the roles of nanoscale geometry and physical properties of the constituent materials is needed before an optimized nanocomposite with tunable stiffness and fracture toughness can be realized. The energy dissipating mechanisms reported in this letter, act together to increase the fracture toughness of the nanocomposite. These fracture mechanisms allow a stiffened nanocomposite to have similar or higher fracture toughness than the unstiffened polymer. The method of deposition and material composition induces microscopic mode II fracture normal

to the film, despite being loaded perpendicular to the normal of the film. It can be said that the film is susceptible to mode II fracture.

CHAPTER V

IMPACT TESTS ON GLASS/NANOCOMPOSITE/GLASS SAMPLES

In this chapter, the results from a series of impact tests on glass/nanocomposite/glass and glass/polymer/glass composite blocks are repeated. These tests were conducted to investigate the ability of the nanocomposite and polymer layers in protecting against an impact event.

5.1 Specimens

The nanocomposites described in this chapter are deposited by spray either manually or with the LDSM. They are deposited on either of the largest faces of 5"x5"x1.1mm borosillicate glass slides and bonded to glass blocks as described in chapter II.

The pure polymer composite blocks are formed by mixing polymer solution (100ml) with a small amount of spherical glass beads (0.5mg) as spacers and casting the solution between the 1.1mm thick glass slide and 1 inch thick glass block. The solution is dried in an oven at $82°C$

The PU/PAA Specimens available are all 21 microns thick, at 100 bilayers. The $(PU/PAA/(PU/Clay)_5)_{17}$ specimens are 7 microns thick. The $(PU/PAA/(PU/Clay)_5)_{42}$ specimens are 21 microns thick. PU specimens are prepared at 42 micron and 21 mi-

cron thicknesses. A schematic of the specimens with the dimensions indicated is shown in figure 5.1.

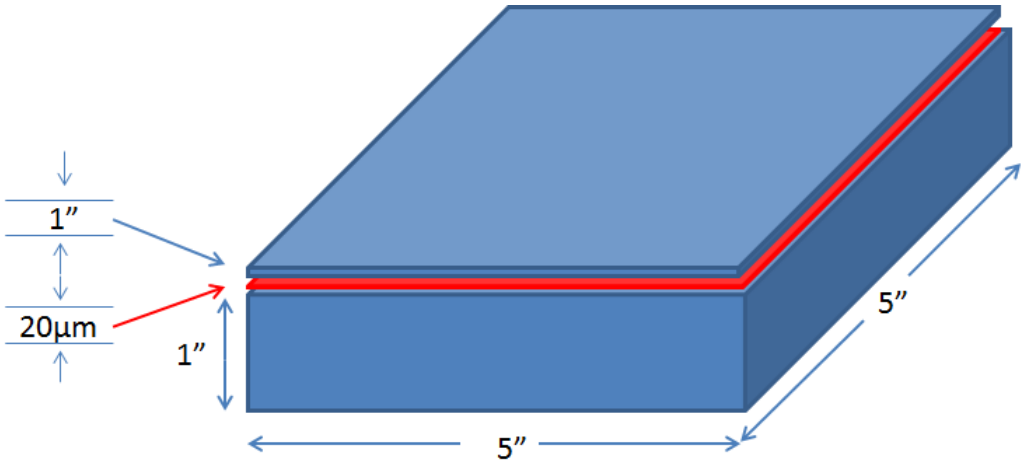

Figure 5.1: Composite Schematic

5.2 Methodology

A frame is built to hold the specimens' large flat surface normally to a 6' gas gun firing 0.5" spherical steel ball bearings. A trigger system is built to record the velocity and trigger a high speed camera system based on the recorded velocity. A schematic of the set up is shown in figure 5.2.

The trigger system consists of two IR emitters and two IR photodiodes, these are placed in emitter-diode pairs at two measured points along the expected trajectory of the ball bearing. When the ball bearing passes between the first pair of photodiode and emitter, a spike in voltage is recorded. The spike is recorded on an oscilloscope, and simultaneously starts a counter in a programmable I/O board. When the ball bearing passes through the second pair of photodiode and emitter, the voltage spike is recorded on an oscilloscope which allows to calculate the velocity of the ball bearing. The second voltage spike also records the counter value on the I/O board, when the counter reaches a predetermined multiple of the recorded counter value, a trigger

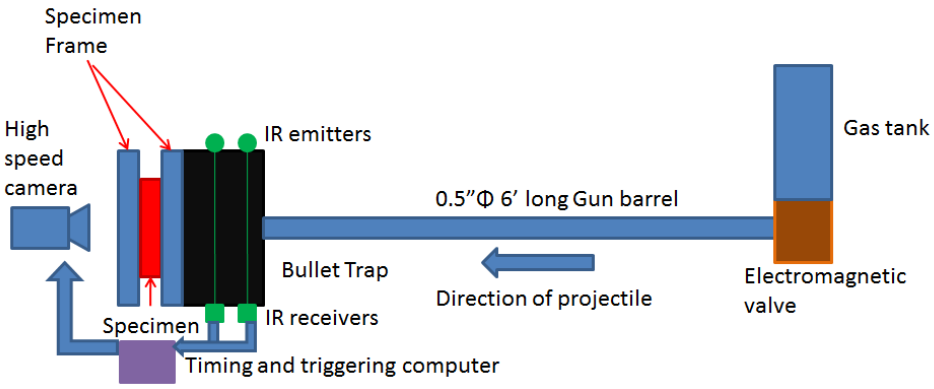

(a) Schematic of the End Notch Flexure Test

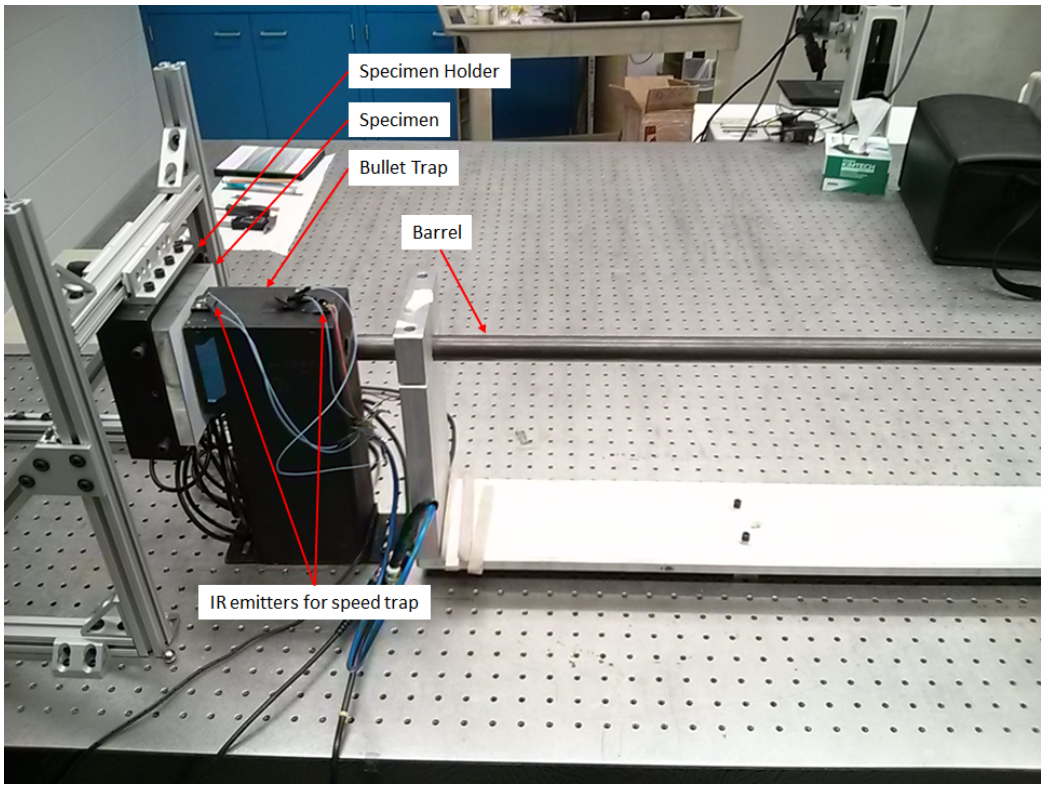

(b) End Notch Flexure Specimen

Figure 5.2: Impact Testing Schematic and Setup

signal is sent to the high speed cameras and flash system. This allows to record the impact event at high speed.

5.3 Results

In the following table, the highest velocity where the 1" glass block survives the impact event is listed along side the lowest velocity where the 1" glass block is fractured in the impact event for various composites. Survival is classified as no damage having been done to the glass block. For example, the unprotected 1" glass block, impacted at 9.3m/s, seen in figure 5.3 is said to have been damaged.

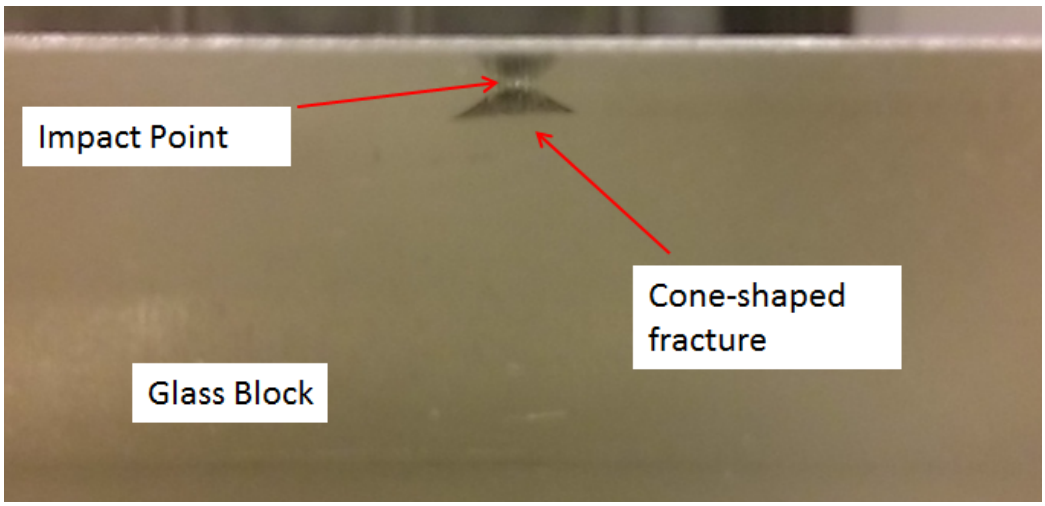

Figure 5.3: Damage to unprotected glass block at 9.3m/s

Given the low sampling of each particular series of tests, Fisher's Exact Test is employed to provide the probability that the null Hypothesis, H_0, that an impact velocity above the value $X_1\,(m/s)$ is not more likely to cause fracture is rejected, when it is false. The complementary positive hypothesis is then, H_1, that an impact velocity above the value $X_1\,(m/s)$ is more likely to cause fracture. The procedure in appendix A is followed to produce table 5.2.

Note that more samples would result in a higher certainty of rejection when the

Specimen Description	Highest Velocity Survived(m/s)	Lowest Velocity Damaged(m/s)
Pure Glass	8.41	9.3
PU/PAA(Handmade) (21 micron)	26.0	32.0
PU/PAA(Machine Made) (21 micron)	25.8	25.9
$(PU/PAA/(PU/Clay)_5)_{17}(7micron)$	29.3	31.5
$(PU/PAA/(PU/Clay)_5)_{42}(21micron)$	30.5	33.0
Pure PU (21 micron)	23.2	26.9
Pure PU (42 micron)	27.7	31.5

Table 5.1: Impact Velocities for Glass Composite Blocks

Specimen Description	Average Velocity $X_1\,(m/s)$	Number of specimens	Power
Pure Glass	8.88	5	0.9
PU/PAA(Handmade) (21 micron)	29.0	4	0.75
PU/PAA(Machine Made) (21 micron)	25.9	6	0.933
$(PU/PAA/(PU/Clay)_5)_{17}(7micron)$	30.5	4	0.833
$(PU/PAA/(PU/Clay)_5)_{42}(21micron)$	31.8	3	0.67
Pure PU (21 micron)	25.0	3	0.67
Pure PU (42 micron)	29.4	5	0.9

Table 5.2: Probability that Fracture is likely caused by Velocity above $X_1\,(m/s)$

hypothesis is false. The sample sets with the highest number of samples available have the highest power value - specifically the machine made PU/PAA.

5.3.1 General Impact Velocity Observations

It is noted that in all cases, adding a layer of polymer and 1.1mm of glass greatly improves the highest impact velocity survived by the 1" glass block. Comparing 21 micron polymer interface specimens, the $(PU/PAA/(PU/Clay)_5)_{42}$ specimens have the best performance at 30.5m/s.

5.3.2 Effect of Increased Thickness

Comparing the $(PU/PAA/(PU/Clay)_5)_{XX}$ specimens, it is observed that the additional thickness from 7 micron to 21 micron has a negligible effect on the impact

velocity survived and fractured. There is an increase from 29.3m/s to 30.5m/s, for an increase of 1.5m/s in highest velocity survived; as well as a corresponding increase from 31.5m/s to 33.0m/s, for an increase of 1.5m/s in lowest velocity fractured. This represents a 4.1% increase in velocity survived for a 200% increase in thickness.

The behavior of the layered $(PU/PAA/(PU/Clay)_5)_{XX}$ system is unlike that of the single cast layer of PU system, where an increased thickness of protecting polymer results in an increase in the impact velocity survived and fractured. There is an increase from 23.2m/s to 27.7m/s, for an increase of 4.5m/s in the highest velocity survived; as well as a corresponding increase from 26.9m/s to 31.5m/s, for an increase of 4.6m/s in the lowest velocity fractured. This represents a 19.4% increase in velocity survived for a 100% increase in thickness.

5.4 Observed Fracture Mechanisms

The 1" thick glass block produced a characteristic cone fracture under the impact point, regardless of whether it is protected by a top glass slide and polymer layer or not. This can been seen in figure 5.3. In addition, the cone shape of the fracture suggests that the boro-silicate glass is anomalous under indentation *Bertoldi and Sglavo* (2004). Typically, anomalous glasses are described by a elastic-plastic model where yield is dependent on the hydrostatic pressure *Lamdropoulos and Fang* (1996).

If the 1" glass block is protected by a polymer layer and 1.1mm glass slide, the 1.1mm glass slide under the impact point is crushed by the impact event. Fracture lines would occur in the glass slide that travel to the edge of the glass. This effect is observed in figure 5.4. These cracks in the 1.1mm glass slide allow the separate pieces of glass to individually shear away from the impact point, some shearing can be observed in figure 5.4 nearest the impact point.

Should the impact velocity on a composite block be high enough, the energy expended by the impactor in crushing the top glass slide and shearing the polymer

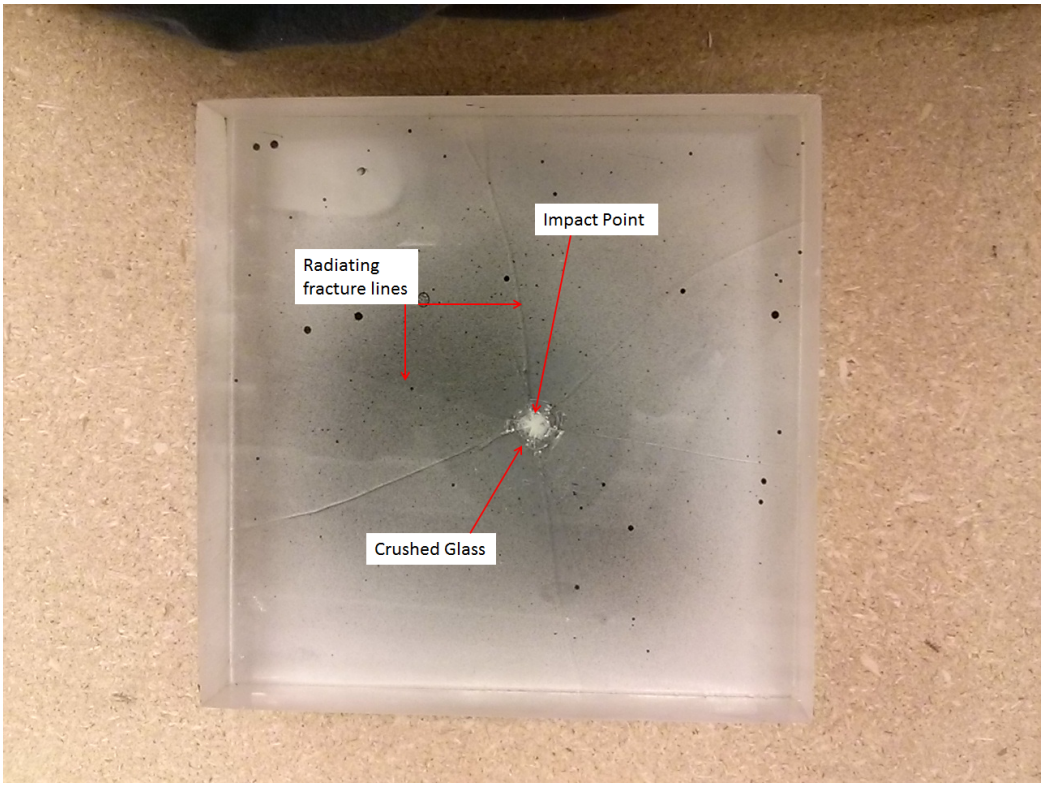

Figure 5.4: Cracks in the 1.1mm glass slide as observed through the 1' glass block

would not be high enough to distribute all of the impactor kinetic energy. Thus, this results in damage to the 1" thick glass block in the form of cone fractures as observed in unprotected glass blocks in figure 5.3. A damaged PU/PAA protected glass block, impacted at 25.9m/s, is shown in figure 5.5.

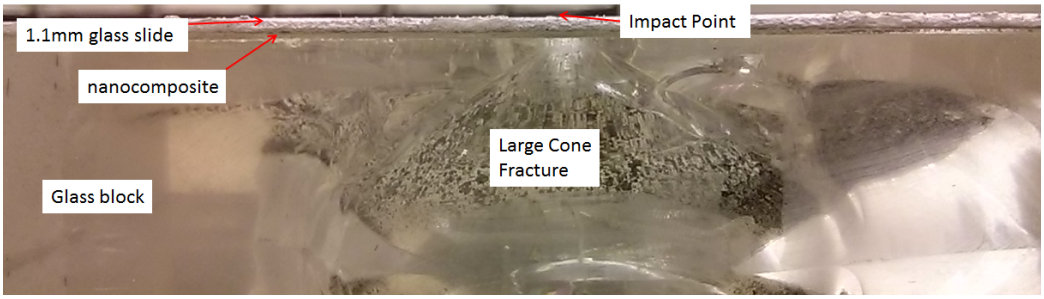

Figure 5.5: Composite Glass/PUPAA/Glass block impacted at 25.9m/s

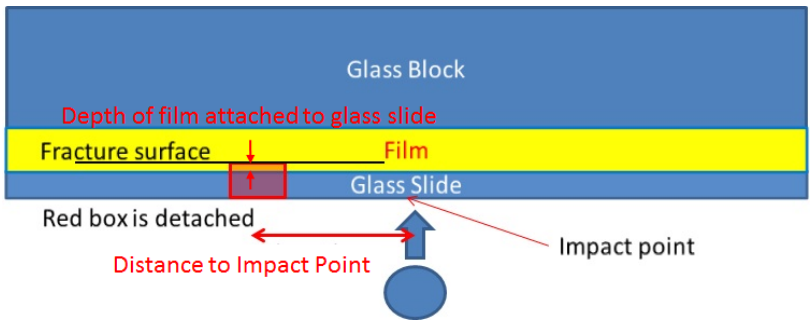

(a) Schematic of the shear location and method of mesurement

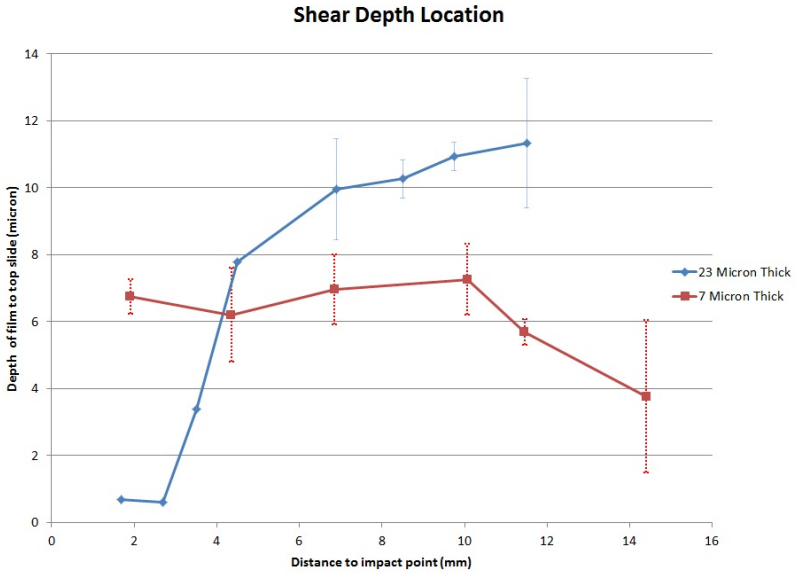

(b) Depth of shear surface from 1.1mm glass slide in $(PU/PAA/(PU/Clay)_5)_{XX}$ specimens

Figure 5.6: Shear Location

5.4.1 Measured conical fracture in the $(PU/PAA/(PU/Clay)_5)_{XX}$ layer

Pieces of 1.1mm glass slide with $(PU/PAA/(PU/Clay)_5)_{XX}$ nanocomposite still attached were removed from the surface of the $(PU/PAA/(PU/Clay)_5)_{XX}$ specimens post impact. The thickness of $(PU/PAA/(PU/Clay)_5)_{XX}$ still attached to the 1.1mm glass slide was then measured. This was performed only on the $(PU/PAA/(PU/Clay)_5)_{XX}$ because these were the only specimens where the shear surface detached large continuous pieces of glass. A schematic of the dimension measured is included in figure 5.6a.

Figure 5.6b shows the depth of the shear surface in the $(PU/PAA/(PU/Clay)_5)_{XX}$ nanocomposite. It is observed that the shear surface in the 21 micron specimen takes

the shape of a cone that begins at the glass slide surface and increases linearly from a depth of 1 micron to 9 microns , and plateaus at a depth of 10-12 microns. It is observed that the shear surface in the 7 micron specimens does not change greatly and has a value of 6-7 microns at all locations.

5.4.2 Shear Damage in the 7 micron specimens

However, much more extensive damage is observed in the 7 micron specimen, where an additional shear surface is present in the nanocomposite, such that some film can be seen partially detached. Shear damage also occurs in the 21 micron specimen, but only at the locations less than 3mm from the impact point. Figure 5.7 shows the damaged and detached film above the thickness of the film in the 7 micron sample. Figure 5.8 shows the film still attached to the glass slide in the 21 micron sample.

The measured depth indicates that the preferred shear fracture location for nanocomposite specimens is 10-12 microns deep from the 1.1mm glass slide. If it is not possible to fracture in that manner, multiple shear surfaces are produced and a similar amount of energy is absorbed, resulting in the negligible difference in the impact velocity results between the 7 and 21 micron specimens. A schematic of the preferred shear surface in the 21 micron samples is included as figure 5.9.

5.5 Conclusions

It is concluded that the LBL nanocomposite does perform better than a monolayer polymer of the same thickness at the thicknesses tested. However, It is observed that adding thickness to a layered nanocomposite system, that tends to shear, does not result in additional ability to withstand impact. It can be expected that at much higher thicknesses, the monolayer polymer would perform better than the LBL nanocomposite. The preferred shear location has been measured and it is found that

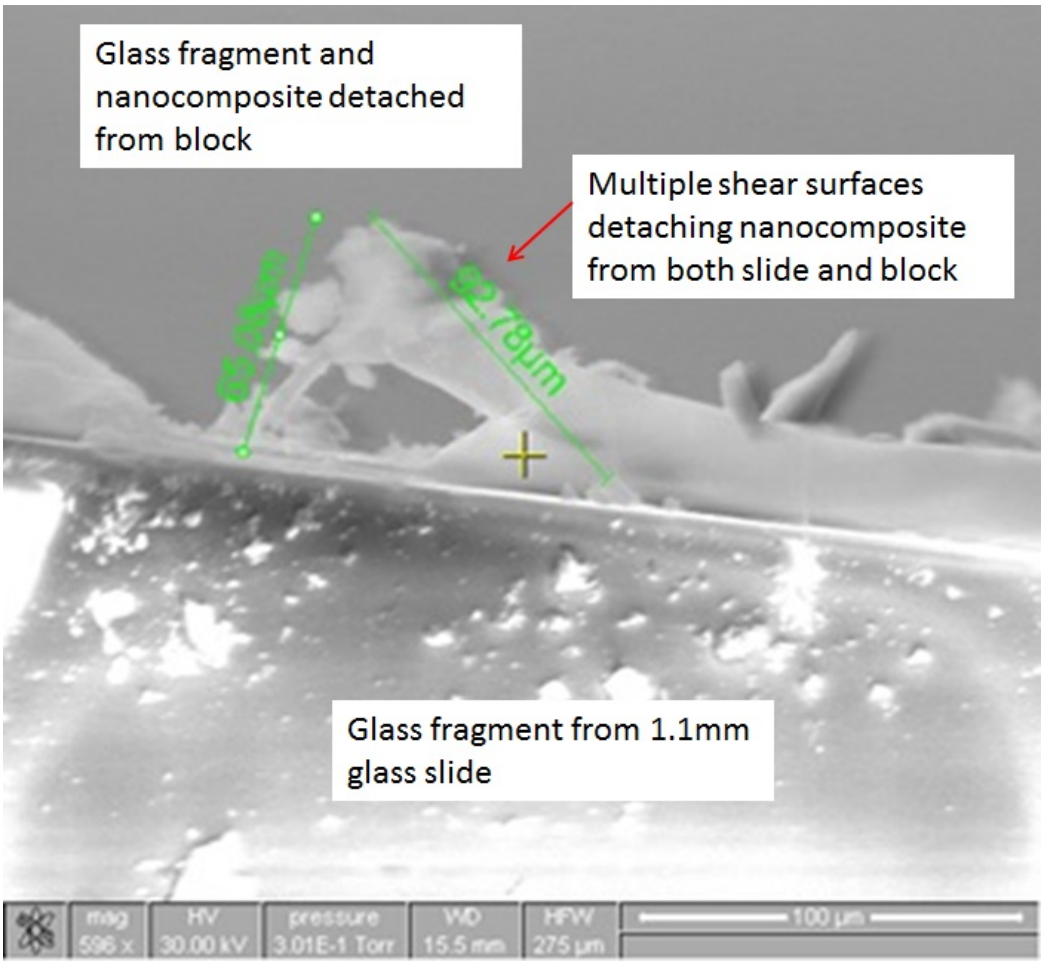

Figure 5.7: Shear damage in the 7 micron $(PU/PAA/(PU/Clay)_5)_{XX}$ seen in an edge-on view of the film

if the nanocomposite is allowed to shear in its preferred depth of 10-12 microns, we can conclude that the shearing action prevents further stresses from being transmitted to layers below the sheared layer. If the nanocomposite is less than 10-12 microns, a similar amount of energy is absorbed through the development of multiple shear surfaces.

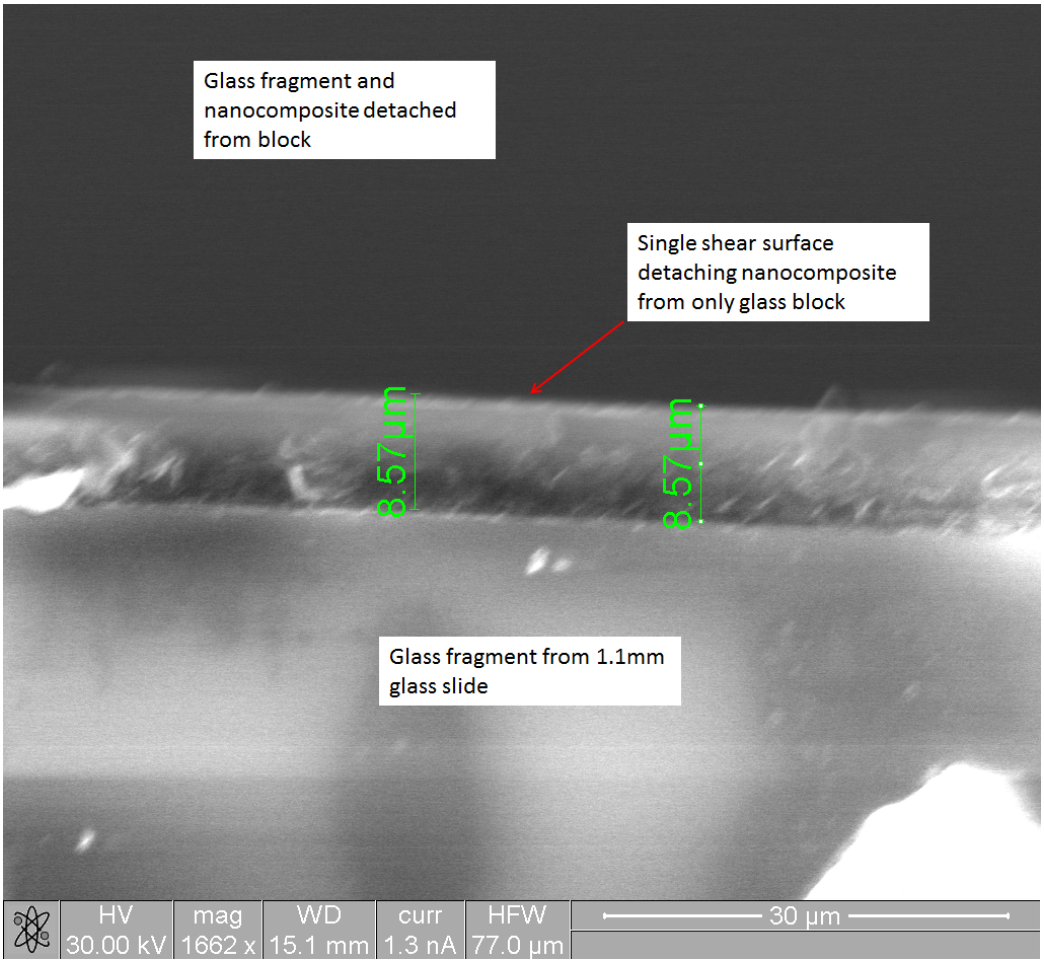

Figure 5.8: No Shear damage in the 21 micron $(PU/PAA/(PU/Clay)_5)_{XX}$ seen in an edge-on view of the film

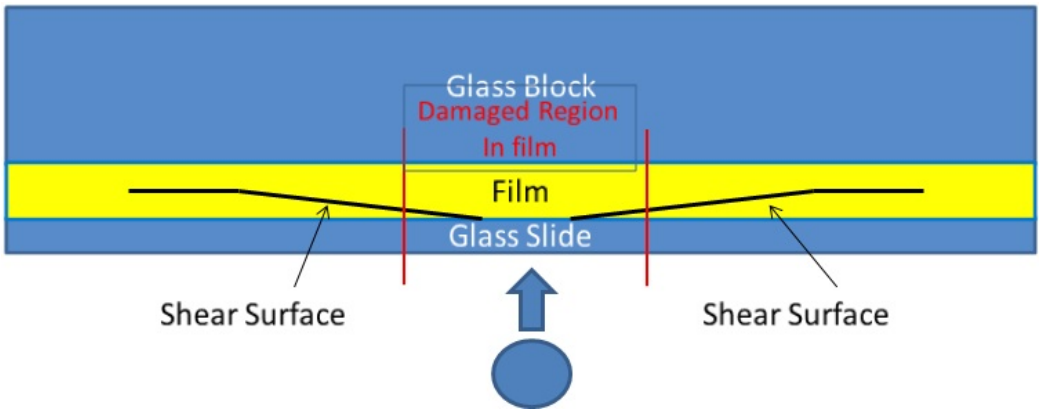

Figure 5.9: Preferred location of shear damage in 21 micron $(PU/PAA/(PU/Clay)_5)_{XX}$

CHAPTER VI

INTERLAMINAR FRACTURE CHARACTERIZATION OF PU/PAA

In this chapter, the interlaminar fracture toughnesses of PU/PAA are determined through a series of experiments. The LDSM is the manufacturing method for these samples.

6.1 Determining Interlaminar mode II Shear Strength

1" by 0.5" Lap Shear specimen is used to determine the interlaminar mode II shear strength. Glass slides cut to 1" by 0.5" are deposited with PU/PAA in the LDSM. After deposition, these are bonded to steel tabs using commercial 2-ton epoxy. Another 1" by 0.5" glass slide is bonded to a similar steel tab using commercial 2-ton epoxy. Once the epoxy hardens, the glass slide with PU/PAA is wet with a new layer of PU, rinsed and then bonded to the plain glass slide. A schematic of the test sample is seen in Figure 6.1. The specimen is loaded in tension by an Instron test frame at 1mm/min, pictures are taken every 5 seconds.

A critical shear strength of $1.186 \pm .005$ MPa is obtained from three samples in figure 6.2

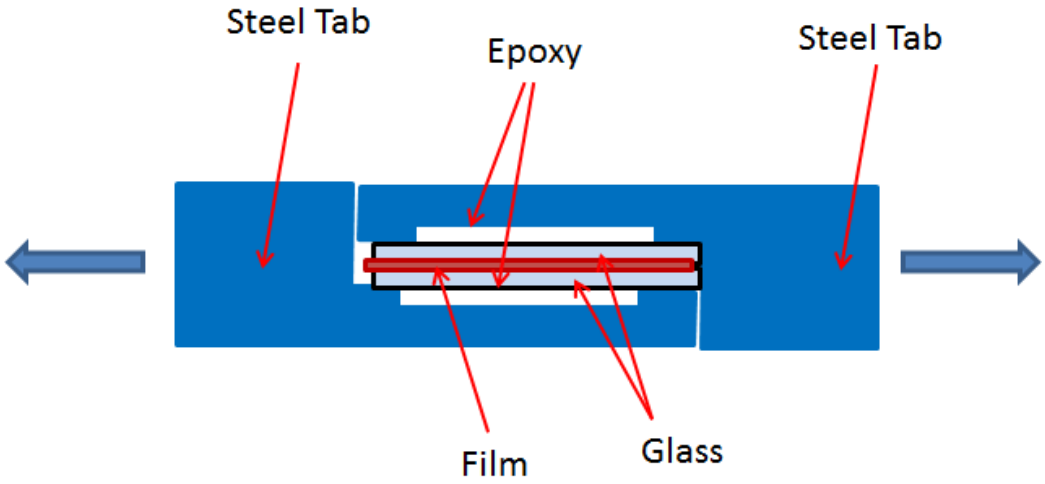

Figure 6.1: Lap Shear Specimen

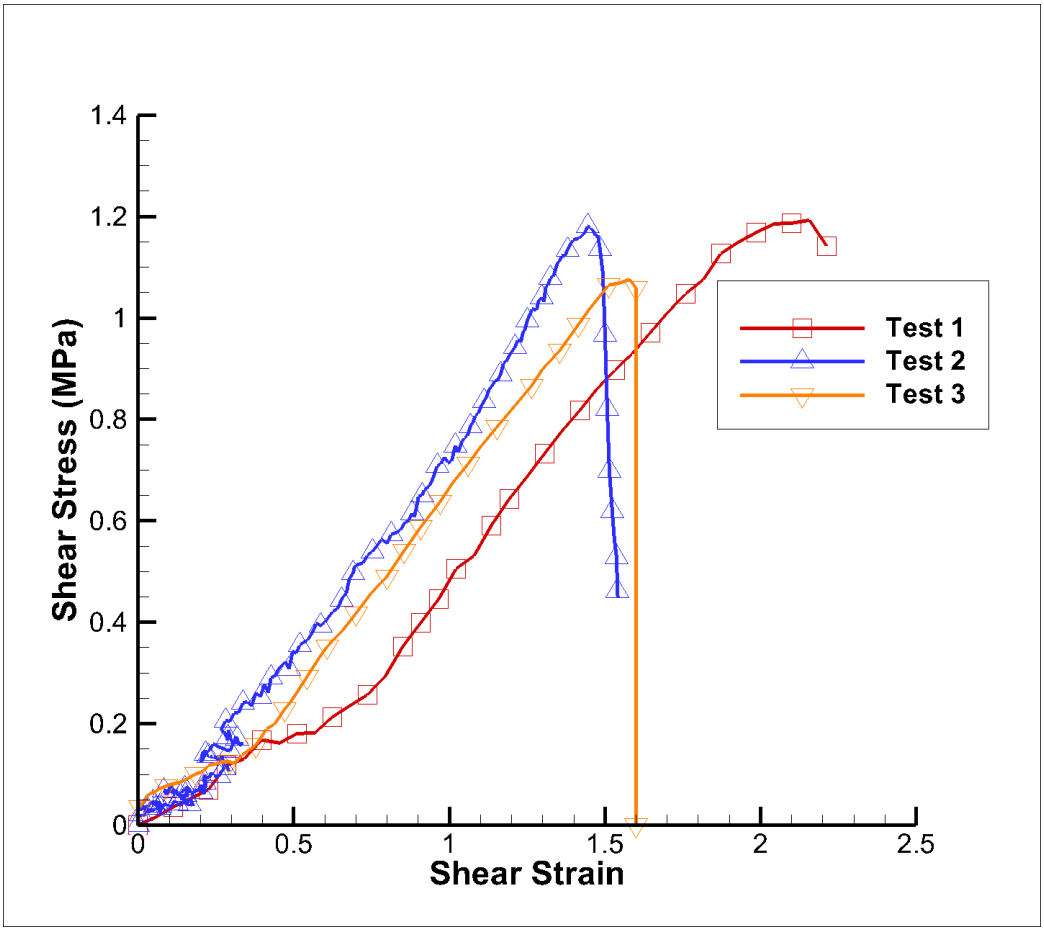

Figure 6.2: Lap Shear Results

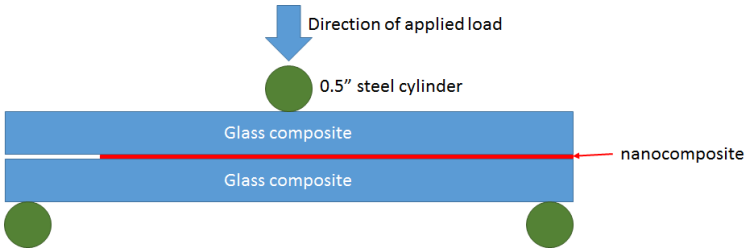

(a) Schematic of the End Notch Flexure Test

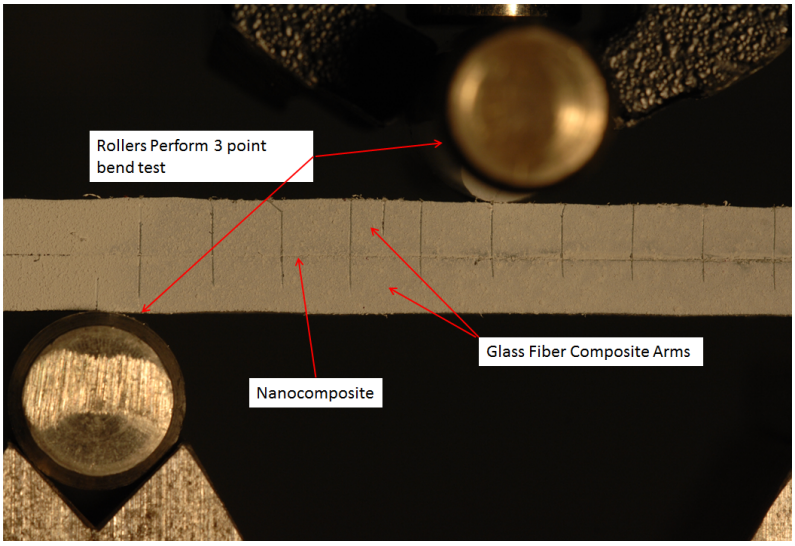

(b) End Notch Flexure Specimen

Figure 6.3: End Notch Flexure Schematic and Specimen

6.2 Determining Interlaminar mode II fracture toughness

5" by 0.5" End Notch Flexure(ENF) specimens are used to determine the interlaminar mode II fracture toughness. Films made by the LDSM on 5" by 5" plates are detached into free standing PU/PAA films. These films are then cut into 5" by 0.5" pieces and hot pressed between two fiber-glass arms. The sides of both arms are painted and marked such that the tip of the fracture surface can be easily identified. The arm is loaded in a three point bend fixture 6.3, where the center roller is depressed into the ENF specimen at 1mm/min. An image of the specimen is taken every 5 seconds.

The ENF tests are processed according to the analytic procedure presented in *Thouless* (2009). This is an analytic correction for the any shear in the glass composite

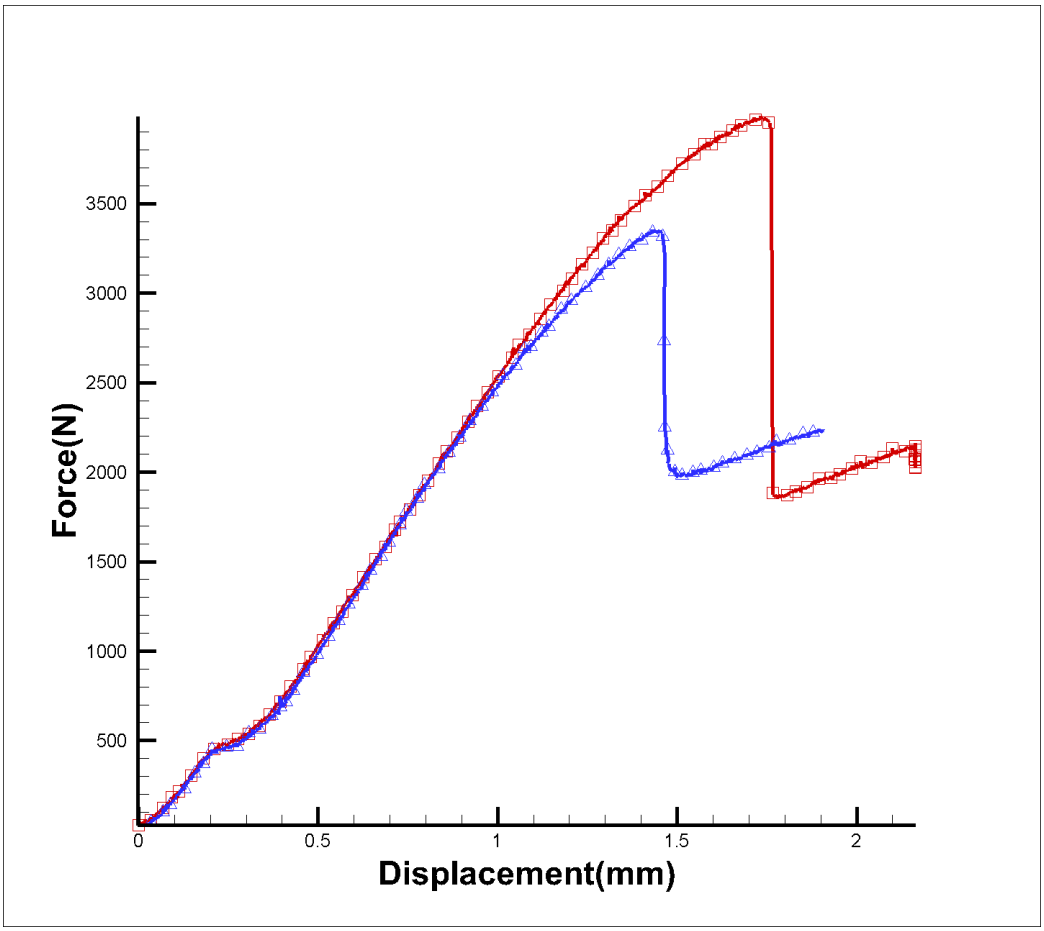

Figure 6.4: End Notch Flexure Test

beam arms of the ENF specimen, it does not correct for shear or deformation in the nanocomposite layer. The fracture toughness is calculated as:

$$\frac{E_1 h_1^3 G_{IIC}}{F^2 a^2} = \frac{9}{16}\left[1 + 0.21\frac{h}{a}\right]^2 \tag{6.1}$$

where E_1 is the young's modulus of the beam along the length of the ENF specimen, h_1 is the thickness of 1 arm of the ENF specimen, h is the thickness of the entire ENF specimen, F is the load applied to the center of the specimen and a is the length of the crack.

The tests reveal fracture toughnesses of 22.85 ± 3.75N/mm.

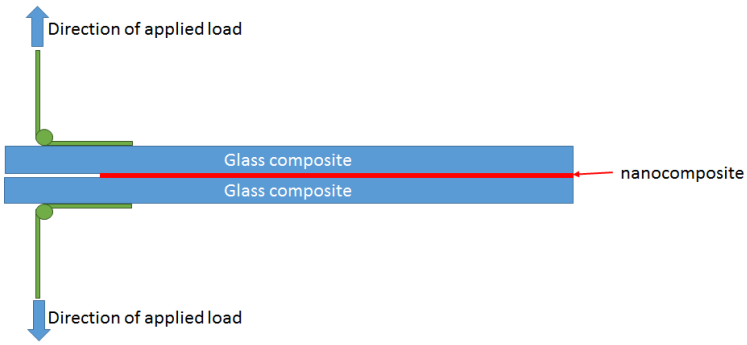

(a) Schematic of the End Notch Flexure Test

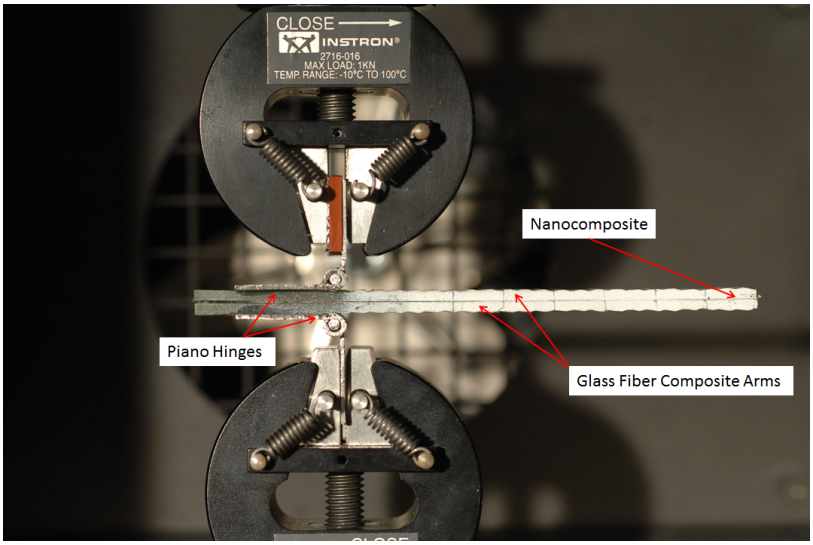

(b) End Notch Flexure Specimen

Figure 6.5: Double Cantilever Beam Schematic and Specimen

6.3 Determining Interlaminar mode I fracture toughness

5" by 0.5" Double Cantilever Beam(DCB) specimens are used to determine the interlaminar mode I fracture toughness. The DCB specimens are made with the same procedure as the ENF specimens in 6.2. After the DCB specimens are completed, a 2-ton epoxy is used to attach piano hinges to the specimens. An Instron Test Frame is used to load the finished specimens in tension at a displacement control rate of 1mm/min, as in figure 6.5.

We obtain the following force-displacement curve in figure 6.6, which is then processed using the compliance calibration method in *(Subcommittee-D30.06)* (2007).

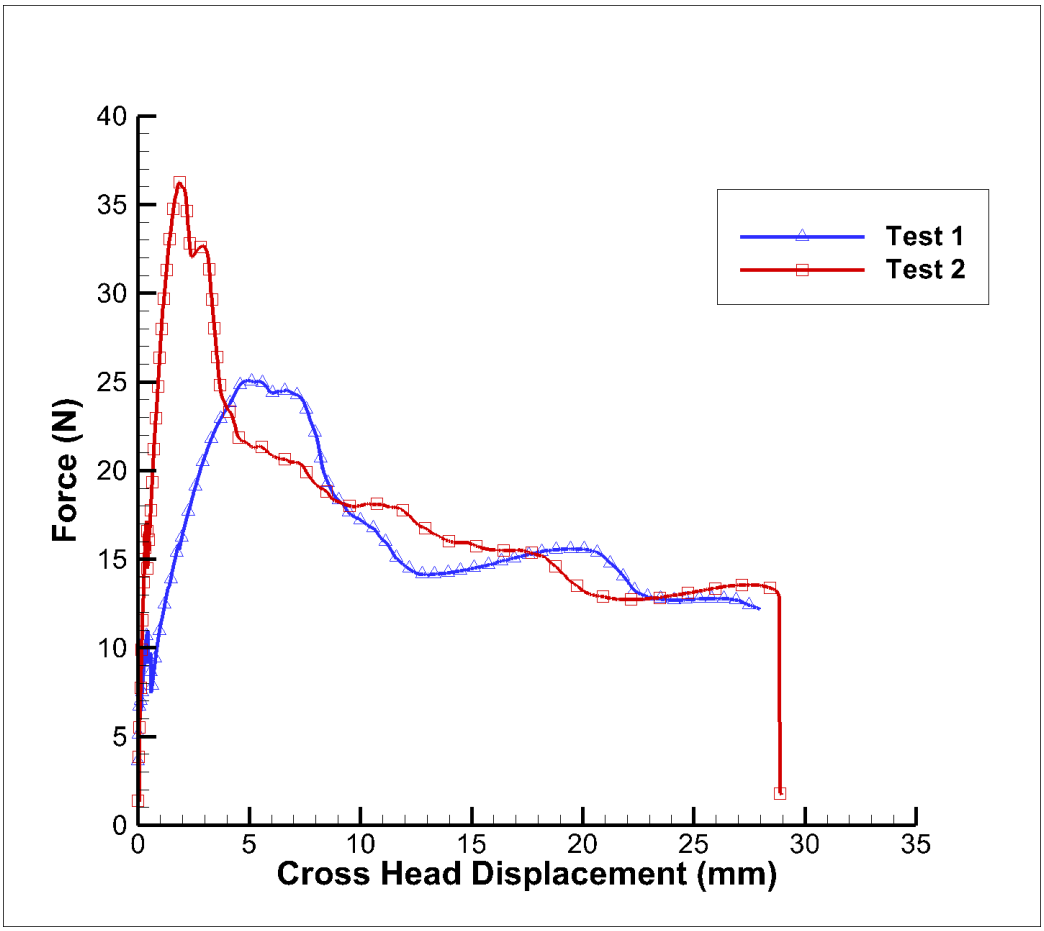

Figure 6.6: DCB Force Displacement

The Compliance is worked out in figure 6.7. Hence, the interlaminar fracture toughness is worked out in figure 6.8 as 0.53N/mm.

6.4 Conclusions

In this chapter, the interlaminar mode I and mode II fracture properties are measured. These can then be used as the first guess for the work in numerical modeling. These figures for fracture toughness and critical stresses are lower than those obtained by simulation in the subsequent chapter, indicating that other fracture mechanisms besides the pure modes induced by these tests are present in the impact specimen.

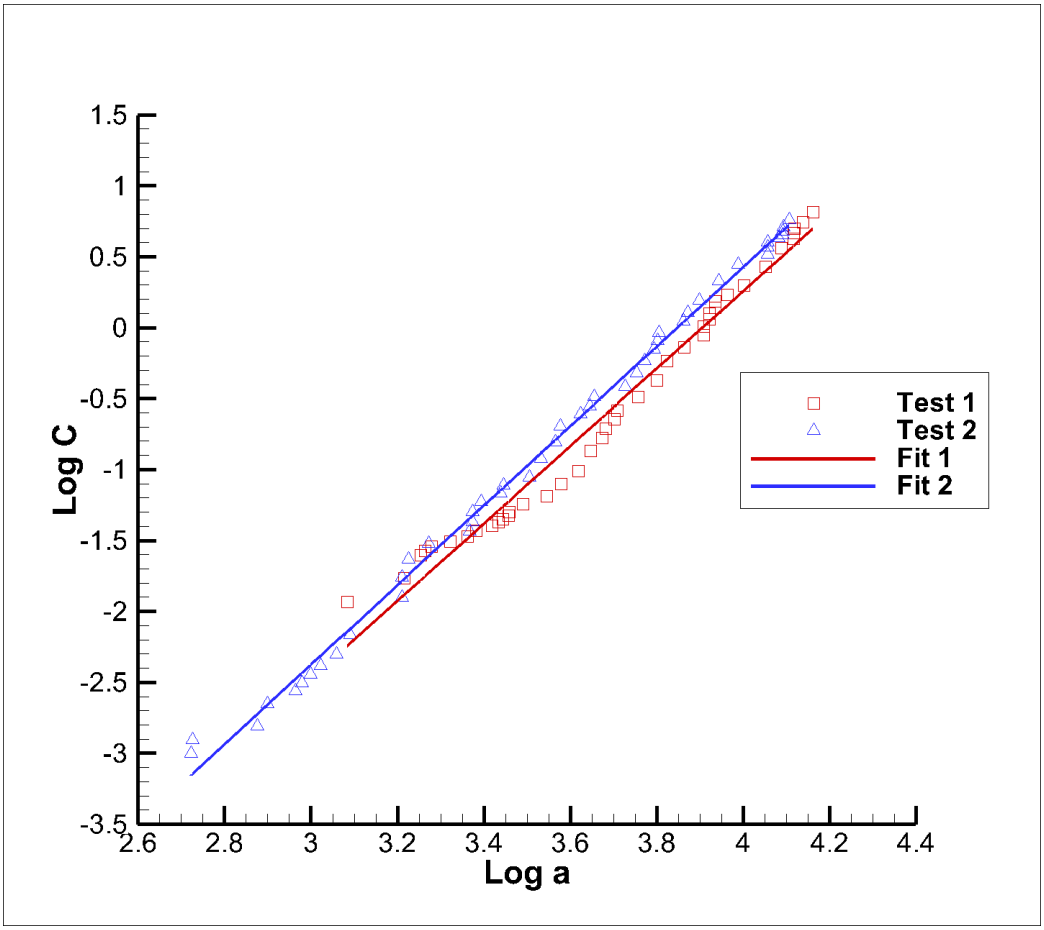

Figure 6.7: DCB Compliance Calibration

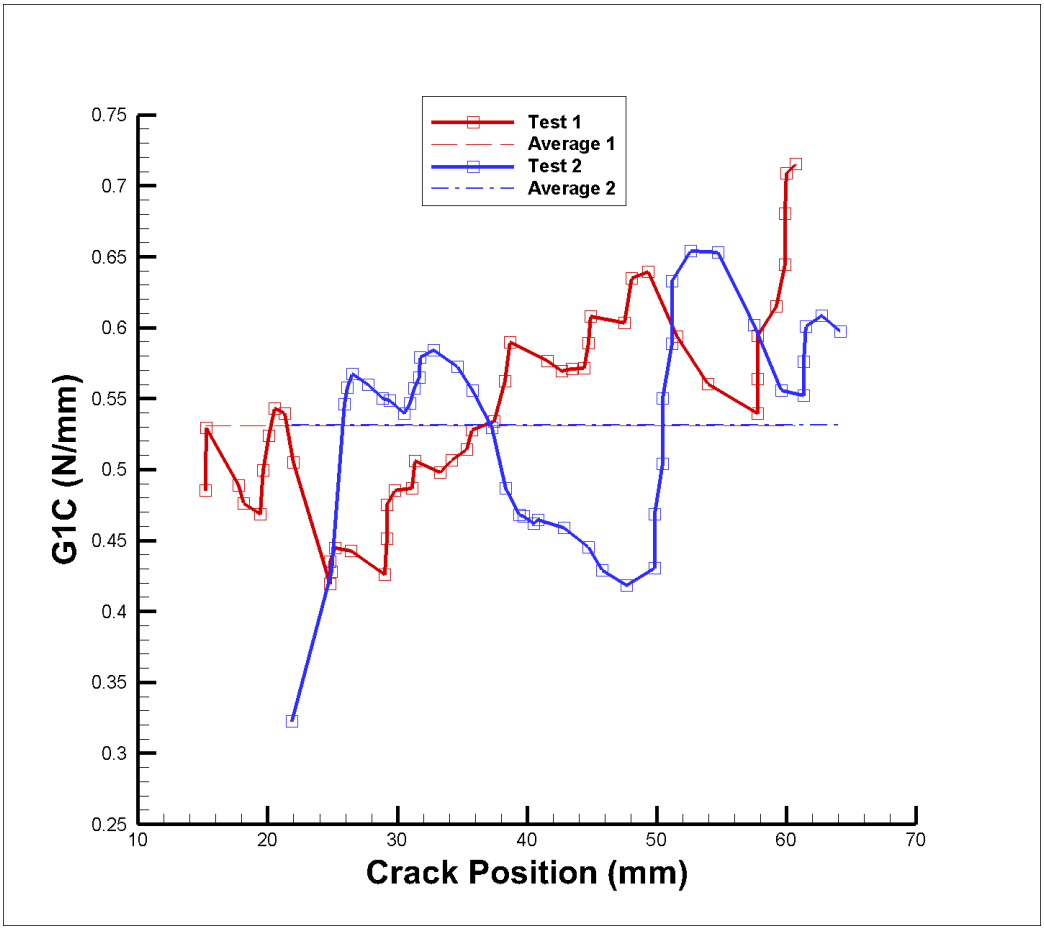

Figure 6.8: DCB Fracture Toughness

CHAPTER VII

NUMERICAL STUDIES ON GLASS/NANOCOMPOSITE/GLASS COMPOSITE

In this chapter, Finite Element (FE) based modeling studies are performed on the glass/nanocomposite/glass composite in order to understand the deformation response of the film layer in a layered armor system. All the work in this section is performed using the commercially available software package ABAQUS, using the dynamic explicit solver (version 6.10-1). First, in section 7.1, the static indentation of a boro-silicate glass is used to establish the FE methodology by comparison against an available analytic solutionand also characterize the correct modeling strategy for boro-silicate glass. Subsequently, the nanocomposite layer in the composite block is analyzed with an modified smeared crack user material model.

7.1 Characterization of Elastic Hertzian Contact

7.1.1 Analytic Elastic Hertzian Contact

The boro-silicate glass is characterized by the indentation of a 0.5" diameter steel pin on the thin edge of a 5" by 5" by 1" block of boro-silicate glass, the test setup

can be seen in figure 7.1. Force-Displacement data is recorded for comparison with the numerical model.

The elastic Hertzian contact problem is first analyzed, where the glass and indentation head are both assumed to have only an elastic stress response to applied strains. A reference used in this section of the work is the analytic elastic Hertzian contact solution found in *Popov* (2010). The force exerted by a rigid cylinder on an elastic half-space is obtained as:

$$F = \frac{\pi}{4} E^* l d \tag{7.1}$$

where l is the length of the contact, d is the depth of the indentation and E^*, the effective Young's modulus, is defined as

$$\frac{1}{E^*} = \frac{1-\nu_1^2}{E_1} + \frac{1-\nu_2^2}{E_2} \tag{7.2}$$

and E_1 and E_2 are the elastic moduli of the materials of the indenter and elastic half space and ν_1 and ν_2 are the poisson's ratios, respectively.

In addition to matching the elastic force-displacement response, stresses at various depths below the indenter can be compared *Johnson* (1987). The stress in the $y-z$ plane along $y = 0$ caused by an applied distributed load $p(s,0)$ can be found, by superposition, as:

$$\sigma_y(0,0,z) = -\frac{2z}{\pi} \int_{-a}^{b} \frac{p(s)(s^2)}{(s^2+z^2)^2} ds \tag{7.3}$$

$$\sigma_z(0,0,z) = -\frac{2z^3}{\pi} \int_{-a}^{b} \frac{p(s)}{(s^2+z^2)^2} ds \tag{7.4}$$

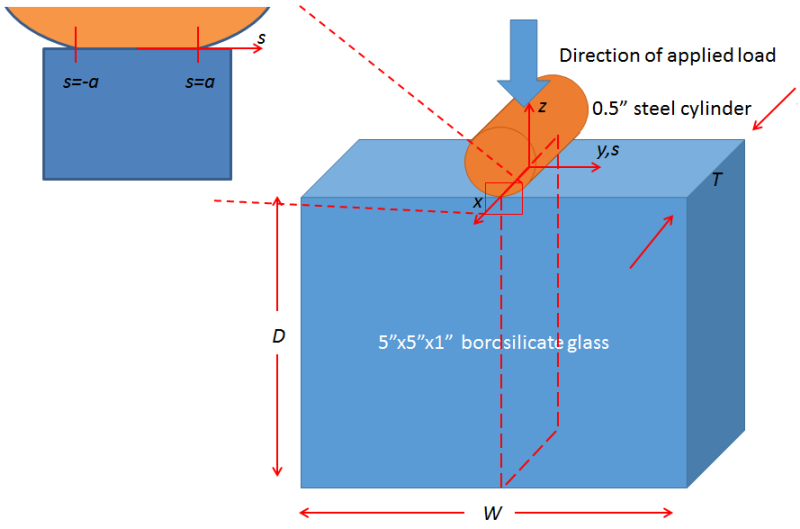

(a) Schematic of the Indentation test

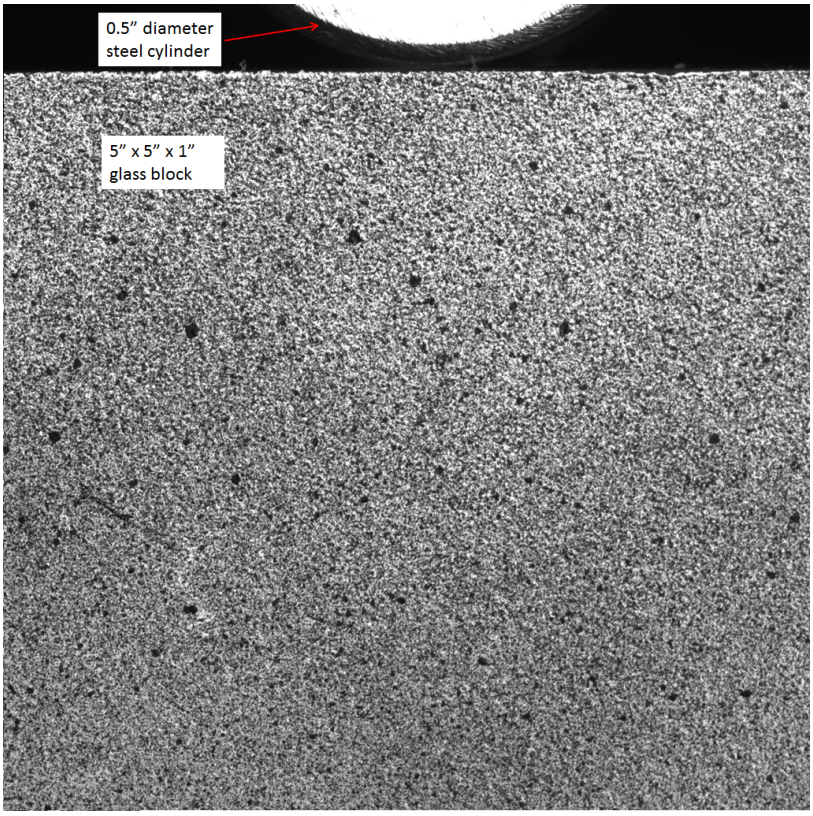

(b) Close up of specimen and indenter

Figure 7.1: Indentation Schematic and Close-up

$$\tau_{yz}(0,0,z) = -\frac{2z^2}{\pi}\int_{-a}^{b}\frac{p(s)(s)}{(s^2+z^2)^2}ds \tag{7.5}$$

where the s axis is parallel to the y axis and the pressure distribution $p(s,0)$ applied from $s=-a$ to $s=a$, the width of the contact zone, is

$$p(s,0) = p_o\left(1-\frac{s^2}{a^2}\right)^{\frac{1}{2}} \tag{7.6}$$

For a plane strain problem, the out of plane stress in the x axis can be found by

$$\sigma_x(0,0,z) = \nu\left(\sigma_y(0,0,z)+\sigma_z(0,0,z)\right) \tag{7.7}$$

Integrating equations B.10 through B.6 with the applied pressure distribution 7.6 and solving for B.10. We obtain analytically, the principal stresses, in directions as indicated in figure 7.1, are calculated as follows, as a function of depth below the indenter:

$$\sigma_x(0,0,z) = -2\nu p_{max}\left[\sqrt{\frac{z^2}{a^2}+1}-|\frac{z}{a}|\right] \tag{7.8}$$

$$\sigma_y(0,0,z) = -p_{max}\left[\left(2-\left(\frac{z^2}{a^2}+1\right)^{-1}\right)\sqrt{\frac{z^2}{a^2}+1}-2|\frac{z}{a}|\right] \tag{7.9}$$

$$\sigma_z(0,0,z) = -p_{max}\left[\sqrt{\frac{z^2}{a^2}+1}\right]^{-1} \tag{7.10}$$

where p_{max}, the maximum stress, is defined as

$$p_{max} = \frac{2F}{\pi a l} \tag{7.11}$$

where a, the half width of the contact area, is

$$a = \sqrt{\frac{\frac{4F}{E^*}}{\pi l \left(\frac{1}{R}\right)}} \tag{7.12}$$

and R is the radius of the indenter.

Note that the solutions listed as equations 7.8 through 7.10 are for an infinite half-space. For a glass block, where $T << L, D$, the stresses at the central plane below the indenter are well approximated by equations 7.8 through 7.10.

7.1.2 FE Elastic Hertzian Contact

The elastic Hertzian contact problem is also studied by the FE method, where the indentation of an elastic block with an elastic indenter is modeled. The FE model is composed entirely of C3D4 3D linear elastic elements, with a user specified element density (mesh density) along the centerline of the block directly under the indenter. No friction effects are included. The model with the lowest element density of 0.35mm/element can be seen in figure 7.2.

It is observed that there is good agreement in the force-displacement curves between the analytic elastic Hertzian contact solution and the elastic numerical model as seen in figure 7.3. However, neither the elastic FE force-displacement response nor the elastic analytical solution match the experimental force-displacement curve. This suggests that the assumptions of linear elasticity for the glass block, especially, under the indenter where the tresses are large, may be brought into question.

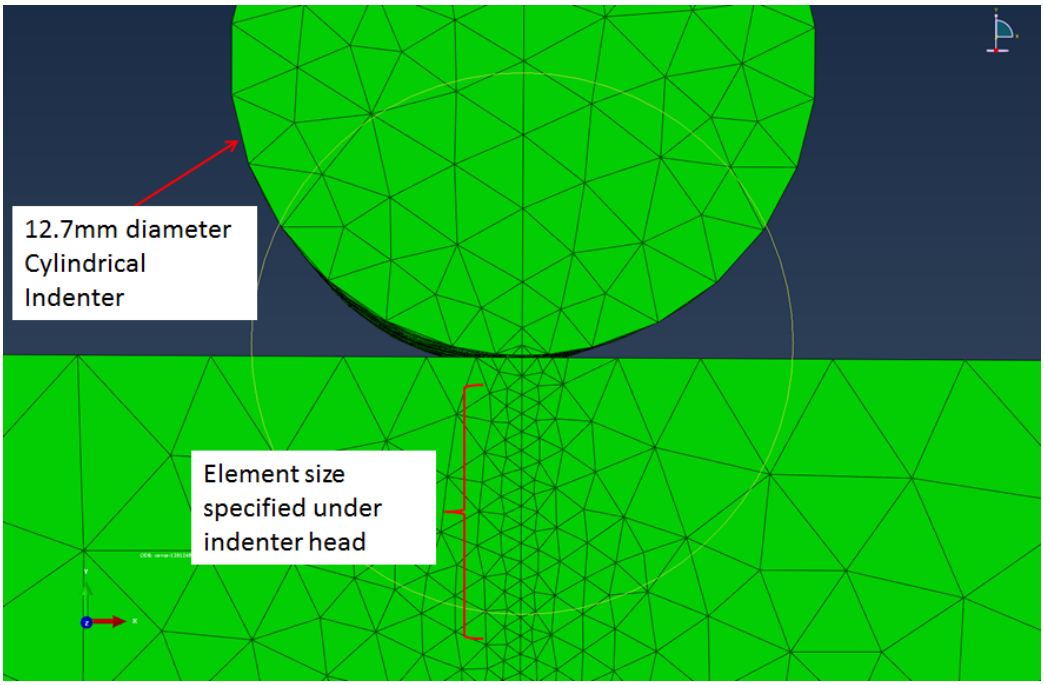

Figure 7.2: Finite Element Model used for Elastic Hertzian Study

In addition to matching the force-displacement response, the stresses along the line (0,0,z) are normalized with respect to p_{max} and compared with the analytic solution listed as equations 7.8 through 7.10. The results are shown in figure 7.4. It is observed that for various element sizes from 0.131mm to 0.35mm, for a 12.7mm diameter indentor, the normalized stress values closely match the expected analytic solution compared at various depths below the point of indentation.

It is concluded that there is no element size dependence in the FE model, in the range of element sizes used, in the description of two elastic bodies in frictionless elastic contact. Therefore, this range of element sizes (and mesh density) will be used in subsequent work, which will incorporate material nonlinearity (plasticity), material distributed damage (microcracking) and subsequent failure by macroscopic (localized) fracture.

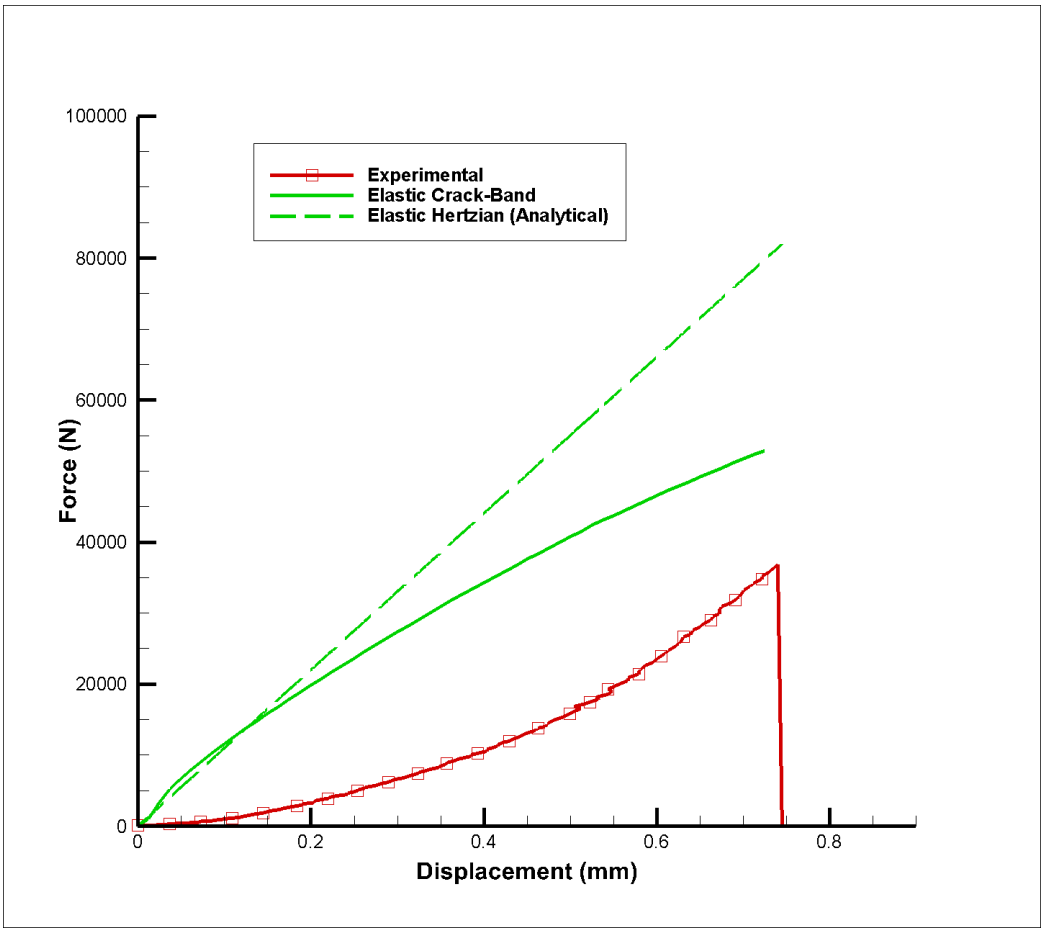

Figure 7.3: Force-Displacement response for Elastic Glass Indentation FE model and Elastic Analytic Solution compared to the Experimental Data

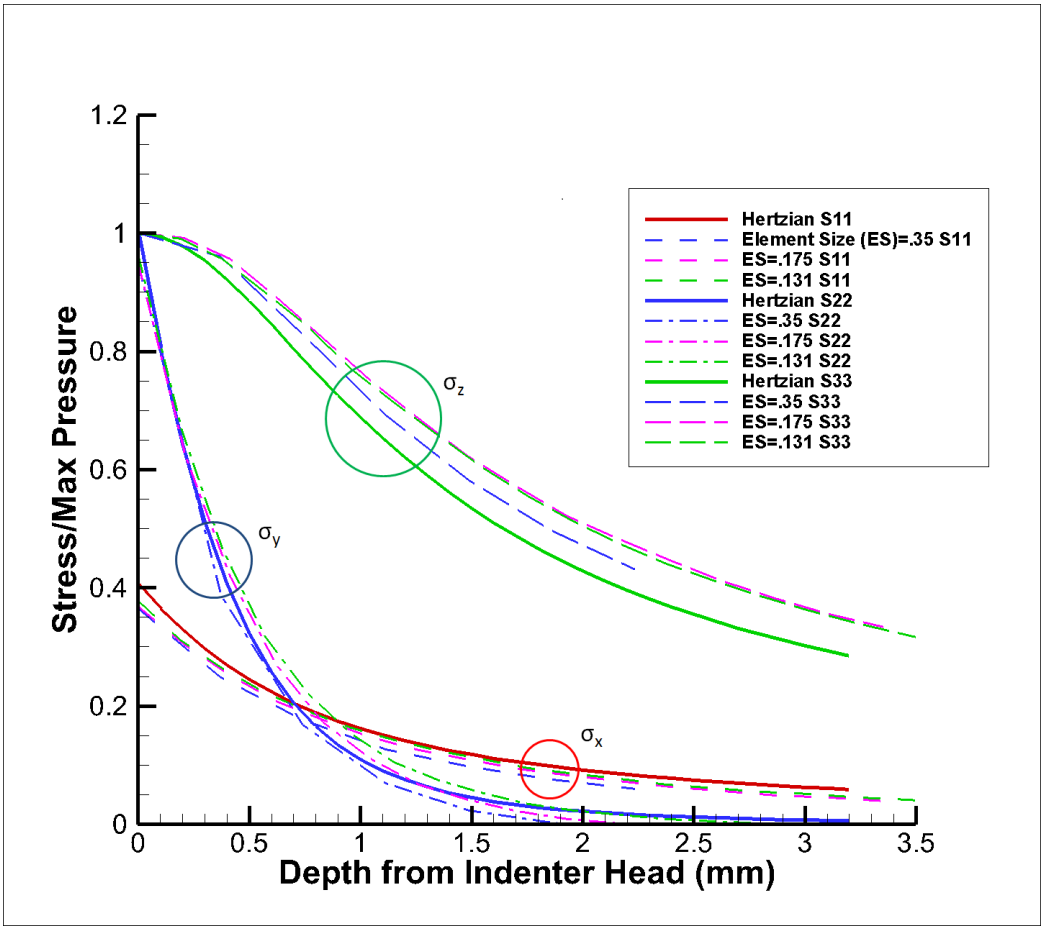

Figure 7.4: Analytical vs Numerical Stress-Depth responses for Indentation

7.2 Characterization of the Plastic Response of Boro-silicate Glass

It is noted from the force displacement response in figure 7.3 that there is much non-linearity in the experimental result, with respect to the analytical elastic and numerical elastic solutions. The experimental force displacement response is also much "shallower" than the elastic curve, indicating that material softening (i.e. plasticity) is present in boro-silicate glass before fracture. It is observed that the experimental response is a much softer than the purely elastic solution, but does display hardening as the pressure is increased; These are both characteristics of the Drucker Prager material model that captures plasticity and shows differences in tensile and compressive responses in the plastic regime, *MacDonald* (2011). Additionally, it is noted from the observed fracture mechanisms that boro-silicate glass is anomalous, which are typically described by a hydrostatic pressure dependent yield condition.

A numerical Drucker Prager model for boro-silicate glass is described in detail in *Chocron et al.* (2009), and the Drucker-Prager model is available as a built-in material model in Abaqus. The Drucker Prager description states that the yield stress of a material varies linearly with respect to the hydrostatic pressure experienced by the material, this property is listed as β in table 7.1. This results in a varying yield stress, Y, with respect to hydrostatic pressure, P, as follows:

$$Y = Y_o + \beta P \tag{7.13}$$

The properties provided by *Chocron et al.* (2009) only describe the yielding behavior of glass under hydrostatic compression. It is noted that the Drucker Prager model results, obtained by the FE method, more accurately matches the experimental force-displacement response up to failure than either of the purely elastic descriptions in figure 7.5.

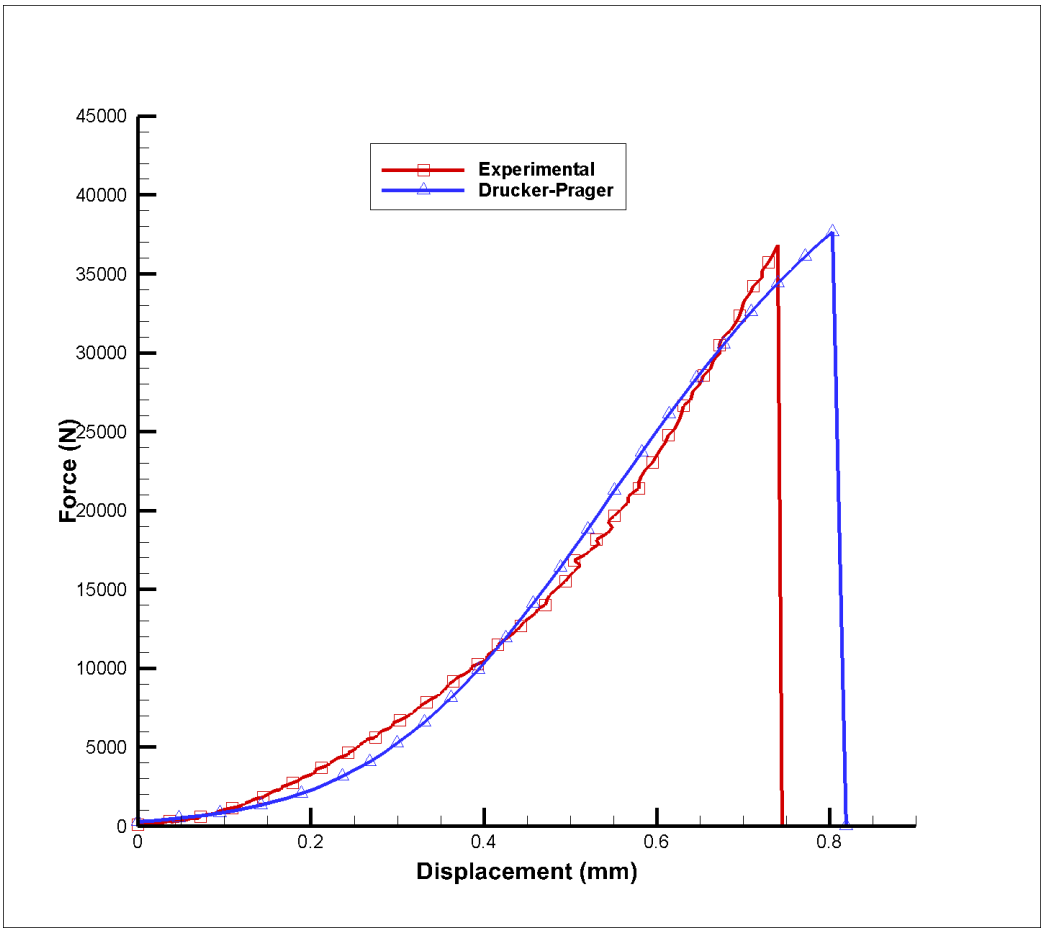

Figure 7.5: Force-Displacement response for Drucker Prager FE model compared to the Experimental Data

It is concluded that the numerical Drucker Prager model accurately describes the plastic behavior of boro-silicate glass under indentation.

7.3 Characterization of the Fracture Response of Boro-silicate Glass

The experimental indentation test shows the test specimen fracture in a brittle fashion at a maximum applied force of 36.8kN.

The damage observed in the experimental indentation test can be described by the built-in shear damage model which can be used in conjunction with the Drucker Prager model in Abaqus. Since these properties are not provided in *Chocron et al.* (2009), shear damage properties of critical plastic shear strain and fracture toughness are calibrated to match the brittle failure of the indentation experiment. It is assumed that the softening post-initiation is linear. These values are calibrated after the value for β has been validated in the previous section.

It is observed that the force-displacement responses of the indentation experiment and the prediction from the numerical Drucker Prager model are in good agreement up to the point of fracture as shown in figure 7.5. It is also observed in figure 7.5 that the maximum applied force for the finite element simulation of 37.6kN closely matches that of the experiment of 36.8kN. The property values for the shear damage model are shown in table 7.1 and are used for the boro-silicate glass model in subsequent impact modeling.

A set of numerical simulations was also performed based on the impact of the pure glass samples. These simulations showed that small amounts of damage to the glass were detected at an impact velocity of 4.25m/s. No damage was detected at 3.75m/s. A large amount of damage is observed at 10m/s. Since it is not possible

Material Property	Symbol	Value
Young's Modulus	E	$72000\,[MPa]$
Poisson's Ratio	υ	0.203
Material angle of friction	β	47.7°
Yield Stress	σ_y	$80\,[MPa]$
Initiation Plastic Shear Strain	γ_i	0.0195
Fracture Toughness	G_{IIC}	$0.75\,[Nmm^{-1}]$

Table 7.1: Material parameters for Borosilicate Glass

to visually detect the amount of damage observed in the numerical simulation of an impact velocity of 4.25m/s and the damage observed in the simulation at 10m/s more closely matches the size of the damaged region in the experiment, it is concluded that the shear damage model and Drucker Prager simulation closely reflect the pure glass experiments in the previous chapter.

It is concluded that the built in shear damage model can describe the fracture behavior of boro-sillicate glass.

7.4 Modified Smeared Crack Model

A Modified Smeared Crack model is used to numerically model the PU/PAA nanocomposite in the glass composite blocks. A description of the original model may be found in *Heinrich and Waas* (2013). It was necessary to limit the fracture modes to only the shearing modes between layers in the nanocomposite.

The response prior to fracture is elastic. In the Post fracture state, the strains in an element can be decomposed into continuum and crack portions:

$$\varepsilon = \varepsilon^{co} + \varepsilon^{cr} \tag{7.14}$$

where any reference to the continuum, such as ε^{co}, is taken to be linearly elastic in this formulation. All the quantities are given in the global coordinate system. The

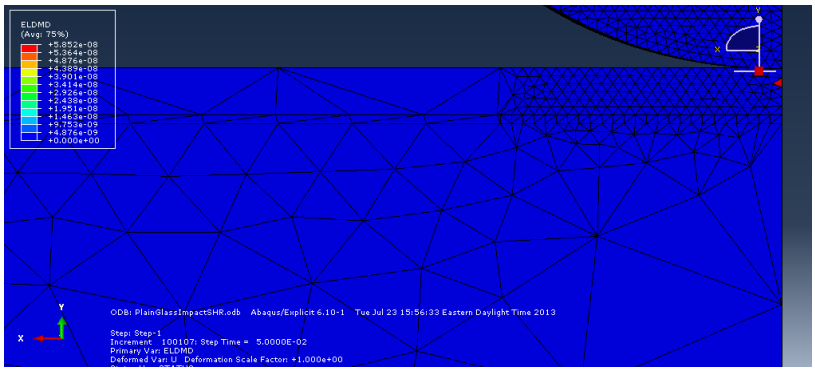

(a) Glass Block impact at 4.25m/s

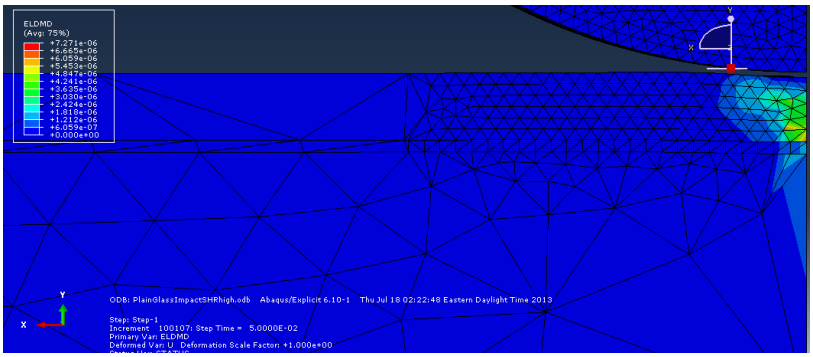

(b) Glass Block impact at 10m/s

Figure 7.6: Numerical Simulation of Glass Block Impact

crack strains can be transformed from the global to the local crack coordinate system via the transformation law $\boldsymbol{N}$, a [3x3] matrix where $\boldsymbol{N}^{-1} = \boldsymbol{N}^{T}$, as

$$\boldsymbol{\varepsilon}^{cr} = \boldsymbol{N}\boldsymbol{e}^{cr} = \boldsymbol{N} \begin{bmatrix} \varepsilon^{cr}_{norm} \\ \gamma^{cr}_{t1} \\ \gamma^{cr}_{t2} \end{bmatrix} \tag{7.15}$$

Here ε^{cr}_{norm} is the crack strain component normal to the crack (i.e. crack gap) and γ^{c}_{t1} and γ_{t2} are the crack strain components tangential to the crack surface (i.e. slip). In a similar fashion, the global stress state $\boldsymbol{\sigma}$ can be transformed to obtain the tractions at the crack interface $\boldsymbol{s}^{cr}$

$$\boldsymbol{s}^{cr} = \begin{bmatrix} \sigma^{cr}_{norm} \\ \tau^{cr}_{t1} \\ \tau^{cr}_{t2} \end{bmatrix} = \boldsymbol{N}^{T}\boldsymbol{\sigma} \tag{7.16}$$

The above strain and stress values in the global coordinate and crack coordinates are related by $\boldsymbol{N}$. In the original smeared crack formulation, the Rankine criterion is used for determining the onset of crack formation, where fracture occurs when a maximum principal tensile stress exceeds a critical stress value. Thus, the global coordinate system can be translated to the local crack coordinate system, where $\boldsymbol{N}$ is transformation tensor from the principal stress directions to the global coordinate system. In the modified formulation used to model shearing between layers only, $\boldsymbol{N}$ is given as a modified identity matrix transforming the global coordinate system to the coordinate system where the z axis and 3 axis are the normal to the layers in the nanocomposite. Instead of the Rankine criterion, the onset of crack formation is determined when the maximum shear stress in the $x - y$ plane exceeds a critical

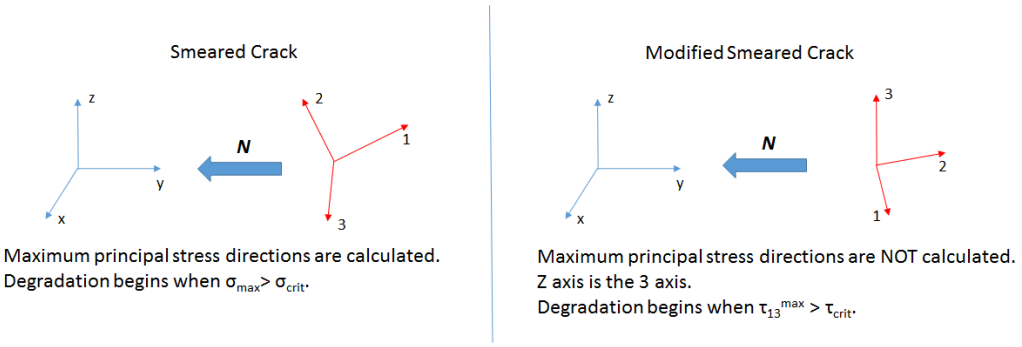

Figure 7.7: Modifications to Smeared Crack Model

shear stress value. The maximum shear stress is expressed as:

$$\tau_{13}^{max} = \sqrt{\tau_{xz}^2 + \tau_{yz}^2} \tag{7.17}$$

A summary of the modifications to the smeared crack model can be seen in figure 7.7.

The local crack stress is calculated from the local crack strain using a secant stiffness matrix,$\boldsymbol{D}^{cr}$, and a damping matrix, $\boldsymbol{D}^{da}$:

$$\boldsymbol{s}^{cr} = \boldsymbol{D}^{cr}\boldsymbol{e}^{cr} + \boldsymbol{D}^{da}\dot{\boldsymbol{e}}^{cr} \tag{7.18}$$

The damping matrix makes the crack progression a time-dependent property. It can also be used to smoothen the numerical solution scheme. Any numerical solution scheme involves a discrete time step. The crack strain rate is accordingly approximated with finite differences.

$$\dot{\boldsymbol{e}}^{cr} \approx \frac{\boldsymbol{e}^{cr}(t+\Delta t) - \boldsymbol{e}^{cr}(t)}{\Delta t} = \frac{\boldsymbol{e}^{cr} - \boldsymbol{e}^{cr}_{old}}{\Delta t} \tag{7.19}$$

The crack stress can finally be expressed as

$$\boldsymbol{s}^{cr} = \boldsymbol{D}^{cr}\boldsymbol{e}^{cr} + \frac{1}{\Delta t}\boldsymbol{D}^{da}\boldsymbol{e}^{cr} - \frac{1}{\Delta t}\boldsymbol{D}^{da}\boldsymbol{e}^{cr}_{old} \tag{7.20}$$

The expanded equation (7.20) yields

$$\begin{aligned}
\begin{bmatrix} \sigma^{cr}_{norm} \\ \tau^{cr}_{t1} \\ \tau^{cr}_{t2} \end{bmatrix} &= \begin{bmatrix} E^{cr}(\varepsilon^{cr}_{norm}) & 0 & 0 \\ 0 & G^{cr}(\varepsilon^{cr}_{norm}) & 0 \\ 0 & 0 & G^{cr}(\varepsilon^{cr}_{norm}) \end{bmatrix} \begin{bmatrix} h \cdot \varepsilon^{cr}_{norm} \\ h \cdot \gamma^{cr}_{t1} \\ h \cdot \gamma^{cr}_{t2} \end{bmatrix} \\
&+ \frac{1}{\Delta t} \begin{bmatrix} \eta & 0 & 0 \\ 0 & \eta & 0 \\ 0 & 0 & \eta \end{bmatrix} \begin{bmatrix} h \cdot \varepsilon^{cr}_{norm} \\ h \cdot \gamma^{cr}_{t1} \\ h \cdot \gamma^{cr}_{t2} \end{bmatrix} \\
&- \frac{1}{\Delta t} \begin{bmatrix} \eta & 0 & 0 \\ 0 & \eta & 0 \\ 0 & 0 & \eta \end{bmatrix} \begin{bmatrix} h \cdot \varepsilon^{cr}_{norm} \\ h \cdot \gamma^{cr}_{t1} \\ h \cdot \gamma^{cr}_{t2} \end{bmatrix}_{old}
\end{aligned} \tag{7.21}$$

where σ^{norm} is the normal traction across the crack surface and $E_{cr}(\varepsilon^{cr}_{norm})$ is the tensile secant stiffness across the crack surface. The crack shear stiffness G^{cr} is given here as a function of the normal crack opening $\varepsilon^{crack}_{norm}$ only and is the same in the 2 and 3 directions. This implies that locally, the crack response is purely mode II dominated. η is assumed to be the same in all directions, although this is not necessary.
The constitutive relation for the continuum is given by,

$$\boldsymbol{\sigma} = \boldsymbol{D}^{co}\boldsymbol{\varepsilon}^{co}, \tag{7.22}$$

where $\boldsymbol{D}^{co}$ is the secant stiffness of the continuum. Combining equations 7.14, 7.20 and 7.22, yields an implicit relation between the crack strain and the total elastic strain.

$$\boldsymbol{e}^{cr} = \left[\boldsymbol{D}^{cr}(\boldsymbol{e}^{cr}) + \boldsymbol{N}^T\boldsymbol{D}^{co}\boldsymbol{N} + \frac{1}{\Delta t}\boldsymbol{D}^{da}\right]^{-1}\left[\boldsymbol{N}^T\boldsymbol{D}^{co}\boldsymbol{\varepsilon}^{elcr} + \frac{1}{\Delta t}\boldsymbol{D}^{da}\boldsymbol{e}^{cr}_{old}\right] \tag{7.23}$$

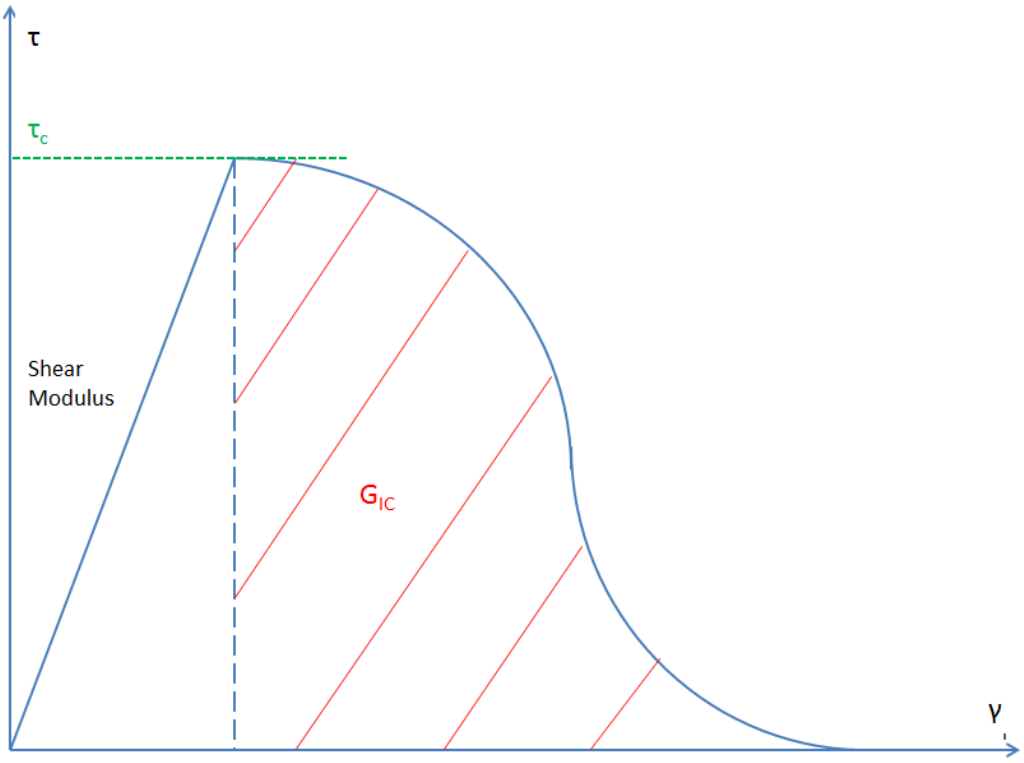

Figure 7.8: Schematic for the Shear Stress-Shear Strain Curve in the maximum principal stress direction for smeared Crack Material

Finally, using equations 7.14, 7.22 and 7.23, the relation between global stress and total strain in the post fracture regime is found as,

$$\begin{aligned}\boldsymbol{\sigma} &= \left[\boldsymbol{D}^{co} - \boldsymbol{D}^{co}\boldsymbol{N}\left(\boldsymbol{D}^{cr} + \boldsymbol{N}^T\boldsymbol{D}^{co}\boldsymbol{N} + \frac{1}{\Delta t}\boldsymbol{D}^{da}\right)^{-1}\boldsymbol{N}^T\boldsymbol{D}^{co}\right]\boldsymbol{\varepsilon}^{elcr} \\ &- \frac{\boldsymbol{D}^{co}\boldsymbol{N}}{\Delta t}\left[\boldsymbol{D}^{cr}(\boldsymbol{e}^{cr}) + \boldsymbol{N}^T\boldsymbol{D}^{co}\boldsymbol{N} + \frac{1}{\Delta t}\boldsymbol{D}^{da}\right]^{-1}\boldsymbol{D}^{da}\boldsymbol{e}^{cr}_{old} \end{aligned} \tag{7.24}$$

A schematic for the shear stress vs shear strain response in the direction of maximum principal shear stress for the smeared crack is included in figure 7.8. This numerical model is used to simulate the PU/PAA nanocomposite layer in the glass composite blocks, where τ_C and G_{IC} have to be determined from the simulation of the impact experiments.

The modified smeared crack model is validated by simulating the End Notch Flexure test performed in the previous chapter. The results are included in appendix C.

7.5 Numerical Impact models

A quarter Symmetry model with 136672 C3D4 elements is used for the numerical impact test. The boro-silicate glass is described by the Drucker-Prager material model, while the nanocomposite film is described by a 3D elastic crack band material model, which has the stress-strain behavior described in figure 7.8 in the maximum principal direction.

The spherical indenter is given various initial velocities, The inch thick glass block is queried for element energy expended in damage. The first velocity at which damage is observed in the inch thick glass block is recorded for various fracture properties in the film layer. Across all the simulations, a highest observed intact/fracture transition is observed at 28.0/30.0 m/s. This closely matches the intact/fracture transition of the monolithic PU and layered PU/PAA of 23.2/26.9 m/s and 26/32 m/s respectively seen in table 5.1; it is lower than that of the $(PU/PAA/(PU/Clay)_5)_{XX}$ nanocomposite.

Material Property	Symbol	Value
Young's Modulus	E	$700\,[MPa]$
Poisson's Ratio	ν	0.3
Critical Principal Shear Stress	τ_c	$30\,[MPa]$
Fracture Toughness	G_{IC}	$954\,[Nmm^{-1}]$

Table 7.2: Material parameters for DCZM

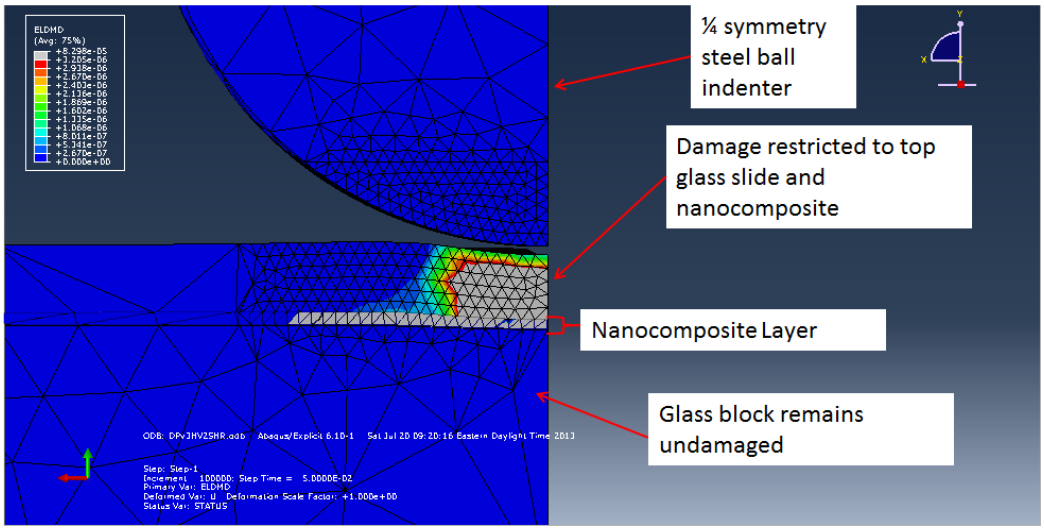

Figure 7.9: Energy Expended in Damage at Indenter Velocity = 28m/s, blue elements are undamaged

Looking at the damaged regions in 7.9, it is observed that the inch thick glass is undamaged, while the film and the 1.1mm thick glass are heavily damaged under the indenter. In addition, it is observed in 7.10, which was an impact at 40m/s, that the 1.1mm thick glass, the film and the inch thick glass block are heavily damaged under the indenter.

7.6 Energy Balance

The Energy Balance of the 28m/s and 31m/s impact cases are considered in this section. Abaqus is requested to output the history of total energy of native abaqus elements and materials at even intervals. Abaqus is able to differentiate between several important types of energy such as kinetic, elastic strain, plastic dissipation and damage dissipation. Abaqus is unable to output the energy of the elements described with the user material, it is assumed that all energy unaccounted for in the

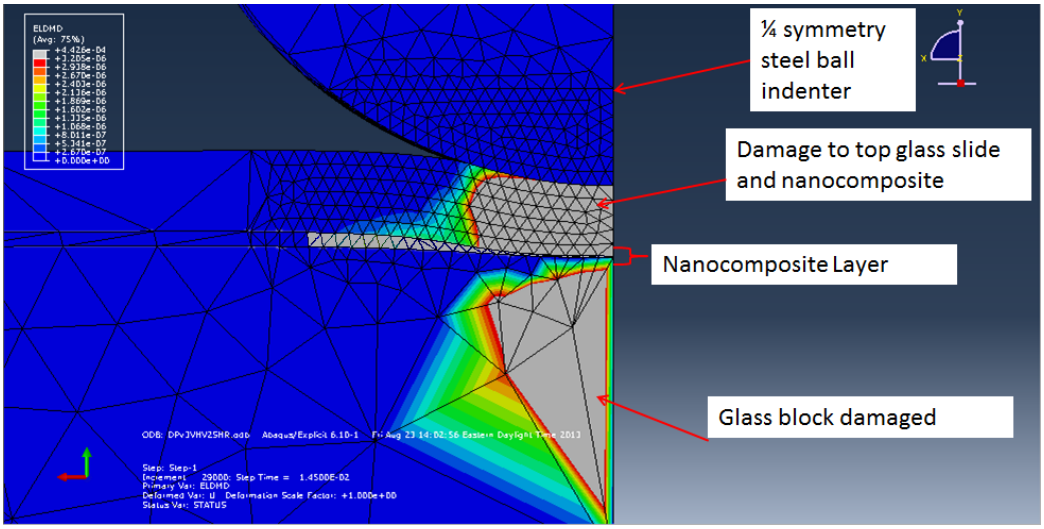

Figure 7.10: Energy Expended in Damage at Indenter Velocity = 31m/s, blue elements are undamaged

native abaqus elements and materials resides in the modified smeared crack material. The energy balance history for the 28m/s and 31m/s impact cases are included in figures 7.11.

It is shown that the amount of energy dissipated through fracture by modified smeared crack material is saturated at the highest velocity without damage to the lower glass block. The total energy dissipated in fracture of the nanocomposite is 7.0 ± 0.27Nmm. The higher kinetic energy of the impact projectile in the 31m/s case is accounted for in the plastic and damage dissipation in the glass slide and glass block. The final energy balance at the end of the simulation is recorded in table 7.3 and all energies in the table refer to the final value at the end of the simulation, except the original kinetic energy which is stated. The proportion of each energy is expressed as a percentage of the original energy input in table 7.3 as well.

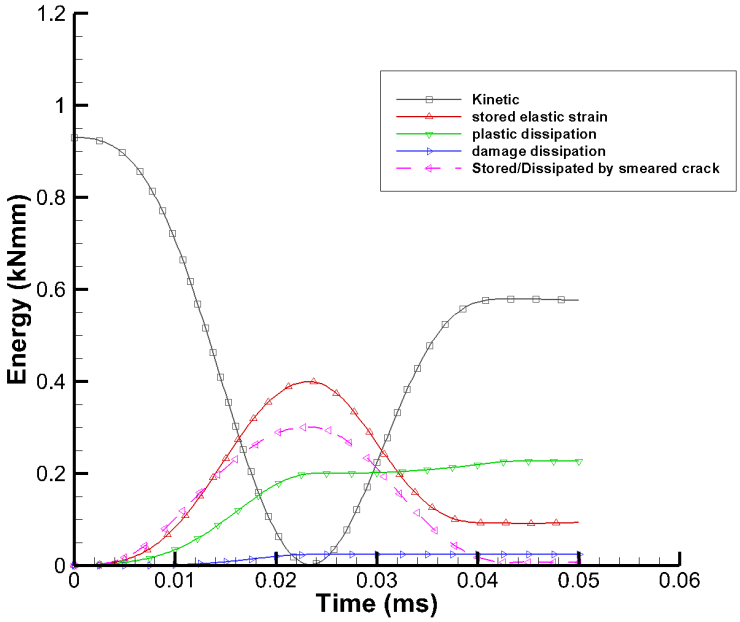

(a) Energy Balance of 28m/s Impact

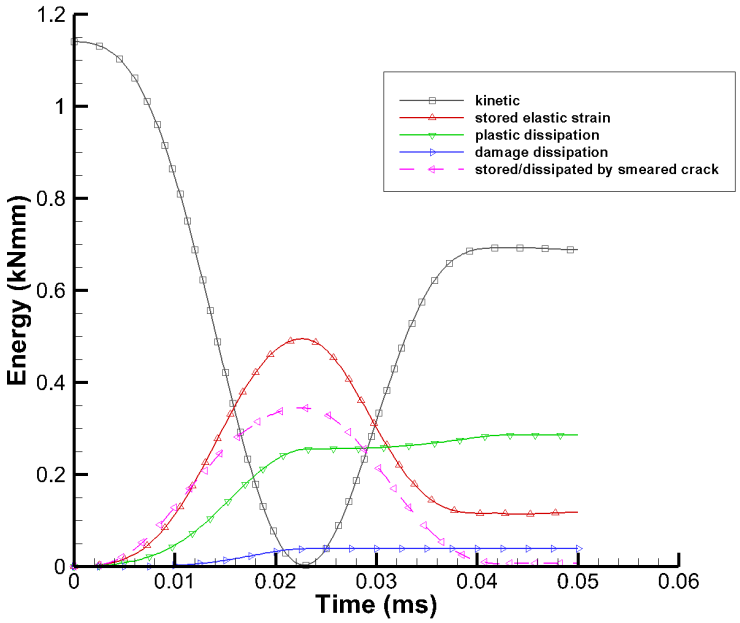

(b) Energy Balance of 31m/s Impact

Figure 7.11: Impact Energy Balance at 28m/s and 31m/s Impact Simulation

Energy Type	Impactor Velocity of 28m/s ($kNmm$)	Impactor Velocity of 31m/s ($kNmm$)
Original Kinetic Energy	0.930	1.140
Kinetic Energy	0.576 (61.9%)	0.688 (60.4%)
Elastic Strain	0.0937 (10.1%)	0.118 (10.4%)
Plastic Dissipation	0.227 (24.4%)	0.286 (25.1%)
Damage Dissipation	0.0244 (2.62%)	0.0391 (3.43%)
Smeared Crack Dissipation	0.00725 (0.78%)	0.0067 (0.59%)

Table 7.3: Impact Final Energy Balance and proportion of original energy input

7.7 Comparison of fracture toughness values

Comparing the values obtained in table 7.2 to figures previously recorded in subsections 3.3.6 and table VI, we see that the critical principal stress value in shear is similar previously obtained values of 28MPa for the in plane mode I critical stress. The increase in critical shear stress from about 7.5MPa measured in the ENF test (see appendix C) to 30MPa, as determined from the numerical study, can be explained through the Mohr-Coulomb model *Hoek* (1990). That is, the critical shear stress for fracture initiation is assumed to increase linearly with the applied normal stress as shown in figure 7.12.

The impact fracture toughness of 954N/mm is an order of magnitude higher than previously obtained values, since it is to be noted that not all the energy absorbing mechanisms are included in the simulations. Notable mechanisms left out in this work are the fracture stepping mechanism observed in subsection 5.4.1 and the sliding friction energy dissipation in the crack wake of all the shear fracture between the sublayers in the LBL film. The absence of these mechanisms in the coupon level measurements result in a much larger fracture toughness estimation than expected.

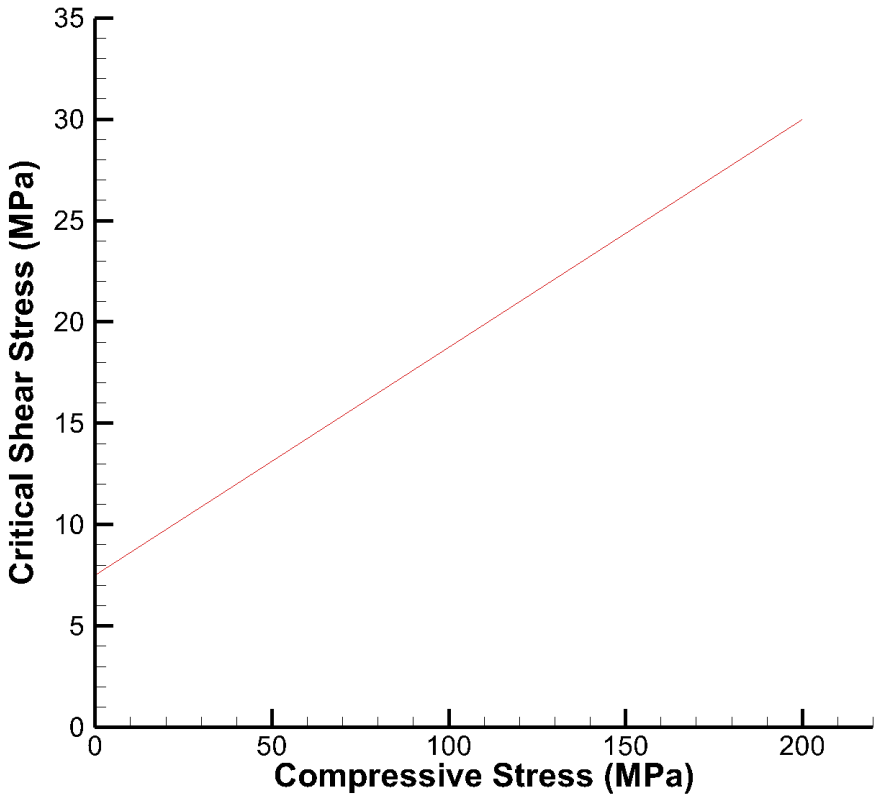

Figure 7.12: Effect of Compressive Stress on Critical Shear Stress

7.8 Conclusions

In this section, it is observed that the monolithic PU and PU/PAA films under impact can be numerically modeled using an elastic crack band model. Abaqus routines can accurately model the Hertzian contact and Boro-silicate glass material response. A modified smeared crack user material model is used to simulate the PU/PAA nanocomposite layer. The numerical model shows a consistent critical stress from previous chapters. However, the fracture toughness recorded is an order of magnitude higher than values obtained in previous chapters. This indicates that much more energy is absorbed through the mixed mode fracture and frictional sliding in the crack wake than in any of the single mode fracture the nanocomposite undergoes.

CHAPTER VIII

CONCLUSIONS AND ORIGINAL CONTRIBUTIONS

In this thesis, a novel material, which can be potentially used in transparent armor, is manufactured on a large scale and is used in improving the resistance to ballistic damage of a glass block. The fracture properties of this layered nanocomposite are determined as a free standing film and as part of a composite block under quasi-static and impact loading conditions. Multiple experimental results demonstrate that these films fail preferentially in shear in the plane of the film, due to their unique manufacturing method. A free standing film with an induced crack is observed, SEM in-situ, to fail in shear in the plane of the film despite being loaded in a direction in the plane of the film. In the composite block, which consists of two glass blocks sandwiching a nanocomposite film, under high speed indentation, it is observed that a cone shaped shear plane originating under the indenter develops, absorbing energy and limiting damage to the film and glass past the shear plane. The cone shaped fracture steps across many layers of the nanocomposite, resulting in fracture of individual layers, shear between layers and sliding between layers, absorbing much more energy than through fracture in any single mode. It is also shown that the PU and PU/PAA films in the composite block can be modeled as a isotropic elastic body which can absorb energy through fracture.

In chapter I, various forms of transparent armor systems are presented for comparison to the transparent armor systems incorporating LBL nanocomposite. In Chapter II, the design and assembly of a LSDM are presented, it is concluded that LBL films manufactured this way are of similar or superior quality to other methods of LBL deposition, while greatly increasing the deposition rate and the surface area of the deposition. In chapter III, the mode I fracture toughness of a LBL nanocomposite is determined parallel to the surface of the nanocomposite using a novel method which separates the energy expended in plastic deformation from energy expended in fracture for a plane stress specimen.

In chapter IV, it is shown that various fracture mechanisms unique to LBL nanocomposites are observed SEM in-situ. These fracture mechanisms suggest that LBL nanocomposites are susceptible to mode II shear fracture between nanolayers under most loading conditions. In chapter V, high speed impact experiments performed induced this delaminating fracture mechanism in a transparent armor system, consisting of two boro-silicate glass pieces sandwiching a LBL nanocomposite. In chapter VI, various fracture toughnesses of the LBL nanocomposites are obtained experimentally. In chapter VII, Finite Element studies on the LBL nanocomposite sandwich armor system are presented. It is possible to represent the LBL nanocomposite with an elastic smeared crack model and the boro-silicate glass with a drucker prager model that incorporates shear damage. The resulting numerical model can accurately predict the indenter velocity necessary to induce fracture in the protected boro-silicate glass layer, and produce fracture patterns observed in the experiment.

8.1 Suggestions for future studies

• Develop an anisotropic elastic with anisotropic fracture material model to model the behavior of $(PU/PAA/(PU/Clay)_5)_{XX}$ nanocomposite in the composite block

under high speed indentation.

• Incorporate different materials in order to increase the fracture toughness in the mode II shear, while keeping the critical stress low.

• Determine the lowest number of bilayers at which the shearing mechanism is active under impact.

• Investigate other nanoparticle/polymer systems manufactured using LBL to optimize the films for increasing impact energy absorption.

APPENDICES

APPENDIX A

Fisher's Exact Test

The data presented in the experimental impact tests contains two statements per data point. They are:

1. Specimen A of sample set B was tested at X m/s.
2. The glass block did or did not fracture.

Statement 1 of every data point is not a description of the specimen, it is a description of the test conditions the specimen was exposed to. Statement 2 is the outcome of the specimen when exposed to the test conditions in statement 1. Statistical tests such as the student's t-test and Z-test cannot be applied to the present data set, because those tests require that the same description of the **specimen** be compared across different sample sets, while statement 1 of our data set is a description of the **experiment** instead. In this case, the Fisher's Exact Test can be used to give the likelihood that the test conditions in statement 1 influence the outcomes in statement 2.

Fisher's Exact test calculates the probability of observing a particular or more extreme distribution in a 2x2 table of categorical data. In table A, an example of

the distribution of categorical data used in the examination of the impact test on the sample set of pure glass is shown. The velocity of 8.88m/s examined is the average of the lowest velocity at which fracture occurs and the highest velocity where no damage is observed. Please note that the velocity chosen is arbitrary, this statistical examination would give the same result as long as the velocity examined is between the lowest fracture velocity and highest intact velocity.

	Fractured	Intact	Row Totals
Impact Velocity $> 8.88ms^{-1}$	2	0	2
Impact Velocity $\leq 8.88ms^{-1}$	0	3	3
Column Totals	2	3	5

where the hypotheses are: The null hypothesis, H_0: An impact velocity above $8.88ms^{-1}$ is no more likely to cause fracture in a piece of transparent armor. H_1: An impact velocity above $8.88ms^{-1}$ is more likely to cause fracture in a piece of transparent armor.

The formula to exactly calculate the probability of the distribution in a particular table is

$$p = \frac{r_1!r_2!c_1!c_2!}{n!a!b!c!d!} \tag{A.1}$$

where the cells of the table are described in the positional table below:

	Fractured	Intact	Row Totals
Impact Velocity $> 25ms^{-1}$	a	b	r_1
Impact Velocity $\leq 25ms^{-1}$	c	d	r_2
Column Totals	c_1	c_2	n

In order to find the p-value of the Fisher's Exact Test, the probability of the distribution in question and more extreme tables would have to be calculated, these probabilities are then summed to obtain the p-value. Note that the table A is already the extreme distribution for a left-tailed or H_1 positive table, since the right diagonal

are populated by zeroes. In general, A computer algorithm for calculating Fisher's Exact Test is employed to give the probability of H_0 being true given the values in a particular table.

Simply, the probability of H_0 being true given the sample table A is

$$p\left(H_0\right) = \frac{2!3!2!3!}{5!2!0!0!3!} = 0.1 \tag{A.2}$$

Since there are no more extreme examples of H_1 occuring, the probability of rejecting the null hypothesis when H_0 is false is:

$$Power = 1.00 - p\left(H_0\right) = 0.9 \tag{A.3}$$

Power values range from 0.00 to 1.00. When the *Power* value is 1.00, it can be said with absolute certainty that the null hypothesis can be rejected, however, this value is mathematically impossible to attain. A large *Power* value is desirable.

APPENDIX B

Full derivation of the Analytic stresses for the Elastic Cylindrical Hertzian Contact Problem

The Elastic response of an elastic half-space indented by an elastic cylindrical indenter is a well studied problem. The following is a full derivation of the stress state of the plane strain stress state of the elastic half-space.

The full stress field for the 2D elastic half space under plane strain at any point with coordinates (y,z) can be obtained by the superposition of the stress state caused by vanishingly small segments of forces along the contact width between s=-a and s=b.

$$\sigma_y(0,y,z) = -\frac{2z}{\pi}\int_{-a}^{b}\frac{p(s)(y-s)^2}{\left((y-s)^2+z^2\right)^2}ds \tag{B.1}$$

$$\sigma_z(0,y,z) = -\frac{2z^3}{\pi}\int_{-a}^{b}\frac{p(s)}{\left((y-s)^2+z^2\right)^2}ds \tag{B.2}$$

$$\tau_{yz}(0,y,z) = -\frac{2z^2}{\pi}\int_{-a}^{b}\frac{p(s)(y-s)}{\left((y-s)^2+z^2\right)^2}ds \tag{B.3}$$

Since, only the line $y = 0$ is considered, we can simplify through substitution to obtain:

$$\sigma_y(0,0,z) = -\frac{2z}{\pi}\int_{-a}^{b}\frac{p(s)(s^2)}{(s^2+z^2)^2}ds \tag{B.4}$$

$$\sigma_z(0,0,z) = -\frac{2z^3}{\pi}\int_{-a}^{b}\frac{p(s)}{(s^2+z^2)^2}ds \tag{B.5}$$

$$\tau_{yz}(0,0,z) = -\frac{2z^2}{\pi}\int_{-a}^{b}\frac{p(s)(s)}{(s^2+z^2)^2}ds \tag{B.6}$$

Assuming the pressure distribution in the contact zone to be

$$p(s,0) = p_o\left(1-\frac{s^2}{a^2}\right)^{\frac{1}{2}} \tag{B.7}$$

The stress in the y and z directions are simplified as follows:

$$
\begin{aligned}
\sigma_y(0,0,z) &= -\frac{2z}{\pi}\int_{-a}^{a}\frac{p_o\left(1-\frac{s^2}{a^2}\right)^{\frac{1}{2}}(s^2)}{\left(s^2+z^2\right)^2}ds \\
&= -\frac{2zp_o}{\pi}\frac{\pi a^3}{2z^4}\left[\frac{-2+2\sqrt{1+\frac{a^2}{z^2}}-\frac{a^2}{z^2}}{\frac{a^4}{z^4}\sqrt{1+\frac{a^2}{z^2}}}\right] \\
&= -p_o\left(\frac{2}{\frac{a}{z}\sqrt{1+\frac{a^2}{z^2}}}-\frac{2}{\frac{a}{z}}+\frac{\frac{a}{z}}{\sqrt{1+\frac{a^2}{z^2}}}\right) \\
&= -p_o\left(\frac{2}{\frac{a^2}{z^2}\sqrt{\frac{z^2}{a^2}+1}}-\frac{2}{\frac{a}{z}}+\frac{1}{\sqrt{\frac{z^2}{a^2}+1}}\right) \\
&= -p_o\left(\frac{2\frac{z^2}{a^2}+2-1}{\sqrt{\frac{z^2}{a^2}+1}}-2\frac{z}{a}\right) \\
&= -p_o\left(\frac{2\left(\frac{z^2}{a^2}+1\right)}{\sqrt{\frac{z^2}{a^2}+1}}-\frac{1}{\sqrt{\frac{z^2}{a^2}+1}}-2\frac{z}{a}\right) \\
&= -p_o\left[\left(2-\left(\frac{z^2}{a^2}+1\right)^{-1}\right)\sqrt{\frac{z^2}{a^2}+1}-2|\frac{z}{a}|\right]
\end{aligned}
\tag{B.8}
$$

$$
\begin{aligned}
\sigma_z(0,0,z) &= -\frac{2z^3}{\pi}\int_{-a}^{b}\frac{p_o\left(1-\frac{s^2}{a^2}\right)^{\frac{1}{2}}}{\left(s^2+z^2\right)^2}ds \\
&= -\frac{2z^3p_o}{\pi}\frac{\pi}{2z^3\sqrt{-\frac{z^2}{a^2}-1}} \\
&= -p_o\left[\sqrt{\frac{z^2}{a^2}+1}\right]^{-1}
\end{aligned}
\tag{B.9}
$$

The shear stress along the line $y = 0$ integrates to 0.

Assuming the condition of plane strain, the stress in the out of plane direction is

$$
\begin{aligned}
\sigma_x(0,0,z) &= \nu\left(\sigma_y(0,0,z)+\sigma_z(0,0,z)\right) \\
&= \nu\left(-p_o\left[\left(2-\left(\frac{z^2}{a^2}+1\right)^{-1}\right)\sqrt{\frac{z^2}{a^2}+1}-2|\frac{z}{a}|\right]+-p_o\left[\sqrt{\frac{z^2}{a^2}+1}\right]^{-1}\right) \\
&= -2\nu p_o\left[\sqrt{\frac{z^2}{a^2}+1}+\sqrt{\frac{z^2}{a^2}+1}^{-1}-\sqrt{\frac{z^2}{a^2}+1}^{-1}-|\frac{z}{a}|\right] \\
&= -2\nu p_o\left[\sqrt{\frac{z^2}{a^2}+1}-|\frac{z}{a}|\right]
\end{aligned}
\tag{B.10}
$$

From our assumption that the $p(s)$ distribution takes the form in equation B.7, it is also assumed that the maximum pressure is p_o and occurs at $s=0$. The stresses are normalized with respect to p_{max} for comparison to the finite element stresses.

APPENDIX C

Numerical Simulation of End Notch Flexure (ENF) Test

The ENF test presented in Chapter VI is analyzed numerically to validate the modified smeared crack code presented in Section 7.4.

The model is analyzed with the Abaqus dynamic/explicit solver. The 3D model, shown in figure C.1 has 43482 C3D4 elements, and utilized fixed mass scaling to reduce the simulation run time. The elements representing the nanocomposite are designed to fail in shear. That is, the smeared crack model is modified so that the elements can only fail by shear parallel to the ENF arms.

The smeared crack model properties used are similar to those obtained experimentally in VI. A critical shear stress of 7.5MPa and a fracture toughness of 12.28N/mm give the best match for the force-displacement curve shown in figure C.2

The activation of the crack in the smeared crack user material representing the nanocomposite occurs at the time step where the force relaxation occurs.

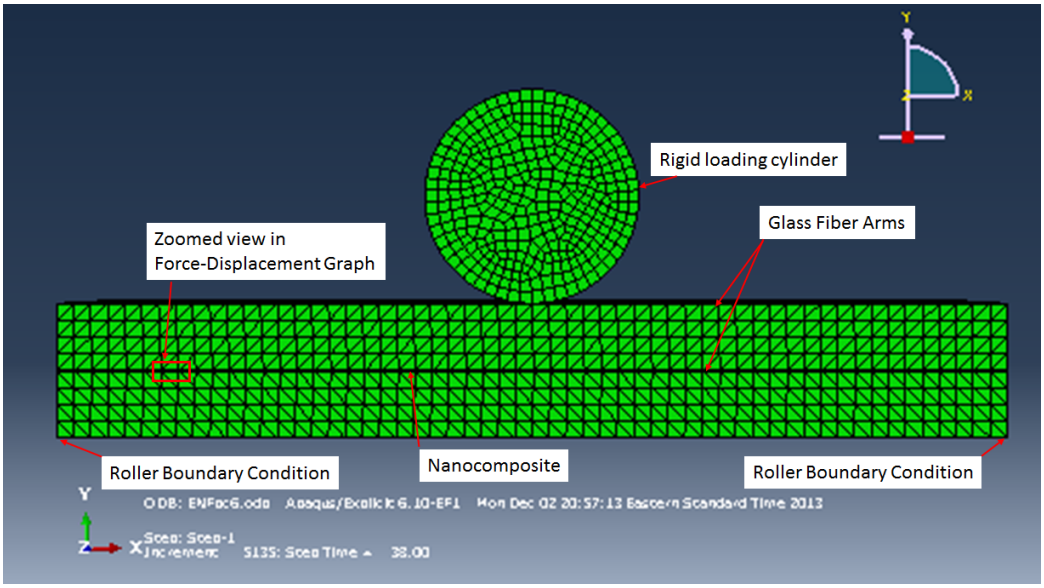

Figure C.1: Model for the ENF simulation

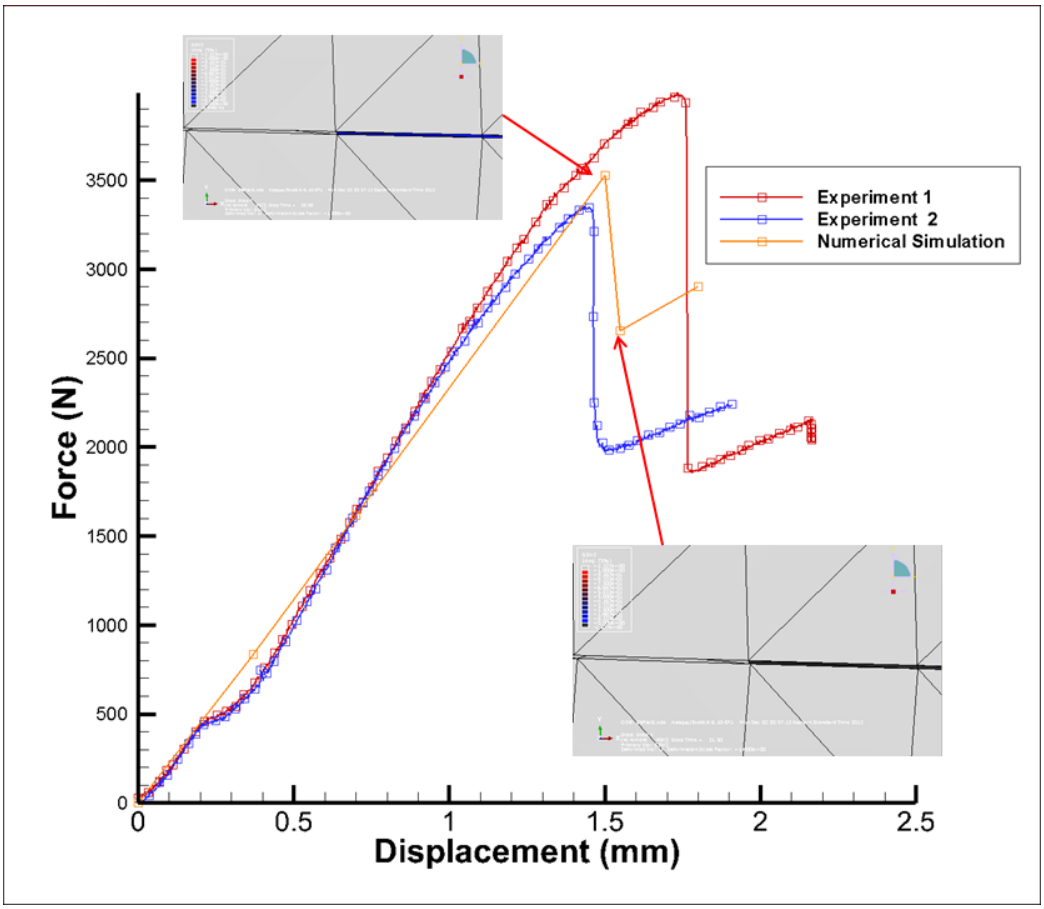

Figure C.2: Comparison of the Force-Displacement response of the End Notch Flexure Test

BIBLIOGRAPHY

BIBLIOGRAPHY

Anderson, T. L. (2005), Fracture mechanics: fundamentals and applications, *CRC Press*.

Arruda, E. M., and M. C. Boyce (1993), A three-dimensional constitutive model for the large stretch behavior of rubber elastic materials, *Journal of the Mechanics and Physics and Solids*, *41*, 389–412.

Bertoldi, M., and V. M. Sglavo (2004), Sode-borosilicate glass: normal or anomalous behavior under Vickers indentation, *Journal of Non-Crystalline Solids*, *344*, 51–59.

Boyce, M. C., D. M. Parks, and A. S. Argon (1988), Large Inelastic Deformation of Glassy Polymers, Part I: Rate-Dependent Constitutive Model, *Mechanics of Materials*, *7*, 15–33.

Chan, H. M. (1997), Layered Ceramics: Processing and Mechanical Behavior, *Annual Review of Material Science*, *27*, 249–282.

Chocron, S., C. E. Anderson Jr, K. A. Dannemann, and A. E. Nicholls (2009), Characterization of Borosilicate Glass Through Confined Compression Testing with Numerical Validation, *US Army RDECOM-TARDEC AMSRD-TAR-R*.

Fung, Y. C. (1969), A first course in continuum mechanics, *Englewood Cliffs, N.J.: Prentice-Hall*.

Gdoutos, E. E. (1990), Crack growth based on energy balance, *4*, 112–159.

Gunnarsson, C. A., B. Ziemski, T. Weerasooriya, and P. Moy (2009), Deformation and Failure of Polycarbonate during impact as a function of thickness, *Proceedings of the SEM Annual Conference*.

Heinrich, C., and A. Waas (2013), Investigation of Progressive Damage and Fracture in Laminated Composites Using the Smeared Crack Approach, *Computers, Materials and Continua*, *35*(2), 155–181.

Hoek, E. (1990), Estimating Mohr-Coulomb Friction and Cohesion values from the Hoek-Brown Failure Criterion, *International Journal of Rock Mechanics and Mining Sciences and Geomechanics*, *27*, 227–229.

Johnson, K. L. (1987), Contact Mechanics, *Cambridge University Press*, *978-0521347969*.

Lamdropoulos, J., and T. Fang (1996), Constitutive law for the densification of fused silica, with applications in polishing and microgrinding, *Journal of American Ceramic Society*, *79*, 1441–1452.

MacDonald, B. J. (2011), Practical Stress Analysis with finite elements, *Glasnevin Publishing*, *978-0955578168*.

Podsiadlo, P., A. K. Kaushik, and E. M. e. Arruda (2007), Ultrastrong and stiff layered polymer nanocomposites, *Science*, *318*(5847), 80–83.

Podsiadlo, P., M. Michel, J. Lee, and et al. (2008), Exponential growth of LBL films with incorporated inorganic sheets, *Nano Letters*, *8*(6), 1762–1770.

Podsiadlo, P., E. M. Arruda, E. Kheng, and et al. (2009), LBL Assembled Laminates With Hierarchical Organization from Nano- to Microscale: High-Toughness Nanomaterials and Deformation Imaging, *ACS Nano*, *3*(6), 1564–1572.

Popov, V. L. (2010), Contact Mechanics and Friction: Physical Principles and Applications, *Berlin, Heidelberg: Springer-Verlag Berlin Heidelberg*, *978-3-642-10802-0*.

Qi, H. J., and M. C. Boyce (2004), Constitutive Model for Stretch-Induced softening of the stress-stretch behavior of elastomeric materials, *Journal of the Mechanics and Physics of Solids*, *52*, 2187–2205.

Qi, H. J., and M. C. Boyce (2005), Stress-strain behavior of thermoplastic polyurethane, *Mechanics of Materials*, *31*, 817–839.

Rao, K. T. V., and R. O. Ritchie (1990), Mechanisms Influencing the Cryogenic Fracture-Toughness Behavior of Aluminum-Lithium Alloys, *ACTA Metallurgica et Materialia*, *38*(11), 2309–2325.

(Subcommittee-D30.06) (2007), ASTM D5528 - Standard Test Method for Mode I Interlaminar Fracture Toughness of Unidirectional Fiber-Reinforced Polymer Matrix Composites, *Book of Standards Volume 15.03*.

Sun, C., M. D. Thouless, A. M. Waas, and et al. (2008), Ductile-brittle transitions in the fracture of plastically deforming, adhesively bonded structures. Part II: Numerical Studies, *International Journal of Solids and Structures*, *45*, 4725–4738.

Suo, Z., and B. Fan (1992), Delamination R-curve phenomena due to damage, *Journal of the Mechanics and Physics of Solids*, *40*(1), 1–16.

Thouless, M. D. (2009), The effects of transverse shear on the delamination of edge-notch flexure and 3-point bend geometries, *Composites: Part B*, *40*, 305–312.

Xie, D., and A. M. Waas (2006), Discrete cohesive zone model for mixed-mode fracture using finite element analysis, *Engineering Fracture Mechanics*, *73*(13), 1783–1796.

Xie, D., A. G. Salvi, and C. SUN (2006), Discrete cohesive zone model to simulate static fracture in 2D triaxially braided carbon fiber composites, *Journal of Composite Materials*, *40*(22), 2025–2046.